PhD-FSTC-2012-14
The Faculty of Sciences, Technology and Communication

DISSERTATION

Presented on 04/05/2012 in Luxembourg

to obtain the degree of

DOCTEUR DE L'UNIVERSITÉ DU LUXEMBOURG

EN PHYSIQUE

by

Khanh-Quyen NGO
Born on 17 February 1984 in Ha-Noi (VietNam)

LOW-ENERGY SECONDARY ION MASS SPECTROMETRY: INVESTIGATION OF BURIED INTERFACES IN MULTI-LAYER ORGANIC THIN FILMS

The present project is supported by the National Research Fund, Luxembourg

LE-SIMS investigation of buried interfaces in multi-layer organic thin films

Acknowledgements

I would like to express my deep gratitude to many people who have supported me a lot during my PhD work.

First and foremost, I would like to thank Dr. Tom Wirtz for giving me this wonderful opportunity to be a part of the UIS group, CRP-Gabriel Lippmann and also for guiding me on this interesting research project. His helpful suggestions enriched my work and me, and made the thesis more clear and valued. I am very much grateful to him for all his support and his care of administration during my time in both the CRP-Gabriel Lippmann, Luxembourg and the University of Michigan, USA.

My sincere thanks to Dr. Patrick Phillipp for his supervision, availability, sharing his expertise in SIMS domain and especially for his patience to read and correct all my scientific manuscripts including this PhD thesis. I would like to thank him also for all his support and encouragements during my PhD work.

I would like to thank Prof. Susanne Siebentritt, my co-supervisor for her useful comments and suggestions during all the annual meetings and also for spending so much her valued time to read and to give valuable suggestions to my thesis.

I would like to thank Prof. Jan Kristian Krüger, Prof. Mark G. Dowsett and Prof. John Kieffer for being part of the thesis jury.

My hearty thanks to Dr. Jean-Nicolas Audinot, Patrick Grysan and Esther Lentzen for assisting me in the elemental imaging experiments in NanoSIMS50 instrument. A special thank goes to Patrick Grysan for helping me in the AFM imaging experiments. I want to thank Dr. Jérôme Guilllot, Sébastien Francois and Joffrey Didierjean for AES and XPS measurements and all the useful discussions.

Thanks to Dr. Nathalie Valle, Brahime Eladib, Rachid Barrahma, Mathieu Gérard, Arnaud Moschetta, Samir Menaouli and Alain Robert for their support and assistance to use of the Sc-Ultra instrument.

I thank Peter, Sudharsan, Beatrix, Catalina, Nora, Ludovic and Hung for all the meaningful discussions, interesting exchanges, shared moments, funny stories and ever-growing friendship. I also thank the others members of the group: Canan, Antoine, Arindam, Lex, Ben, Nico, David, Yves and Oleksiy for their kind support and sharing. I will surely miss our time together in the group meetings and in the lunch hall.

I would like to address my gratitude to the Human Resources services, the support services, the secretary and the library staff for all their assistance, and all those in the CRP Gabriel Lippmann whose names are not mentioned here for their kind supports during the last three years.

I thank also Prof. John Kieffer and Prof. Max Shtein and their groups for their warm welcome during the time I spent in Michigan and for all helpful supports, assistances to the preparation of samples for my studies.

The project was supported by the National Research Fund, Luxembourg (NSF-FNR-MAT-07-01) and the US National Science Foundation (NSF-DMR 0806867).

Finally, I thank my family and friends in Luxembourg, in France and in Viet Nam for supporting me throughout all the three years.

Table of content

Introduction

Recently, conjugated organic compounds appear as potential electronic materials due to their tuneable property via chemical synthesis and to the low-cost processing. Consequently, the application of these materials increases significantly in optoelectronic devices e.g. organic light-emitting diodes (OLED), photovoltaic (PV) cells, and field effect transistors (FET) etc. These devices are generally composed of several layers situated between two electrodes, all deposited on a substrate. The main performances of these devices such as charge and energy transport, operational lifetime and energy conversion efficiency depend strongly on the doping and the interface structure. Therefore, understanding the impact of deposition conditions on layer structure as well as interface structure is very important for the development of the deposition techniques. It requires a characterization technique with molecular-level dimensional control. Among various analytical techniques like scanning electron microscopy (SEM), atomic force microscopy (AFM), cross-sectional transmission electron microscopy (XTEM), and small-angle x-ray diffraction (SAXD), secondary ion mass spectrometry (SIMS) is a powerful technique that allows not only for obtaining information about molecular, elemental and isotopic composition of surfaces but also for depth profiling. SIMS is based on material sputtering by an ion beam and secondary ion determination in mass-to-charge ratio and has an excellent sensitivity (ppm to ppb detection range), a high dynamic range as well as a nanometre range depth resolution. Thus, for elemental depth profiling of thin films, dynamic SIMS is a perfect characterization technique.

However, up to now, dynamic SIMS, which achieves the depth profile by eroding the sample surface, is applied traditionally to the analysis of surfaces and thin films of inorganic compounds and alloys. Due to high impact energies and continuous bombardment, conventional dynamic SIMS causes a lot of fragmentation which hampers its application to organic materials, i.e. the organic information gets lost during the sputtering or interface broadens due to atomic mixing. Therefore, in this project we develop dynamic SIMS analysis

conditions using low energy primary ion beam to analyse multi-layered samples used in organic optoelectronic devices. For the characterization of organic samples, the low energy atomic bombardment causes less fragmentation than sputtering by high-energy atoms and therefore some organic fragments may be observed throughout the whole depth profiles. Furthermore, low impact energies reduce also the atomic mixing during the sputtering, and allow thus to enhance the depth resolution.

The objective of this thesis is to study the different artefacts and mechanisms, which may arise in the low-energy depth profiling of organic materials and to optimize the SIMS conditions for interface resolution. For the objectives, in chapter I, a general introduction about the organic molecules used in this work as well as the fabrication techniques is presented. In addition, the deposition conditions and the properties of the samples are also listed. In chapter II, the fundamental aspects of the SIMS technique, description of the instruments used (the Cameca SC-Ultra and the Cameca NanoSIMS 50) as well as the analysis conditions are provided. Moreover, other analysis techniques used in this work and the corresponding analysis conditions are also described.

In chapter III, a study of the fragmentation of different organic films during sub-keV bombardment is performed. In this study, the impact of low energy primary ion beam on organic fragmentation is characterized. Moreover, the typical secondary ions of different organic molecule are identified. The ions with high and stable intensity are chosen for depth profiling the organic sample in chapter V and VI.

Chapter IV is a study about air-contact induced topography change on Cs^+ sputtered surface. In this work, the formation of Cs-O hillocks after air exposure the Cs^+ sputtered organic surface is proven by different characterization techniques i.e. SIMS imaging, Auger electron spectroscopy (AES), Atomic force microscopy (AFM). By combining the analysis results from AFM and X-ray photoelectron spectroscopy (XPS), the mechanism of Cs-O hillocks formation is explored. This is useful to avoid artefacts when characterizing the Cs^+ sputtered surfaces by AFM to study the contribution of irradiation-induced roughness to SIMS interface widths (chapter V).

The ability of low-energy SIMS to characterize the metal/organics interfaces is investigated in chapter V and VI. Chapter V is about the SIMS depth resolution and sputter-induced surface roughness studied on a series of metal – organic layered samples. As results, different interface structures are qualified and the impact of sputter-induced roughening is also taken into account. In chapter V, The diffusion of metal into organic layer seen in SIMS depth profiles is characterized on different samples for different analysis conditions. Results from using the peeling-off method combined with backside depth profiling shows that the diffusion is due to two mechanisms: diffusion during sample preparation and sputter – induced diffusion.

Chapter I
Organic materials in optoelectronic devices

I.1. Organic optoelectronic devices

The application of conjugated molecular and polymeric organic compounds in the area of energy conversion is increasing[1,2]. Two devices that have shown an impressive development recently are organic light-emitting diodes (OLED)[3] and organic photovoltaic cells (OPVC)[4]. Both systems consist of thin organic films sandwiched between two electrodes, the anode and the cathode.

Compared to inorganic devices, OLEDs have shown several advantages i.e. a large illuminating area, a light weight, low costs and flexibility. Figure I.1 shows the schematic of recombination processes in a basic two-layer OLED, which is composed of a hole and an electron transport layers (HTL, ETL), sandwiched by an anode and a cathode electrode. When an electrical potential difference is applied between the two electrodes, holes are injected from the anode into the HTL and electrons are injected from the cathode into the ETL. These injected holes and electrons migrate towards the interfaces between HTL and ETL layers and recombine near the junction in the luminescent ETL. Upon recombination, photons are released and emitted from the light-transmissive anode and substrate. This structure can be modified to improve the light-emitting efficiencies by adding further layers[5-8] i.e. an additional luminescent layer between HTL and ETL layers as the site for hole-electron recombination and electroluminescence. This separation allows to optimize independently the function of individual organic layers e.g. luminescent layer can be chosen for a desirable emitting-light colour as well as a high luminance efficiency[5,7,9-11]. Furthermore, to promote the injection of charges (holes and electrons) from the

electrodes (anode and cathode) into the charge transport layers (HTL and ETL), further injection layers can be added between electrodes and transport layers, called charge injection layers[6]. While the internal quantum efficiency of some OLEDs approach theoretical limits (i.e. 100% through electrophosphorescence emitting layer[9,12,13]), the light extraction is typically limited to 20% due to light trapping and waveguiding in the organic layers and electrodes[14,15]. Besides low device efficiencies, the degradation pathways, which control device operational stability and operational lifetime, are not well understood.

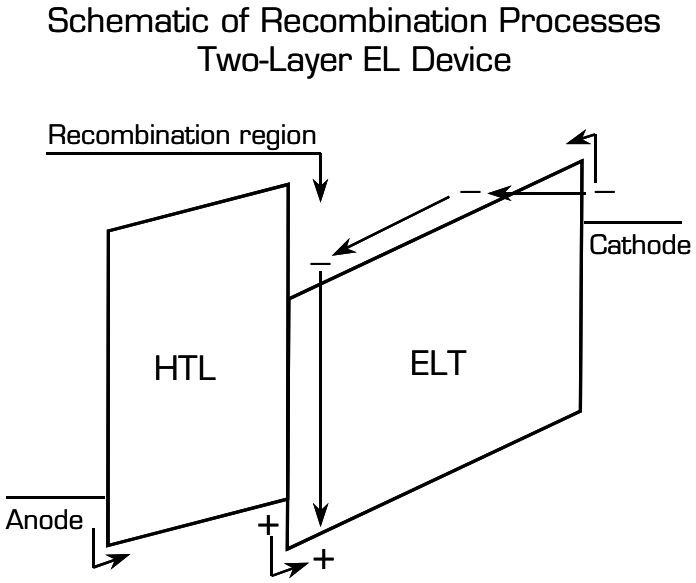

Figure I.1: *Energy level diagram of a two-layer OLED[16].*

The growing global energy needs, the finite supply of fossil fuel sources, the detrimental long-term effects of CO_2 and other emissions into our atmosphere as well as the doubtful question about safety of nuclear power, raise the urgency of developing renewable energy resources. Therefore, harvesting energy directly from sunlight, photovoltaic technology causes a lot of attention[17]. Compared to tradition photovoltaic cell technology using inorganic materials, OPVC has some potential advantages i.e. light-weight, economical in material used, and great flexibility of substrates (low-cost substrates such as plastic foils, which are compatible with continuous roll-to-roll processing)[18]. Figure I.2 shows a schematic of energy conversion operation of an OPVC. The

energy conversion mechanism has been well described by Peumans[19]: absorption of a photon, *hv*, in the active layer leads to the generation of a bound excited state (exciton), which diffuses to the donor-acceptor interface then dissociates into electron and hole. The charges then immigrate to the electrodes, creating a voltage between two electrodes, and an electric current if the two electrodes are connected. A device with a stack of bi-layer cells can increase output voltage. The change of the interface between layers of the stack is listed as one of the main factors that lead to device degradation[20]. Moreover, doping and interfaces are critical in OPVCs to increase the energy conversion efficiency i.e., the dispersion of metallic nanoparticles in the organic layers on purpose or even damage at the interface between the metal/organic interface lead to the enhancement in power conversion efficiency[19,21].

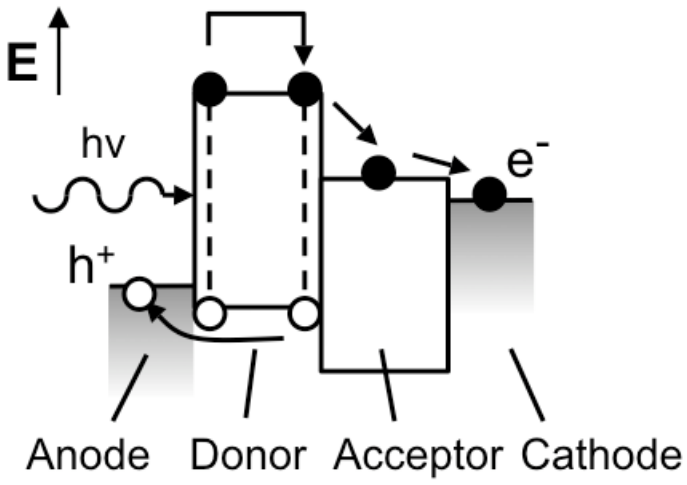

Figure I.2: *Schematic of energy conversion diagram for a two layer OPVC.*

As presented above, in order to improve the device efficiency, stability and lifetime, the structure of OLED and OPVC becomes a complicated multilayered system. Therefore, the nature of layers and of interfaces and doping play an important role in efficiency of charge and energy transport, energy conversion efficiency as well as degradation which decreases operational lifetime and stability of devices[22,23]. Exact characterization of doping, layers and interfaces becomes therefore essential.

Analysis techniques that are commonly used are atomic force microscopy (AFM), scanning electron microscopy (SEM), scanning tunnelling microscopy (STM), transmission electron microscopy (TEM), Auger electron spectroscopy (AES)… SEM, AFM and STM techniques can provide 2D or 3D surface profiles with a resolution down to atomic scale. TEM allows imaging with a resolution down to 0.5 Å and it can give information about the material structure. Therefore, TEM can give structural information of a cross-section of a multilayer sample. However, the image contrast is not always good enough to identify different materials. Sample preparation (sectioning, etching, milling…) is however often difficult, time consuming and it may also change the structure of the sample. AES can provide chemical images and also elemental depth profiling. In addition, it allows quantitative analysis. However, the detection limit of AES is only in the 0.1-1 at% range. Compared to these techniques, secondary ion mass spectrometry is a powerful technique, which can give either a chemical surface image or an elemental depth profile. It combines excellent sensitivity (parts-per-billion) with high dynamic range and superb depth resolution (~nm). In addition, no treatment of the sample prior to the analysis is required.

I.2. Organic molecules and organic thin films

Among the organics used in optoelectronic device, we focus on some common organic molecules in this study: aluminium tris(8-hydroxyquinolinato) (Alq_3), phthalocyanine derivatives (MPc) and fullerenes (C_{60}) (Figure I.3). While Alq_3 is the most important electron-transport material, and also an emissive material for green light OLED, MPc is used as hole transport material for improving the OLED device efficiency, stability and the operation lifetime[24]. C_{60} is usually used as electron acceptor in OPVC. As for the molecular structure, C_{60} contains only carbon atoms, while phthalocyanine derivatives ($C_{32}H_{16}N_8M$, M is a metal) is a complex with a metal atom M in the centre of the phthalocyanine. The atomic % of nitrogen in MPc molecules is 14 % for CuPc. Alq_3 ($Al(C_9H_6NO)_3$) has aluminium bonded to three 8-hydroxyquinoline groups (C_9H_7NO) and thus

includes 5.8 atomic % of nitrogen. The densities of the organic films are presented in table I.1.

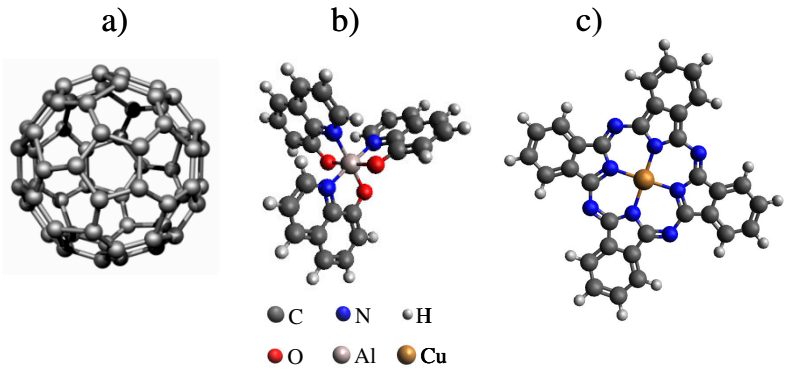

***Figure I.3**: Organic molecules used in this study: a) Fullerene b) Aluminium tris(8-hydroxyquinoline) and c) Copper Phthalocyanine.*

Organic molecule	Film density (g/cm^3)
Alq_3	1.3[25,26] - 1.5[27]
CuPc	1.5[26] – 1.6[28] – 1.8[29]
C_{60}	1.5[26]
Pc	1.5[30]
FePc	1.6 (calculated by TRIM)
ZnPc	1.4[31] - 1.5[32]

***Table I.1:** Film density of different organic materials.*

The surface topography of an organic material develops depending on many factors: nature of organic molecule[33,34], nature of substrate[34,35], substrate temperature[28,34,36], thickness of the film[34]… The CuPc molecule has a planar square configuration with a side length of about 1.3 nm and a diagonal of 1.5 nm[37,38]. However, X-ray diffraction studies on CuPc thin films show that the CuPc molecules do not lie parallel to the substrate plane and that the CuPc films have a low degree of crystallization with an interplanar spacing of about

1.3 nm[34,36]. This means that the CuPc surface roughness after deposition must be worse than 1.3 nm, as also indicated in other studies[28,39]. The surface roughness of Alq_3 thin films amounts to 2.7 nm[40].

Moreover, varying the film thickness also develops surface roughness: thin films have a smoother surface than thicker ones[39,41,42]. Yang et al. showed an increase of surface roughness from 1 nm to 10 nm when the CuPc thickness grew on an ITO-coated glass from 6 nm to 9 nm[34]. The substrate temperature during organic deposition has also an influence on the development of surface topography. In general, the surface is smoother at low substrate temperature[36,39].

The properties of deposited layers change when another layer is deposited on top. Therefore, the preparation conditions need to be optimized for each layer. As an example, Jin et al.[39] show results from a series of three stacks of CuPc/Ag multilayers prepared in a vacuum thermal evaporation method. For a layer thickness of less than 8 nm prepared at room temperature, the authors show an evidence of the material mixing completely by cross sectional TEM. In addition, the reaction between metal and organic layers influences also the interface structure and properties. No chemical reaction is found for Ag or Au[43] but a significant reaction/diffusion is verified for Mg or Al[43-45].

I.3. Deposition techniques

Vacuum thermal evaporation technique (VTE) is a common method used in thin film growth for organic optoelectronic devices. In this section, we present the principles of this technique and describe two VTE systems at University of Michigan, which are used for the preparation of samples: a conventional Angstrom system and a lab-built supper-lattice system.

I.3.1. General description

Figure I.4 presents a schematic of the VTE technique. The deposition takes place in a vacuum chamber in which material sources are at the bottom and

substrate targets are placed on top of them. The use of vacuum is necessary for a high degree of purity, homogeneous films and a structural control. The sources contain the conjugated organic molecules in form of crystalline powders. The source is heated to evaporation temperature by applying an electrical current. The material evaporates and deposits on the substrates placed several centimetres above the sources. A shutter plane between material sources and substrate targets can be opened and closed to control the deposition process. During the deposition process, the film thickness is controlled using a pre-calibrated quartz crystal monitor placed near the substrate. The substrate can rotate to create smoother films.

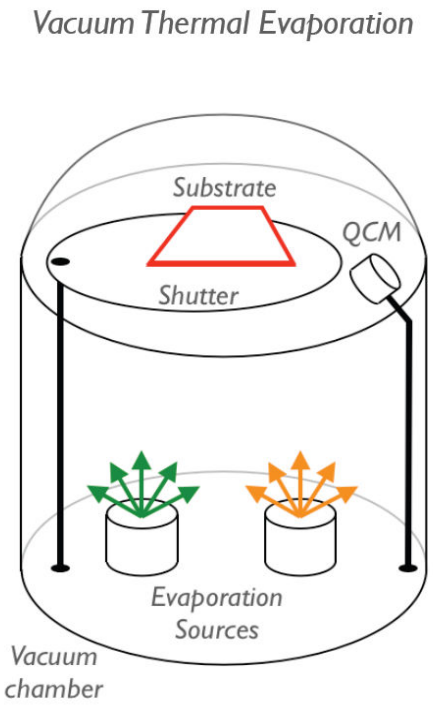

***Figure I.4**: Principles of vacuum thermal evaporation technique.*

I.3.2. Standard Angstrom VTE system

The used Angstrom VTE system is of the Åmod design created by Angstrom Engineering INC[46]. The system has 6 material sources which allow depositing multilayered samples without venting the system. Stainless steel shields isolate

the sources to protect from cross contamination. An extra shutter above each source prevents leaks from the preheated source in multilayer deposition. A top QCM sensor near the target substrate and three QCM sensors above the sources ensure a good calibration. The conventional substrate holder can rotate during the deposition. Substrate temperature is not monitored. For some applications, the substrate holder can be replaced by a special system that allows controlling the substrate temperature down to low temperature by using liquid N_2.

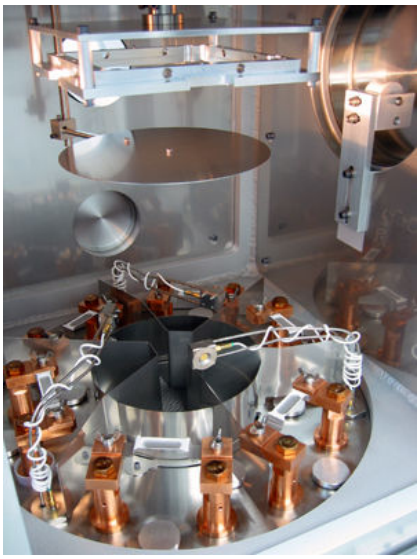

***Figure I.5**: Deposition chamber of Angstrom VTE system*

I.3.3. Lab-built supper-lattice VTE system

The superlattice system is a compact VTE instrument, which can be used to prepare superlattice structures of two materials at the same time. The system was designed and built in the group of Professor Max Shtein at The University of Michigan. It requires 30 minutes to reach a pressure of 1.3×10^{-6} mbar while the Angstrom system needs at least 2 hours. The two material sources sit inside two tubes that lead the evaporated material from the source to the substrate and avoid cross-contamination. A QCM is mounted on each tube to calibrate the deposition rate and layer thickness. As the two sources A and B are heated, the substrate rotates from the non-depositing position to the

depositing position above material A and then to the depositing position above material B. Thus, by programming the time above each source, the desired thickness of each layer is obtained.

a) b)

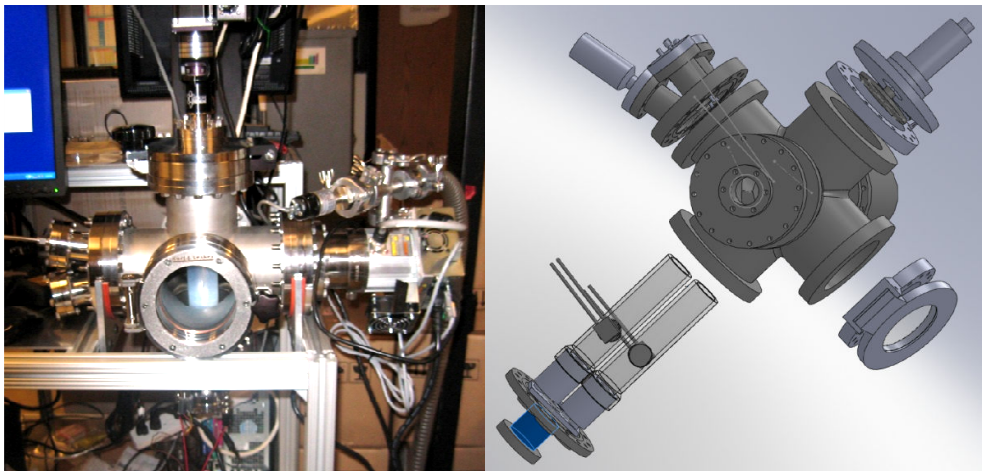

***Figure I.6**: Lab-built superlattice VTE system a) photo of the system, b) set-up of the deposition chamber*[47].

I.4. Sample preparation

I.4.1. Substrate cleaning

In this study, Si wafers were used as substrate. The substrates were cleaned by sonicating in solvents. The order of the cleaning solvents as well as the washing times and temperatures are listed in table I.2. After cleaning, the substrates were dried with nitrogen gas and were treated with UV/ozone for 10 minutes. The UV/ozone allows eliminating the residual hydrocarbons and water on the Si wafers. Then, the substrates were mounted in the deposition position in the VTE chamber.

Order	Solvent	Time	Temperature
1	Deionized (DI) water	5 minutes	Room temperature (RT)
2	DI water + soap	5 minutes	RT
3	Acetone (ACE)	5 minutes	RT
4	Trichloroethylene (TCE)	5 minutes	RT
5	TCE	5 minutes	RT
6	ACE	5 minutes	RT
7	ACE	5 minutes	RT
8	Isopropyl alcohol (ISO)	5 minutes	RT
9	ISO	5 minutes	RT
10	ISO	10 minutes	80 °C

Table I.2: *Cleaning procedure for the Si wafers.*

I.4.2. Organic single layers

The samples were deposited at room temperature at a pressure of about $1.3x10^{-6}$ mbar in the Angstrom system. Substrates were silicon wafers cleaned according to the procedure described in I.4.1. Before layer deposition, the QCM sensors were calibrated as follows: a calibrating film in the nanometre range was deposited onto a silicon wafer, the thickness of this film was measured by ellipsometry and the measured thickness was compared to the value from the QCM sensor. Next, the tooling factor of the QCM sensor was corrected. During deposition, the deposition rates were controlled in the range of 0.5-1.5 Å/s.

The organic single layer samples were used to study the fragmentation of organic molecules used in organic optoelectronic devices during Cs^+ low-energy bombardment (Chapter III) and the aggregation of Cs to Cs-O in Cs-implanted craters after air contact (Chapter IV). The samples are described in table I.3.

Sample	Organic molecule	Film thickness (nm)	Characterization techniques	Results in
S1	C_{60}	43	SIMS	Chapter III
S2	Alq_3	100	SIMS	Chapter III
S3	CuPc	150	SIMS	Chapter III
S4	Alq_3	80	SIMS+XPS	Chapter IV
S5	CuPc	80	SIMS+XPS	Chapter IV

Table I.3: *Description of organic single layer samples.*

I.4.3. Metal-organic bi-layered samples

The metal-organic bi-layered samples are composed of a metal film, which is either silver or aluminium, and an organic film on a silicon substrate. The metal and the organic film have the same layer thickness. After cleaning the silicon substrate, the organic layer was deposited first and the metal layer next. The deposition was performed in the Angstrom system or in the superlattice system. The pressure in the deposition chamber was about $1.3x10^{-6}$ mbar. The substrate was kept at room temperature (RT samples) or at –60°C (cryo samples) for studying the influence of deposition temperature on the interface structure and on the property of deposited film. The QCM sensors were calibrated in the same way than in I.4.2. The procedure was applied to both metal and organic layers. The deposition rate was set to about 0.5-2.0 Å/s for the Al layers, between 0.1-2.0 Å/s for the Ag layers and between 0.5 -1.5 Å/s for the organic layers. The samples are described in table I.4.

Sample Ag/organic	Organic molecule	Layer thickness (nm)	Substrate temperature	Deposition system	Characterization techniques	Results in
A1	Alq_3	30	RT	Angstrom	SIMS+AFM+AES	Chapter IV, V, IV
A2a	CuPc	30	RT	Angstrom	SIMS	Chapter V, VI
A2b	CuPc	30	RT	Angstrom	SIMS+AFM+AES	Chapter IV, V
A3	Pc	30	RT	Angstrom	SIMS	Chapter V, VI
A4	FePc	30	RT	Angstrom	SIMS	Chapter V, VI
A5	ZnPc	30	RT	Angstrom	SIMS	Chapter V, VI
B1	CuPc	12	RT	Superlattice	SIMS+AFM	Chapter V, VI
B2	CuPc	48	RT	Superlattice	SIMS+AFM	Chapter V
C1	CuPc	13	-60°C	Angstrom	SIMS+AFM+AES	Chapter IV, V, VI
C2	CuPc	30	-60°C	Angstrom	SIMS	Chapter V, VI
Sample Al/organic	**Organic molecule**	**Layer thickness (nm)**	**Substrate temperature**	**Deposition system**	**Characterization technique**	**Results in**
D	CuPc	30	RT	Angstrom	SIMS	Chapter VI

Table I.4: Description of metal-organic bi-layered samples.

I.4.4. Al/Ag/CuPc sample

For peeling-off tests, a sample of three layers containing an Ag and an Al film on top of the CuPc film was prepared in the Angstrom system at room temperature. The three layers had the same thicknesses of 30 nm. The sample is described in table I.5.

Sample	Organic molecule	Al Layer thickness (nm)	Characterization technique	Results in
P	CuPc	30	SIMS	Chapter VI

Table I.5: *Description of peeled-off sample.*

Chapter II
Characterization of organic materials

This chapter presents the analysis techniques that have been used in this study, including Secondary Ion Mass Spectrometry (SIMS), Atomic Force Microscopy (AFM), X-Ray Photoelectron Spectroscopy (XPS) and Auger Electron Spectroscopy (AES). Among these techniques, SIMS was used as the main technique for the characterization of the organic multilayered samples. The other techniques are used to study artefacts produced by low-energy SIMS (LE-SIMS) in organic materials.

II.1. Secondary Ion Mass Spectrometry

II.1.1. Introduction to SIMS

The emission of neutrals and ions emitted from a solid surface during ion bombardment was first observed by Joseph J. Thomson in 1910[48]. Information on surface composition is obtained by analyzing the ejected ions.

In 1949, the first SIMS prototype using an electron impact primary ion source was developed by Herzog and Viehboeck[49]. Later, complete SIMS instruments were constructed by Honig[50], Bradley[51], Beske[52], Werner[53] as well as Castaing and Slodzian[54].

Depending on the application, one distinguishes between static SIMS and dynamic SIMS. In the 1970s, static SIMS was introduced by Benninghoven and it soon became a powerful technique to characterize the extreme surface of samples and organic materials[55,56]. In static SIMS, the sample is exposed to a low primary ion fluence such that the generated collision cascades do not

overlap and the organic materials are less fragmented. Thus, it allows to obtain molecular information from the uppermost surface layer[57-62]. This technique is mainly used for the acquisition of mass spectra and for imaging. In dynamic SIMS, much higher primary ion fluences are used to sputter the sample, which allows for depth profiling into a bulk material[63,64] and obtaining elemental compositions down to the ppb level.

The primary ion beam can be formed of atomic ions (e.g. Ar^+, Cs^+, Ga^+), molecules or small cluster ions (e.g. O_2^+, SF_5^+, C_{60}^{n+}, $Au_{n\ (n=1-3)}^+$, $Bi_{n\ (n=1-7)}^+$) or massive cluster ions (e.g. Ar_{500}^+, Ar_{1000}^+, Au_{400}^{4+}…). The primary ions are created in an ion source, and accelerated and focused towards the sample to be analyzed. These ions implant into the sample, change the bombarded surface and sputter material from the sample surface. Depending on the sample potential, only negative or positive secondary ions (secondary ions representing typically less than 1% of sputtered matter) can be extracted by the extraction lens and accelerated towards the mass spectrometer. There, the ions are separated according to their mass/charge ratio and collected by detection systems.

Since its introduction, SIMS has developed strongly for various analytical applications, including the acquisition of mass spectra, depth profiling and 2D and 3D imaging (Figure II.1). The mass spectrum is a plot of secondary ion intensities as a function of mass-to-charge ratio (m/z). It presents the chemical composition of a material. Mass spectra are useful for identification of surface contaminations and bulk composition[57,65-68]. For depth profiles, secondary ion intensities of some elements are recorded while sputtering into the material (Figure II.1). It is applied successfully to thin films in the semiconductor domain[69-71] as well as to metals, glasses, organics, …. Finally, elemental mapping supplies information on chemical composition with lateral resolution down to 50 nm[72]. Elemental mapping in SIMS has been used successfully in biology and medecine[61,73-76] as well as in studies for surface contaminations[66].

To summarize, SIMS is a powerful technique for surface and thin film analysis. Its main advantages are listed below:

- Large range of detectable masses: from 1 (H) up to molecular masses of 10.000 amu.

- Can detect all elements (from H to U) as well as distinguish between different isotopes.
- High sensitivity: some elements can be detected with a concentration down to the ppb level (parts-per-billion).
- High mass resolution allows SIMS to avoid mass interferences.
- In SIMS depth profiling, the depth resolution can reach the sub-nm range by reducing the impact energy.
- In SIMS imaging, the lateral resolution can be as good as 50 nm on dedicated instruments.

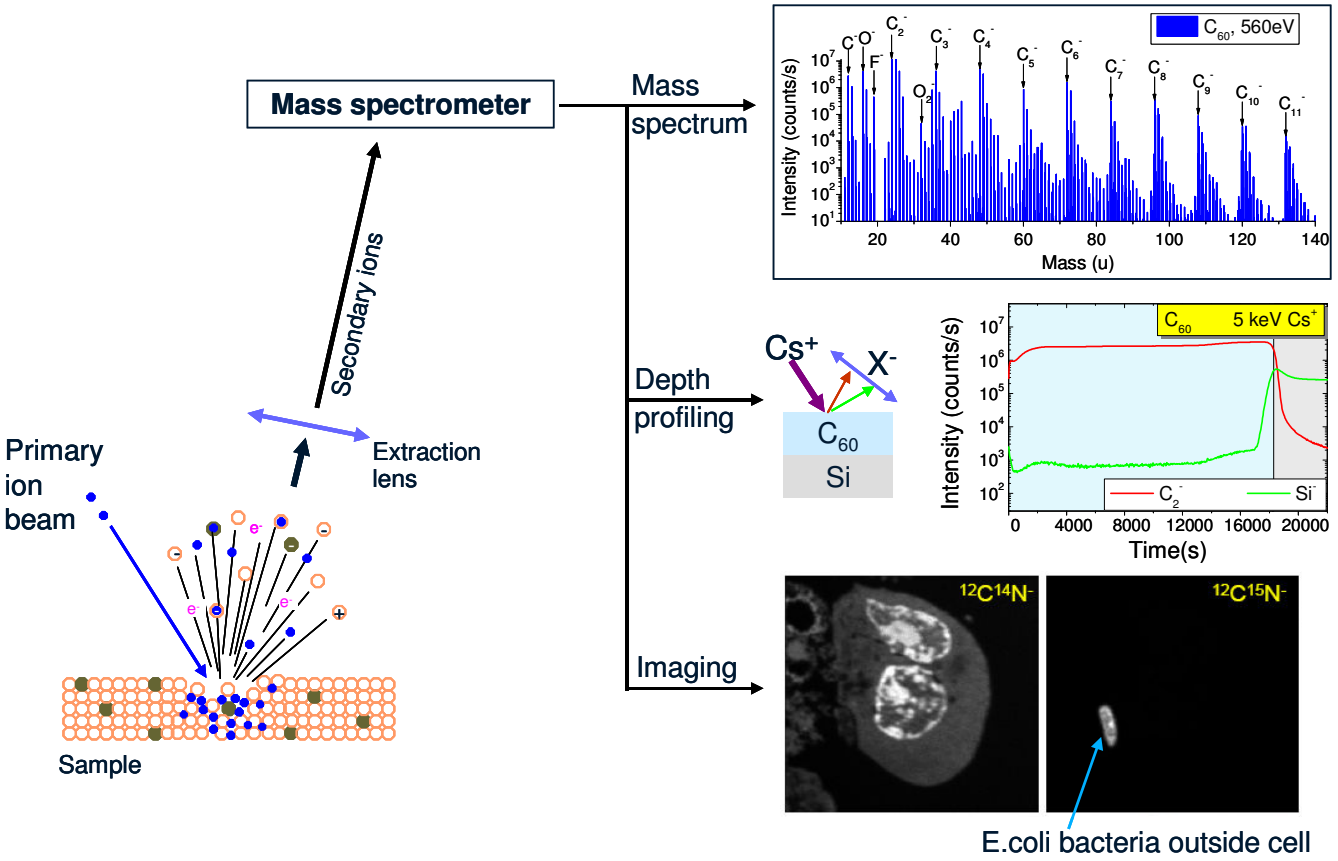

***Figure II.1**: Particle-surface interactions in SIMS and its applications. Examples shown here: mass spectrum from C_{60} analyzed at 560eV Cs^+, depth profiling of C_{60} thin layer on Si substrate and $^{12}C^{14}N$ and $^{12}C^{15}N$ images of biological sample to track E.coli by SIMS (E.coli is labelled with ^{15}N)[77].*

II.1.2. Ion-solid interactions

II.1.2.i. Interaction mechanisms

When an energetic ion beam bombards a surface, it undergoes a series of collisions with substrate atoms. Then a fraction of ions implant into the material. At each collision, they transfer a part of their energy and momentum to the target atoms and electrons. Thus, the primary ions lose progressively their energy, slow down, and finally stop in the solid. A small fraction of the primary ions is also backscattered.

Inside the target, the atoms receive energy during the collisions with the primary ions. They may be set in motion; they can be displaced by several interatomic distances. This recoil atom may hit other atoms resulting in a collision cascade. If surface or near – surface atoms receive a momentum in the direction towards the vacuum with an energy high enough to overcome the surface binding energy, they are sputtered. The majority of the ejected atoms (i.e. 60%) are from the first atomic layer[78,79].

Therefore, the implantation depth of primary ions and the dimensions of the perturbed zone in the target depend not only on the primary ion beam parameters (impact energy, incidence angle and ion species) but also on the target nature (material density, mass of target atoms, surface topography and crystallinity). In SIMS analysis, a collision cascade has typically an impact on an area of about 100 $Å^2$ with a lifetime in the range of 10^{-11}-10^{-12} s. With a current density of less than some mA/cm^2, the collision cascades can be considered independent one from the other[80]. Therefore, based on the energy and mass of the incident ion, three different collision cascade regimes can be identified[81,82]:

- The *single-knock on regime* for light ions and low energy heavier ions. In this regime, the recoil atoms, which are hit by the incident ion, receive a sufficient energy to leave the surface but not enough energy to generate a cascade.
- The *linear-cascade regime* is for ions of medium or high mass at energies up to a few keV. Here, the recoil atoms receive enough energy

to generate collision cascades. However, the density of the recoil atoms is low such that the collision cascades induced by different impact particles do not superpose.

- The *collision-spike regime* is for incidence of heavy atoms or molecules or atom clusters with sufficient high energy. Here, the recoil atoms are so dense, that the collision cascades overlap and the majority of atoms in a certain volume are in motion.

Therefore, the low-energy bombardment in this work can be considered to be in the single-knockon and linear-cascade regime.

II.1.2.ii. Sputtering

The target particles that are ejected when irradiating a surface with an energetic beam can be neutral or charged, and they can be atoms, clusters, molecules or molecular fragments[56]. The sputter yield, which is defined to quantify the amount of sputtered matter, is given by:

$$Y(M^q) = \frac{number\ of\ sputted\ atoms\ M^q}{number\ of\ primary\ ions} \qquad (II.1)$$

For a given material, the sputtering yield may vary with the primary ion beam parameters i.e. the energy, the mass and the impact angle of the incident ions. The dependence of the sputtering yield on the impact energy and the primary ion species is shown in an example in Figure II.2. At first, the sputtering occurs only when the bombarding energy is larger than the threshold energy (typically 20-50 eV). Then it increases with the impact energy to a maximum situated at a few keV for light incident particles and at about 100 keV for heavy particles. At higher impact energies, the sputtering yield gradually decreases. This phenomenon is due to the deep penetration of the primary ions into the solid, thus less energy is deposited near the surface. The influence of the primary ion mass on the sputtering yield is negligible at impact energy lower than 500 eV but becomes important at higher impact energy[81,83]. Similar trends to the ones described in Figure II.2 for a Si sample are observed for organic materials[84].

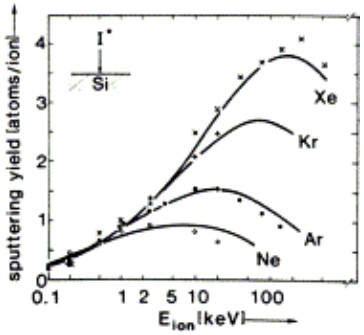

Figure II.2: *Sputtering yield of Si for various noble gas ions at normal incidence measured as a function of the primary ion energy*[85].

Moreover, the sputtering yield Y depends on the angle of incidence θ_{in} defined with respect to the surface normal [86,87]:

$$Y \sim \cos^{-s}\theta_{in} \ , \ 1<s<2 \text{ for } \theta_{in} < 80° \qquad \text{(II.2)}$$

Y increases with θ_{in} up to a maximum obtained between 55°-85°, then decreases (Figure II.3). The reduction at near – glancing incidence is related to the particle and energy reflection[81,83]. This effect is observed both for inorganic and organic materials [88-91].

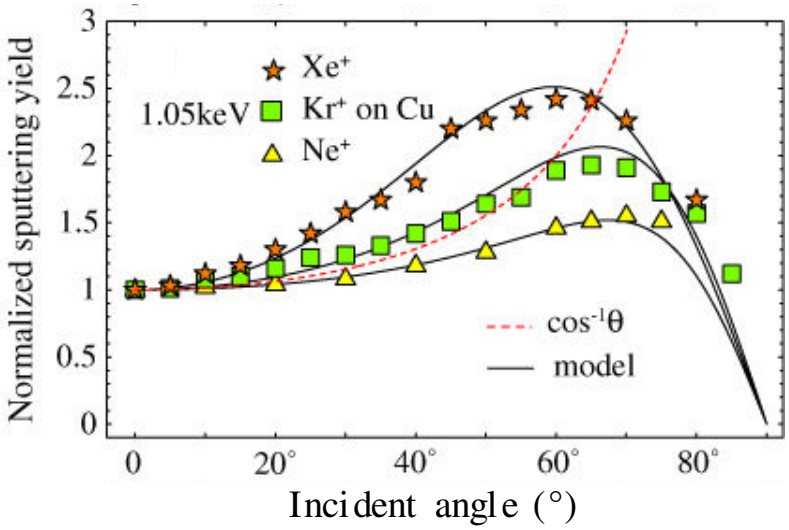

Figure II.3: *Sputtering yield as a function of incident angle at 1.05 keV Xe^+, Kr^+, Ne^+ ions on Cu in model (solid line) and experimental results (symbol)*[92].

II.1.2.iii. Ionization

II.1.2.iii.a. Ionization mechanisms

Over the last decades, many ionization models were proposed to describe the experimental results that were obtained under various conditions from various samples. Well-known models are for instance the electron-tunneling model for metals and semiconductors[93,94] and the bond-breaking model for ionic solids and oxides[95,96]. To explain the cluster secondary ion emission which is most important in organic material characterization, two basic models were proposed[56]:

- In the cluster emission model, the cluster is emitted as such as a fragment of the surface layer.
- In the recombination model, the single atomic ions or neutral particles emit from the surface and recombine close to the surface.

The emission of large molecular ions in static SIMS can be explained using the cluster emission model[56]. Moreover, following the studies of Gerhard[97] and Oechsner[98] about the dimers emitted from different materials using the sputtered neutral mass spectrometry, the cluster emission is found for materials with strong (ionic) bonds while the recombination model is applicable for metals, alloys, and systems with comparable masses.

Benninghoven[99] gave an explanation for the cluster emission model as following. The preformed ions are supposed to be present at the sample surface before bombardment. When a projectile bombards the surface, an energy gradient is formed at the surface around the impact point. As a result, in an area close to the impact point, the molecules are strongly fragmented and emitted as atoms or small fragments. In an area further away from the impact point in the excited zone, large preformed molecular ions may be emitted.

Cooks et al.[100,101] proposed a more general model: the desorption-ionization model, where the emitted clusters are suggested to originate from both mechanisms. In this model, irradiation leads to the emission of preformed ions and to ions formed through ion/molecule reactions as well as through the dissociation of energetic (metastable) ions. The latter corresponds to the

unimolecular decomposition of secondary cluster ions ejected with high internal energies into smaller fragment ions and neutrals. The contribution of ions from this reaction can be determined by kinetic energy distribution (KED) measurements[102-104]. In some cases, this contribution can be as high as 50% of the total intensity in the mass spectrum[102,105].

Comparing the abundance distributions of charged and neutral clusters, Urbassek[106] found that the ejection process divides into two steps. At first, the cluster is formed in the neutral state, and it is ionized only while leaving the interaction range with the surface. The change of cluster ion distributions as a function of sputtering time is also discussed. Just after a sputtered cluster leaves the surface with high internal energy, it may fragment during the first 10 µs or more after the cluster generation[106]. Gnaser found similar results when observing the Si or C clusters sputtered from Si, SiC and graphite[103,104]. However, this metastable effect is more important for the static mode, where a pulsed ion beam is used, than in the dynamic mode where the surface is bombarded continuously.

II.1.2.iii.b. Use of Cs^+ primary ions

Implantation and desorption

The emission of secondary ions is very sensitive to the chemical states of the sample surface e.g. the presence of alkaline metals on the bombarded surface can enhance the emission of negative secondary ion[107].

Cs^+ primary ion beams are therefore widely used in SIMS to enhance negative secondary ion yields, thus improving detection sensitivity[108,109]. Negative secondary ion yields can be further improved by combining Cs^+ bombardment with the deposition of metallic Cs^0, either before or during SIMS analyses[110-112]. Moreover, the use of Cs in SIMS enables quantification through MCs_x^+ secondary ion detection[113-115]. Finally Cs^+ primary ion beams at low impact energy were recently successfully used for depth profiling of organic materials.

The desorption of Cs implanted into samples during the sputtering by Cs^+ primary ion beams has been studied by different authors[116-119]. Vandervorst et al. showed that Cs tends to migrate to and to desorb from the sample surface

at room temperature[118,119]. The fraction of desorbed Cs atoms must therefore be considered when estimating the Cs near-surface concentration[118-122]. This is of particular importance at low-energy Cs^+ bombardment, as these experimental conditions typically lead to high Cs concentrations at the sample surface.

To our knowledge the behaviour of implanted Cs in general and its desorption in particular have not yet been studied for organic materials.

Oxydation

Cs is extremely reactive and pyrophoric. Its oxidation is very complex because of the existence of a series of Cs oxides[123,124]. There are some well-described studies on the oxidation of Cs surface films deposited in high vacuum by Cs getters onto surfaces of Cu[123], Ag[125,126], Ru[122,127], Ni/Pt[128], GaAs[129,130] and InP[131] as well as on alternating Cs-graphite layers[124,132]. The authors were investigating the electronic properties of Cs oxides mainly by ultraviolet photoelectron spectroscopy (UPS) and X-ray photoelectron spectroscopy (XPS). In general, depending on O_2 exposure, Cs coverage, substrate structure, etc… the metallic Cs forms different Cs oxides with various stoichiometries, including suboxides (Cs_7O, Cs_4O, $Cs_{11}O_3$), oxide Cs_2O, peroxide Cs_2O_2 and Cs superoxide CsO_2[123-125].

Among the different oxide states of Cs, the peroxide Cs_2O_2 appears as an intermediate state that is formed before full oxidation to the superoxide. When the Cs peroxide is present on the surface, Cs oxides have been shown to form cluster structures: a two-dimensional structure for very thin layers[131] and a three-dimensional structure for thicker layers of Cs[125].

The oxidation mechanism of Cs proposed by Woratschek et al.[123] can be used to explain the observations described in Chapter 4 of this PhD thesis. After a very small dose of O_2, the Cs surface is covered by a monolayer of $Cs_{11}O_3$, where the O^{2-} ions are incorporated below the surface and the topmost layer contains merely the metallic Cs atoms. Once the $Cs_{11}O_3$ monolayer is formed, further diffusion of O_2 into the underlying Cs layer is slowed down. For a higher dose of O_2, as the topmost layer is metallic Cs, the dissociative adsorption of O_2 may continue and leads to the local build-up of rich oxygen zones at the surface. These oxygen atoms act as nucleation centres for the transformation

into Cs_2O_2. Finally, for a higher O_2 dose, the surface layer is completely oxidized into CsO_2, which then hinders the further penetration of oxygen into deeper layers. The outermost superoxide on the sample surface is considered to obstruct the penetration of O_2 into the bulk, thus hindering the transformation of deeper layers into superoxide.

To our knowledge, our work is the first one to study the oxidation of Cs implanted into organic samples during SIMS analysis.

II.1.2.iv. Secondary ion cluster distribution

Over the last few decades, the fragmentation and cluster formation of matter sputtered under ion bombardment in dynamic SIMS has been investigated in many studies[103,133-138]. It was found that the abundance of charged clusters fluctuates as a function of their size, while the distribution of the neutral clusters decreases continuously with the cluster size[133,134]. The oscillations in secondary ion intensity distributions of single species clusters are seen for metals, semiconductors and also carbon. For metals, the cluster emission occurs mainly in the positive spectrum, while for semiconductors and carbon the negative cluster ions are predominant[56].

Furthermore, this behaviour has been related to the variation of the ionization energy i.e. ionization potential for positive ion clusters and electron affinity for negative ion clusters, rather than to that of the binding energy. This is probably due to the fact that ionization probabilities of positive (negative) secondary ions sputtered from metals or semiconductors are proportional to the exponential of the ionization potential (electron affinity)[139] while the binding energies of clusters with similar size are comparable. The ejection process is assumed to occur in two steps: sputter emission of a neutral cluster followed by the ionization as it leaves the interaction range with the surface. The intensity oscillations in the mass spectra of cluster ions are therefore an artefact caused by ionization of the neutral clusters[134]. In the case of carbon negative clusters sputtered from graphite, a correlation between the abundance distribution and the electron affinity of the clusters was confirmed[103,136,137]. Results in literature are mainly limited to metals[133-135,140], alloys, some other polycrystalline or amorphous inorganic materials[103,136-138,141-144] and fullerite[145] or

C_{60}[138,146], but no dynamic SIMS studies on organic molecular thin films have been noted as of yet.

The alternations in the abundance distribution of C_n^- and C_mCs^- clusters (see Chapter III for experimental results) have been reported and investigated previously, but only at high impact energies on different allotropes of carbon (at 14.5 keV[103,136,137,142-144] and 5 keV[138] Cs^+ ion bombardment and at 4 keV SF_5^+, Xe^+ and Ar^+ ion bombardment[141]).

Results of Gnaser obtained with a Cs^+ beam at 14.5 keV impact energy on graphite and silicon carbide show odd-even alternations of C_n^- and C_mCs^- clusters with n[103,104,136].

Regarding the C_n^- clusters, an oscillation of the cluster abundances is observed for low values of n with the even-numbered clusters being more abundant than the odd-numbered clusters. From n=10 to n=14, the odd-even oscillations become less pronounced and above n=14, the odd-numbered clusters dominate. A similar behaviour is also observed when bombarding a fullerene substance by a 18 keV Cs^+ ion beam[145]. The oscillating distribution of C_n^- clusters has been attributed to a change in the cluster geometry which reflects also the variations of the electron affinity (EA)[103,136,143]. From ultraviolet photoelectron spectra (UPS) results, Yang et al[147] published the experimental electron affinity of neutral carbon clusters n=1-30 (Figure II.4). They proposed that at C_{10}^-, where the even-odd alternation changes, a transition from linear chain-like structures (n<10) to monocyclic rings (n>10) occurs. Later on, other authors suggested that for small neutral carbon clusters (n<10), the n-odd clusters have a linear structure with closed shell and low EA while the n-even clusters exist in two isomeric forms, one being linear and the other one cyclic[148,149]. The correlation between the C_n^- distribution and the electron affinity (the even-odd alternations and the change in distribution from n=9 to n=16) supports the electron tunnelling model developed for metals[135] where the secondary ion intensities of stable negatively-charged clusters are determined by the electron affinity[103,136,137,143]. For clusters of similar size, the differences in binding energy are small[103].

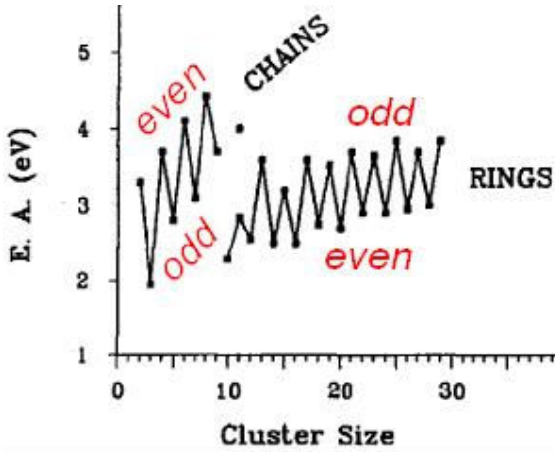

Figure II.4: *Electron affinity of neutral carbon clusters as measured by photodetachment thresholds of the negative cluster ions*[147].

The main differences between the C_n^- distributions obtained from SiC and from graphite are the stronger decrease with n of the cluster abundances and the less pronounced even-odd alternation for SiC[104]. The author explained these findings by the difference in carbon concentration in the two structures, as the formation of large clusters depends on the number of atoms in the vicinity of the cluster-emission site.

The C_mCs^- cluster distributions were found to be similar to the C_n^- alternations, but much more pronounced[103,104,136,145]. Throughout the C_mCs^- distributions, the clusters with an even number of C-atoms are in between one and two orders of magnitude more abundant than their odd-numbered neighbours. The most intense clusters are C_4Cs^- and C_6Cs^-. This agrees both with the variation of the binding energy of the ground-state isomers C_mCs^- (m=1–10) and the electron affinity of C_mCs clusters[150]. It has also been calculated that the C_mCs^- (m=4-10) ground state structure is composed of Cs^+ and C_m^{2-} where Cs is slightly embraced by C_m.

In addition to C_m^- and C_mCs^- clusters, $C_nN_x^-$ clusters are also of relevance in this PhD work. In this context, no results on nitrogen-containing samples have been noted as of yet. The only results that can be found on C_pN^- abundance distributions are from Gupta et al.[138]. They detected these clusters when sputtering different forms of carbon (phlycrystalline graphite, amorphous carbon and C_{60}) in the presence of N_2 and NO_2 gas. The C_nN^- (n up to 10) clusters exhibit an oscillating alternation with the odd p ions being relatively

more abundant than the even ones. According to this author, this abundance distribution relates to the electron affinity and the chain-to-ring transition does not occur up to p=10. Furthermore, Zhan's DFT calculations of C_pN^- (p =1-7) cluster structure correlate well with this even-odd alternations: his calculated vertical electron detachment energies (VDEs) and fragmentation energies show that the C_pN^- clusters with odd p are more stable than those with even p[151]. Moreover, his ab-initio calculations show that the anions C_2N^-, C_3N^- and C_5N^- have stable linear structures while the C_pN^- anions with larger odd values of p are slightly bent. C_pN^- anions with even p are all bent, except for p=2.

II.1.3. Depth profiling

The interaction between energetic ions and surface material results not only in the sputtering of particles but causes also some modification of the sample surface. Among them, sample damaging, recoil mixing, surface roughening and primary ion induced diffusion are important parameters that limit the depth resolution and complicate data interpretation in SIMS analysis. These phenomena depend on the bombardment parameters (primary ion energy, ion mass, incident angle) and on sample parameters (sample crystallinity, sample temperature, sample composition). In the next paragraphs, we will discuss in more detail the influence of these parameters on surface analysis in general and depth profiling in particular.

II.1.3.i. Damage formation

In the sputtering process, the number of ejected particles per incident ions (sputtering yield) is small compared to the total number of target atoms involved in the collision cascades. Therefore, the energy used for the ejection of particles, including surface-binding energy and kinetic energy of sputtered particles, is only a small fraction of the deposited energy. The largest amount of the energy is spent in the target and creates damage and heat. In inorganic materials, the irradiation-induced damage includes the displacement of target atoms due to the collisions with primary particles or with recoil atoms. In order to be ejected out of its original position in the lattice, a target atom has to

receive an energy higher than the displacement energy or threshold energy, which is in the order of ~10 eV. The number of displaced atoms per bombarding ion increases with projectile size[56] as well as with impact energy[152].

For a low fluence (static SIMS), the number of primary ions hitting the surface is small so that only a fraction of the surface is irradiated. The damage is isolated in space-separated zones. Therefore, only a heavily disordered region is formed along the trajectory of projectile ion, or energetic recoil atoms. The size of this damage zone depends on the projectile mass, bombardment energy and target mass. In this case, the mean depth of origin of sputtered particles is expected in the order of mainly two monolayers[56,153].

For a high fluence (dynamic SIMS), the individual damaged regions overlap and lattice damage becomes more important. In this situation, an atom can be relocated many times before being ejected. At about 1 keV, the bombardment-induced broadening may range between 2 and 4 nm[154,155]. Material damaging due to irradiation includes surface amorphization, material swelling and radiation-induced diffusion. When the lattice defects created by displaced atoms increase and agglomerate, the material may become amorphous. This effect is more pronounced for some materials i.e. semiconductor and brittle crystalline structures (T_c superconducting ceramics) and less in others e.g metals[83]. The swelling is a collective flow of matter towards the surface to balance the injection and accumulation of primary ions in the bulk. This effect is more pronounced for organic materials[156,157]. The radiation-induced diffusion is the diffusion of vacancies and interstitials into the undamaged bulk due to thermal diffusion[69,158].

The abovementioned irradiation-induced damage has mostly been studied for inorganic materials; however, the deductions are still true for organic matter. Moreover, in organic materials, the irreversible damage (fragmentation and cross-linking) due to ion irradiation has to be taken into account. For example, in many polymers, the ion bombardment can create scission, cross-linking and branching which change dramatically the physical properties of materials[159]. These damages cause the loss of sample information when depth profiling.

For organic materials, the damage can be reduced or controlled by carefully choosing the primary ion beam, i.e. the primary ion species and the impact

energy. At a same impact energy, a monoatomic ion beam is shown to induce heavy damage, i.e. bond breaking, structure change, carbonization on the film surface, whereas a cluster ion beam creates much less damage on the organic surface[160,161]. The difference observed for these two kinds of ion beams is due to the energy deposited on the sample surface and the sputter yield. When a cluster ion impacts on a surface, it fragments to smaller clusters or atoms, which have only a fraction of the initial energy of the whole cluster. This results in a high sputter yield and a low thickness of the damaged layer[162]. In the case of a monoatomic primary ion, only a small fraction of the impact energy is used for the sputtering in the near surface region while the rest extends deeply into the substrate and causes damage and mixing[162,163]. A reduction of the impact energy is necessary for reducing this damage when using a monoatomic primary ion. Moreover, a reactive primary ion can enhance or reduce the fragmentation or cross-linking on organic samples. For example, for some organics, the use of a Cs^+ primary ion beam allows cross-linking during sputtering to be prevented as free radicals react with the implanted Cs[164,165]. However, for some other organics (e.g. molecules containing a large number of oxygen atoms) the opposite trend is observed as Cs reacts with the molecules themselves and fragments them[165,166].

II.1.3.ii. Recoil mixing

When the recoil atoms are displaced in a multi-component target, they cause an intermixing of the components called recoil mixing. In depth profiling, this reduces the depth resolution. There are two types of recoil mixing[56]:

- Primary recoil mixing is the displacement of target atoms in a direct collision with primary ions.
- Cascade mixing is the displacement of target atoms in a collision with other recoil (target) atoms.

For low-energy bombardment, the depth of the mixed region is defined by the implantation range of the incident ions. Therefore, in this case, the primary recoil mixing is the main contribution. Figure II.5 shows Molecular Dynamics (MD) and Monte-Carlo (MC) simulation results for Ar bombardment at 500 eV on a Si substrate. As the Ar primary ion range in this condition is of 40 Å, the

Si atoms in the depth of 40 Å are fully mixed after a fluence of $1.25x10^{16}$ atoms/cm^2. Thus, the depth resolution of this system is limited to 40 Å at the best.

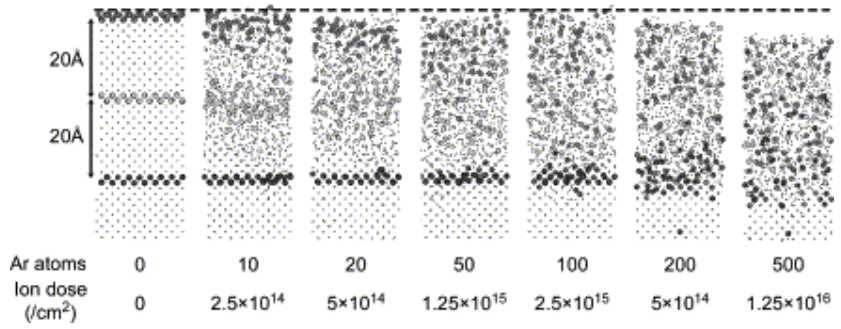

Figure II.5: *Snapshots of the mixing of a Si substrate under 500 eV Ar impacts calculated by MD simulations. Large circles present the marker Si atoms, which are initially positioned at 0, 20, 40 Å*[167]*.*

The influence of the impact energy on primary recoil mixing for a large range of materials was studied extensively by simulation[155,168-171]. These studies show that the cascade mixing can be minimized when using heavy projectiles, low impact energies and oblique incidence angles.[155,168-170]. The impact of mixing in depth profiling is evidenced by the distortion in the depth profile. In addition to the recoil mixing, the diffusion of material in the average damage depth due to the displacement of atoms to vacancies is also a reason of the profile distortion[172,173].

While the previous conclusions were drawn from studies focusing on inorganic materials, they remain true for organic materials. Studies by Delcorte et al.[174] based on TRIM simulations reveal the advantage of low impact energy and glancing incident angle when bombarding organic materials. These studies also highlight the influence of the primary ion species and the nature of the sample on recoil mixing in organic materials. Again, molecular or cluster ion beams are shown to reduce the mixing zone in comparison to monoatomic ion beams (see Figure II.6) [162,163]. Figure II.6 shows that, at the same impact energy, Ar penetrates much deeper into a polystyrene (PS) sample than C_{60}. The Ar ion causes several bond-scissions and a cascade of collisions extending deeply into the sample, causing extensive damage. In comparison, the damage created by the C_{60} is limited to the first 2 nm.

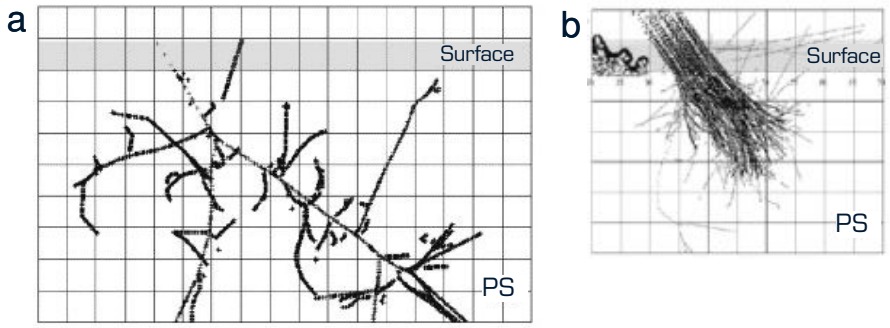

Figure II.6: *Tracks of the atoms forming the collision cascade in a polystyrene tetramer. The successive positions of the projectile and recoil atoms with more than 10 eV of kinetic energy are represented as a function of time up to 200 fs. Each square of the grid is 5 × 5 Å^2. The sample-vacuum interface is indicated by the gray area. (a) Ar → PS, 5 keV, (b) C_{60} → PS* [162].

In summary, both for inorganic and organic materials, the recoil mixing zone can be reduced by using a cluster beam or a monatomic beam with heavy projectiles, oblique incident angle and low impact energy. This reducing may ameliorate the depth resolution and minimize the profile distortion.

II.1.3.iii. Surface roughness

The development of surface roughness under energetic ion bombardment has been investigated in numerous studies. The results show that surface roughening depends on several parameters i.e. fluence of primary ion beam, angle of incidence, ion energy, surface crystallinity, … Depending on ion fluence, one can distinguish three types of surface roughening[56]:

- For low-fluence (10^{11}-10^{15} ions/cm^2), the crystallinity of the target does not change for almost any types of materials.
- For medium-fluence (10^{15}-10^{17} ions/cm^2), the initial stage of sputter-induced roughness is observed. For increasing fluence, large clusters, dangling dislocation and bubbles form first, and then dislocation starts and complex configurations appear.
- For high-fluence (>10^{17} ions/cm^2), many types of surface structures develop i.e. steps, ridges, grooves…

The reasons for surface roughness development during sputtering are the diffusion of atoms on the surface[56,175] and the variation of the sputtering yield with the local impact angle, which is depending on the topography, and with the crystal orientation[83,153]. Bradley and Harper's theory of ripple formation[175,176] shows that a surface element with convex geometry is eroded faster than that with a concave geometry, thus this induces an instability on the surface and leads to the formation of roughness. While most of the studies focussing on surface roughness formation concentrated on inorganic materials, the conclusions remain true to some extent for organic materials.

For reducing the surface roughness during bombardment, Zalar[177] and Bulle[178] proposed either sample rotation or oblique incidence of the ion beam. Another way to control roughness, mainly for organic materials, consists in adjusting the temperature of the sample. Low or high sample temperatures during the analysis can reduce the surface roughness comparing to room temperature conditions[179-182]. The reduction of sputtering-induced roughness observed for instance at –75 °C for poly(methyl methalcrylate) (PMMA) is due to the change of polymer properties (improved inter- and intrachain coupling) resulting in a uniform sputtering[181]. At high temperature, the depolymerization reaction is considered to increase main-chain scission and decrease side-chain loss and cross-linking. As a result, the sputter rates increase and the overall damage accumulation decreases[181]. Finally, the use of large cluster ions also considerably reduces the sputtering-induced roughness [183,184]. In this context, a large variety of different clusters have been studied: C_{60}^{n+} [185-189], Au_n^{q+} (5<n<400, 1<q<4)[190,191], SF_5^+ [180,181,192] and Ar_n (n=500-2000)[161,193-195].

II.1.3.iv. Radiation-induced broadening of depth profiles

II.1.3.iv.a. Influence of primary ion beam

All published experimental data show that[153,196], for a given primary ion species and a fixed impact angle, the profile broadening increases with impact energy. The relation between the interface width Δz_s in a depth profile and the impact energy E_o is described by[70,153]:

$$\Delta z_s = k_s E_o^m \qquad \text{(II.3)}$$

where k_s is a factor depending on the analyzed sample (layer/substrate combination, interface location, sample temperature) as well as on the primary ion beam (primary ion mass, impact angle). This energy dependency of the interface width is related both to mixing effects and to surface roughening.

The depth resolution can be expressed using the growth λ_g and decay λ_d lengths. These growth/decay lengths represent the distance over which the measured signal increases/decreases by a factor e, leading to $I \propto \exp(\pm z/\lambda)$, where I is the detected intensity and z the depth.

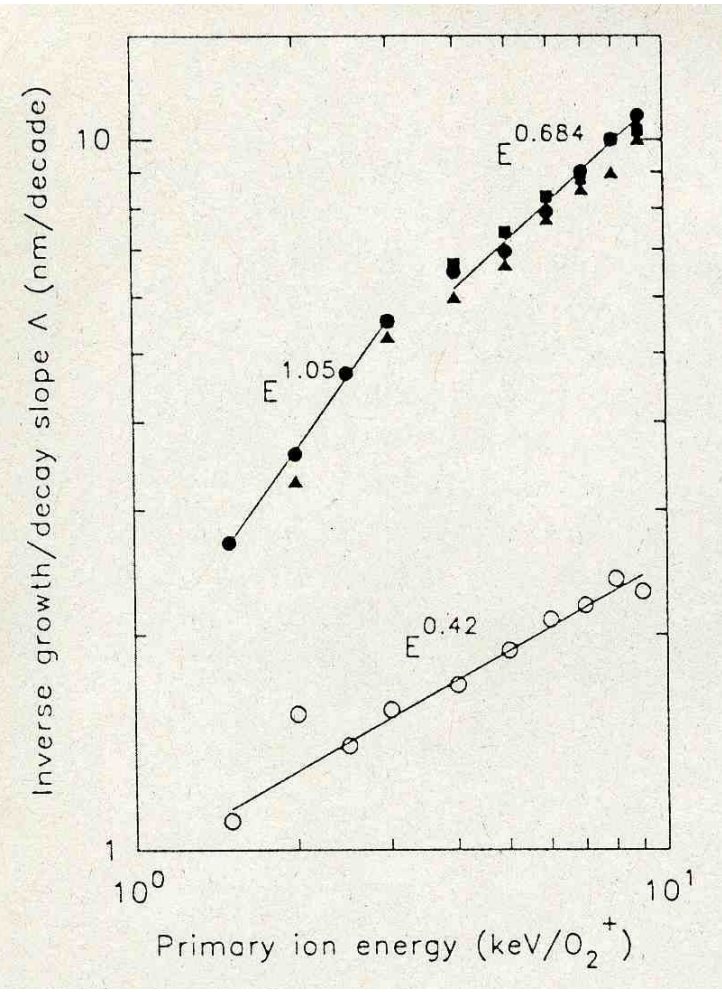

Figure II.7: *Growth (open symbols) and decay (filled symbols) length data as a function of impact energy for an analysis with $^{16}O_2^+$ primary ions of boron deltas and thicker layers in silicon: square symbol for molecular beam epitaxy (MBE) delta sample with 500 nm cap analyzed at 45°, circle symbol for MBE delta sample with 500 nm cap analyzed at normal incidence and up triangle symbol for MBE delta sample with 50 nm cap analyzed at normal incidence*[70].

Considering in addition a non-energy dependent factor δz_0, the broadening depth becomes[70]:

$$\delta z = \delta z_0 + kE_p \qquad (II.4)$$

δz_0 is characteristic for the true feature shape and sources of roughness-like behaviors i.e. intrinsic surface topography, interface roughness, statistical effects of sputtering, … which do not or may not depend on impact energy. The situation can be summarized through Figure II.7, which shows the log-log plot for boron growth and decay length data after correcting for a non-energy dependent broadening assumed to be ~1 nm. The impact energy has a stronger effect on the decay length than on the growth length, as shown in Figure II.7.

The depth resolution also depends on the angle of incidence of the primary ion beam[70,88,155]. Andersen[155] suggests that the interface width Δz decreases with sputter yield Y:

$$\Delta z \propto Y^{-1/2} \qquad (II.5)$$

Taking into account that the sputtering yield Y varies with the incident angle (cf section II.1.2.ii), one obtains the following relationship:

$$\Delta z\,(\theta_{in}) \sim \Delta z\,(0°)\,\cos^{s/2}\theta_{in} \qquad (II.6)$$

Therefore, an increase of the incident angle increases the sputter yield and reduces the sputter-induced broadening.

To optimize depth profiling, i.e. to reduce damage range and mixing, the use of heavy projectiles at low impact energies or large cluster ion beams and quite oblique incident angles are essential. At the same time, too oblique incidence leads to increased particle and energy reflection[83] or roughness formation[197-199]. The latter can be avoided or controlled by using sample rotation[177,200], gas flooding[200,201] and temperature control[180,182].

II.1.3.iv.b. Influence of sample nature

For given analysis conditions, the bombardment induced effects, e.g. mixing, roughening … depend on the sample. An amorphous material or a single crystal, which turns amorphous under ion bombardment, leads to a uniform erosion rate on the surface and to a good depth resolution[153]. Polycrystalline

metals develop huge surface roughness during bombardment due to the different sputter rates for the different crystalline orientations and therefore lead to a loss in depth resolution[153]. For organic materials, the quality of the depth profiling depends on the structure and properties of the material. The characterization can only be successful if the experimental conditions are chosen carefully (i.e. the primary ion nature, the beam angle and energy and the sample temperature)[165,202]. Finally, the density of the target has an influence on the sputtering processes and consequently also on depth profiling[203-206].

II.1.4. SIMS instruments

II.1.4.i. Cameca SC-Ultra

II.1.4.i.a. Description of the instrument

***Figure II.8**: Cameca SC-Ultra instrument. The primary column is hidden behind the mass spectrometer.*

The Cameca SC-Ultra instrument[207] is a SIMS instrument for ultra-shallow depth profiling. Based on this objective, the instrument is designed for using low impact energies. The SC-Ultra installed at CRP-Gabriel Lippmann has a floating primary column at 60° with a Cs^+ surface ionization source and a duoplasmatron O_2^+ source. It is equipped with a magnetic sector mass

spectrometer and an electron gun for charge compensation (Figure II.8). The analysis chamber connects to an airlock used for the sample transfer.

II.1.4.i.b. Experimental conditions

All experiments on the Sc-Ultra instrument were performed using a Cs^+ primary ion beam at impact energies in the range of 250 eV – 10 keV in positive and negative secondary ion mode. The different impact energies resulted in different incident angles due to the influence of the extraction field. The mass resolution $\frac{M}{\Delta M}$ was set to 400. A contrast aperture of 300 µm was used and the energy slit was closed to a width of 45 eV. The raster size was set to 300 x 300 μm^2. The combination between a field aperture having a diameter of 1200 µm and an electronic gate set to 70% resulted in a diameter of the analyzed area of 70 µm. For samples with thick organic layers, charging effects appeared. In these situations, the electron gun was used for charge compensation. The electron current was varied in the range of 0.5-2.1 mA. When studying roughness formation during Cs^+ bombardment, sample rotation was used at low-energy bombardment. The rotation speed was set to 20 rpm. The pressure in the analysis chamber typically was $3 \cdot 10^{-8}$ mbar.

More details about analysis conditions are listed in tables II.1 and II.2. For some energies, the real impact energies depends on the sample voltage, mainly because the primary ion beam cannot be focused onto the surface below a given impact energy. To avoid any confusion in the forthcoming chapters, the nominal impact energy will be used.

Nominal impact energy	250 eV	500 eV	1 keV	5 keV	10 keV
Impact energy	250 eV 260 eV	500 eV 560 eV 517 eV	1 keV	5 keV	10 keV
Sample Voltage	-2 kV	-2 kV -3 kV	-2 kV -3 kV	-2 kV	-5 kV
Incidence angle	38°	47°	51°	56°	56°
Primary current	3-13 nA	3-21 nA	1.5-12 nA	1.3-2 nA	1.7 nA

Table II.1: *Experimental conditions in negative mode.*

Nominal impact energy	500 eV	1 keV
Impact energy	550 eV; 568 eV	1 keV
Sample Voltage	3 keV	3 keV
Incidence angle	64°	63°
Primary current	2.5-11 nA	3-11 nA

Table II.2: *Experimental conditions in positive mode.*

II.1.4.ii. Cameca NanoSIMS50

II.1.4.ii.a. Description of the instrument

The Cameca NanoSIMS50 instrument is a dynamic SIMS for surface imaging. It is capable of achieving a lateral resolution down to 50 nm combined with a high mass resolution ($M/\Delta M > 5000$) and a high transmission of 70%. Images of 5 different ions in the mass range from H to U can be recorded simultaneously with detection limits down to the ppm. Moreover, a three

dimensional image can be reconstructed by imaging layer by layer. With all of these advantages, the NanoSIMS50 is a powerful instrument for surface analysis in various fields including biology, geology and materials science[72,208-210]

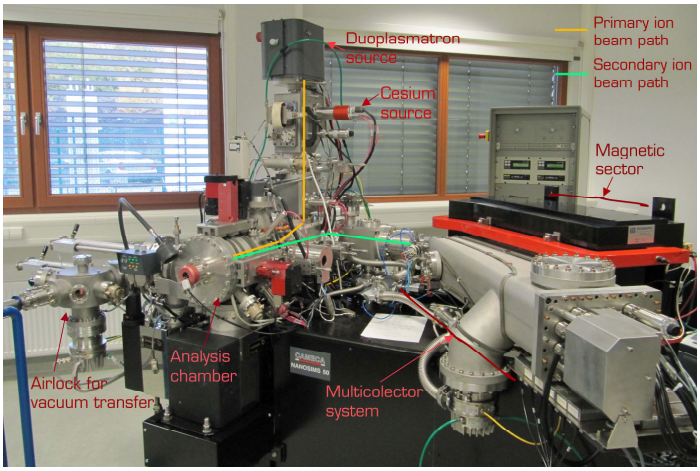

Figure II.9: *Photo of Cameca NanoSIMS50 instrument.*

The NanoSIMS50 is equipped with a surface ionization source for Cs^+ primary ion beam and a duoplasmatron ion source for O_2^+, O^- and O_2^- ions. The primary ion beam hits the sample at normal incidence. The same optics are used to focus the primary ion beam onto the sample and to extract the secondary ions. A double focusing mass spectrometer is used for mass separation. By using high impact energy for primary ions and high energy for secondary ions, the probe diameter can be minimized and the transmission of the mass spectrometer maximized.

II.1.4.ii.b. Experimental conditions

The Cameca NanoSIMS50 instrument was used in this PhD work to investigate the effect of vacuum storage and air contact on artefacts in Cs implanted samples. For sample transfer under UHV conditions, a lab-built UHV suitcase[211] was used to exchange samples between the Cameca SC-Ultra instrument and the Cameca NanoSIMS50 instrument.

All images were recorded using a Cs^+ primary ion beam with an impact energy of 16 keV and a current of 1.5 pA. The probe with a diameter of about 80 nm was raster-scanned over an area of 10 x 10 μm^2. Each image contained 256 x 256 pixels. The signals of $^{12}C^-$, $^{16}O^-$, $^{12}C^{14}N^-$, $^{28}Si^-$ and $^{107}Ag^-$ secondary ions

were collected with a counting time of 20 ms per pixel. The mass resolution $\frac{M}{\Delta M}$ was set to 4500.

II.2. Other techniques used for surface analysis

II.2.1. Atomic Force Microscopy

II.2.1.i. Description of the technique

Atomic force microscopy (AFM) is a very high-resolution scanning probe microscopy, with lateral resolutions down to the angstrom. It is capable to characterize a wide range of materials surfaces, including polymers, ceramics, composites, glass and also biological samples[212,213].

The basic part of an AFM instrument is the cantilever with a sharp tip at its end, which is used to scan the surface. The cantilever is made of silicon or silicon nitride and its tip has a radius of curvature in the range of nanometres. During the scanning, the tip is brought close to the sample surface. This approach creates forces between the tip and the sample, which then deflect the cantilever. This deflection is measured using a laser which reflects from the cantilever surface onto a position-sensitive detector. From the measured deflection of the cantilever, the force between the tip and the sample is calculated[214].

To avoid damaging the tip by collisions with the sample surface while scanning, a feedback mechanism is used to adjust the distance between the tip and the sample. Thus, the sample plate is mounted on a piezoelectric system, that allows controlling the tip-to-sample distance for maintaining a suitable force, and also moving the sample in the XY plane while scanning the sample[214].

Depending on the objective, the operator can choose between contact mode, non-contact mode or tapping mode. In contact mode, which is useful for small

and high resolution scans[214], the tip is constantly adjusted to maintain a constant force, thus at a constant height very close to the sample surface. In non-contact mode, the cantilever is oscillated further above the sample surface compared to the contact mode. Better lateral resolution and less tip damage is obtained by the tapping mode which is a combination of the two aforementioned modes. In the tapping mode, the cantilever is oscillated closer to the sample surface than in the non-contact mode, such that the tip periodically touches the surface.

II.2.1.ii. Molecular Imaging PicoSPM LE instrument

The Molecular Imaging PicoSPM LE[215] instrument, which was used for this work, is a high-resolution AFM instrument that can operate at either contact mode, non-contact mode or tapping mode. The configuration and typical parameters are presented in table II.3.

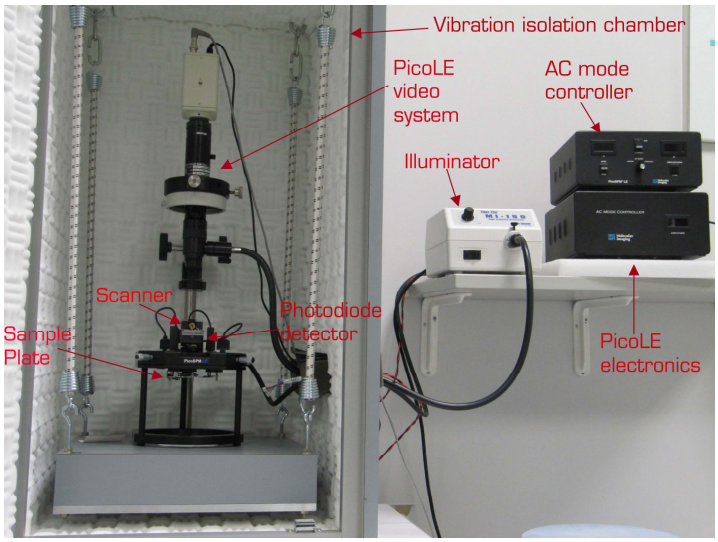

***Figure II.10**: PicoSPM instrument.*

Scanners (X,Y,Z)		
Large	Scan size	100x100x7 μm^3
	Noise levels	< 10 Å RMS (lateral) < 0.5 Å RMS (vertical)
Small	Scan size	10x10x2 μm^3
	Noise levels	< 1 Å RMS (lateral) < 0.1 Å RMS (vertical)
Video Viewing system		
Magnification to CCD		x1200 max
Lateral resolution		2 μm
Field of view		~ 1.5 mm

Table II.3: *Parameters for scanners and video viewing system.*

II.2.1.iii. Experimental conditions

All measurements were performed at ambient air in the tapping mode with a scanning area of 5x5 μm^2 and 20x20 μm^2. The image resolution was 512 x 512 pixels. The cantilever was made of n-type silicon and had a length of 125 μm, a width of 40 μm and a thickness of 4 μm. Its spring constant was 25 -75 N/m. The resonant frequency was between 200-400 kHz. The tip height was in the range of 12-16 μm and its radius was less than 10 nm. After measurement, the RMS roughness was calculated from topography images using the software Gwyddion[216].

II.2.2. Auger Electron Spectroscopy and X-Ray Photon Spectroscopy

Auger electron spectroscopy (AES) and X-ray photoelectron spectroscopy (XPS) are analytical techniques that provide information on the elemental surface

composition[217-219]. In both techniques, the surface is excited by energetic particles (electrons or photons) bombardment which results in an electron emission from the near-surface atoms. By analysing the kinetic energy of the ejected electrons, information on the chemical composition of the topmost surface layers is obtained. Despite a poor detection limit (0.1-1 at%) compared to SIMS, AES and XPS are used in this study to quantify the Cs^+ bombarded surfaces before and after contact with air.

II.2.2.i. Auger Electron Spectroscopy

II.2.2.i.a. Description of the technique

Auger electrons are emitted from a depth ranging from 1 to 10 nm.The atoms situated at 1~2 µm under the surface are excited by an irradiation of energetic electrons. The core state electron (electron energy E_X) can be removed and leaves behind a hole. A secondary electron from an outer shell (electron energy E_Y) fills the hole. The transition energy between the first and second electron energy states can be transfered to a third electron of an outer shell (electron energy E_Z). If the retained energy is higher than the orbital binding energy, the electron is emitted from the atom with a kinetic energy of:

$$E_{kinetic} \approx E_X - E_Y - E_z \qquad (II.7)$$

The Auger spectrum showing electron intensity as a function of kinetic energy gives therefore information on surface elemental composition. Furthermore, E_z depends slightly on the local environment around a given atom and gives thus chemical information.[219-221]

II.2.2.i.b. ThermoVG Microlab 350

The ThermoVG Microlab 350 equipped with a field emission gun and a X-ray gun is capable of analysing both in AES and XPS modes. In AES mode, a spatial resolution of 20 nm is achievable. Figure II.11 shows a picture of the instrument.

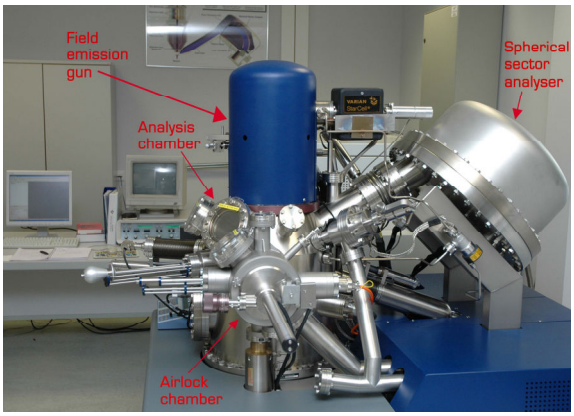

***Figure II.11**: ThermoVG Microlab 350 instrument*

II.2.2.i.c. Experimental conditions

The AES analysis was used to study the effects of a low-energy Cs^+ primary ion beam on the composition of an organic surface. Both chemical mapping and quantification of the surface composition were performed in the VG Microlab350 instrument. The pressure in the analysis chamber was $5 \cdot 10^{-9}$ mbar. A Cs image of 6.25 x 4.6 μm^2 was recorded using an electron beam with an energy of 10 keV and a current of 2 nA.

II.2.2.ii. X-ray photoelectron spectroscopy

II.2.2.ii.a. Description of the technique

In XPS, a X-ray beam irradiates the sample and ejects core-level electrons from sample atoms. The kinetic energy of the ejected electrons from the top 1 to 10 nm of the material is analyzed. The binding energy of electrons can be determined as below:

$$E_{binding} = E_{photon} - E_{kinetic} - \Phi_{spectrometer} \qquad (II.8)$$

Where $E_{binding}$ is the binding energy of the electron, E_{photon} is the energy of the X-ray photons, $E_{kinetic}$ is the measured kinetic energy of the emitted electron and $\Phi_{spectrometer}$ is the work function of the spectrometer.

The binding energy provides information on sample elemental composition, as well as on chemical and electronic state of the elements in the sample[219].

II.2.2.ii.b. Kratos Axis Ultra DLD

In contrast to the ThermoVG Microlab 350, the Kratos Axis Ultra instrument is dedicated to the XPS mode and allows for a higher energy resolution and better lateral resolution. The spot can be reduced to a minimum diameter of 10 µm which allowed for analyses inside our SIMS craters.

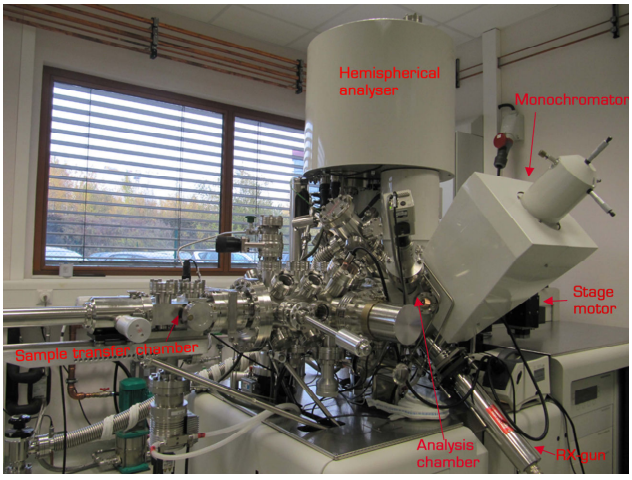

Figure II.12: *Kratos Axis Ultra DLD instrument*

II.2.2.ii.c. Experimental conditions

Analysis of the surface composition in the Kratos Axis Ultra DLD XPS instrument were performed with a monochromatic Al Kα radiation (E = 1486.6 eV). The X-ray source was operated at 100 W. The diameter of the analyzed area had a size of 110 µm and the photoelectron take-off angle was 90° with respect to the sample surface. The energy resolution of the spectrometer was set to 0.5 eV and the pressure in the analysis chamber was $1 \cdot 10^{-9}$ mbar. Samples with Cs implanted craters were analyzed before and after air exposure.

Chapter III
Fragmentation study of organic samples

As presented in II.1.3, depending on the primary ion type and the impact energy, sample damage can be created to different extents. Results from literature show that at high-energy Cs^+ bombardment, the C containing materials are graphitizing and that organic information is lost[103,136-138,141-144]. Nevertheless, recent studies using Cs^+ bombardment at low impact energies for sputtering of polymers in Tof-SIMS prove that some of the organic structure of organic molecules can be maintained during the depth profiling[165,222,223]. However, this possibility has not been verified in dynamic SIMS with a magnetic sector mass spectrometer and the molecules used in this study.

The objective of this chapter is to investigate the possibility of maintaining structural information for different organic molecules (C_{60}, CuPc and Alq_3) under low-energy Cs^+ bombardment in dynamic SIMS and to identify secondary ions that are typical for the abovementioned organic molecules. Thus, this chapter will provide the background information that is necessary for the depth profiling in the forthcoming chapters. The mass spectra of the different organic molecules are compared for different impact energies in steady-state conditions. The abundance distribution of C_n^- and C_kCs^- clusters are characterized and compared to results in literature at high impact energies. Finally, the best fragments for the characterization of interfaces in bi-layered samples by depth profiling in dynamic SIMS will be chosen. The characterization of the interfaces will be described in chapter V.

III.1. Samples and characterization

For the fragmentation study, the samples S1, S2 and S3 are used. The organic layers are deposited onto silicon wafers at room temperature. Details about samples and preparation processes are described in I.4. Table III.1 presents the samples.

Sample	Organic molecule	Layer thickness (nm)
S1	C_{60}	43
S2	Alq_3	100
S3	CuPc	150

Table III.1: *List of samples.*

The fragmentation of the organic molecules is studied by recording mass spectra in the negative mode on the Cameca SC-Ultra instrument. The secondary ion intensities are recorded between 11 amu and 325 amu under steady-state conditions. Results for the positive mode will not be shown because the mass spectra show only a few monoatomic secondary ion peaks and the peaks have quite low intensities. Impact energies of 250 eV, 500 eV, 1 keV, 5 keV and 10 keV are chosen. For insulating samples (CuPc and Alq_3), the electron gun is used for charge compensation. More details about characterization conditions are in II.1.4.i.b.

III.2. General presentation of mass spectra

In this paragraph, a general overview over the different mass spectra will be given and some differences between the mass spectra of the different molecules will be shown. A more systematic study of the fragmentation will follow in the next paragraphs.

The mass spectra of Alq_3, C_{60} and CuPc recorded at impact energies of 250 eV, 500 eV, 1 keV and 5 keV are compared to each other. Figures III.1 and III.2 present the mass spectra for the mass range from 11 amu to 170 amu and from 170 amu to 325 amu, respectively. The mass spectra of sample C_{60} show more well-defined periodic peaks than those for samples Alq_3 and CuPc. This is due to the varying compositions of the molecules: C_{60} contains only carbon, so that all major peaks are formed of the carbon isotopes and some contaminations. For CuPc, nitrogen is also present in the molecules, and Alq_3 contains oxygen in addition. This results in more complex mass spectra for the two latter molecules. Details will be discussed later.

As described in II.1.2, when increasing the impact energy and the incident angle, the sputtering yield increases and thus the secondary ion intensity should increase. However, for a given sample the intensities of the mass spectra do not change much when changing from 500 eV to 1 keV but decrease significantly at 250 eV. This is explained by the variation of the current of the primary ion beam. The primary current is of 7 nA for the impact energies of 250 eV and 500 eV and is reduced to 2 nA at 1 keV. Reducing the primary current allows controlling the sputter rate so that the mass spectra of a given molecule should not exceed into the Si substrate. Thus, reducing the primary current compensates the increase in sputter yield for the higher impact energies at 1 keV. The decrease of peak intensities at 250 eV is due to a reduced sputter rate compared to 500 eV. Moreover, at 250 eV the ratio between high peak intensities and small peak intensities is smaller than for the higher impact energies (Figure III.1). This is possibly due to emission of different fragments at low energies as well as changed reactions with residual gas atoms (hydrogen, nitrogen and oxygen …) in the analysis chamber at 10^{-8} mbar.

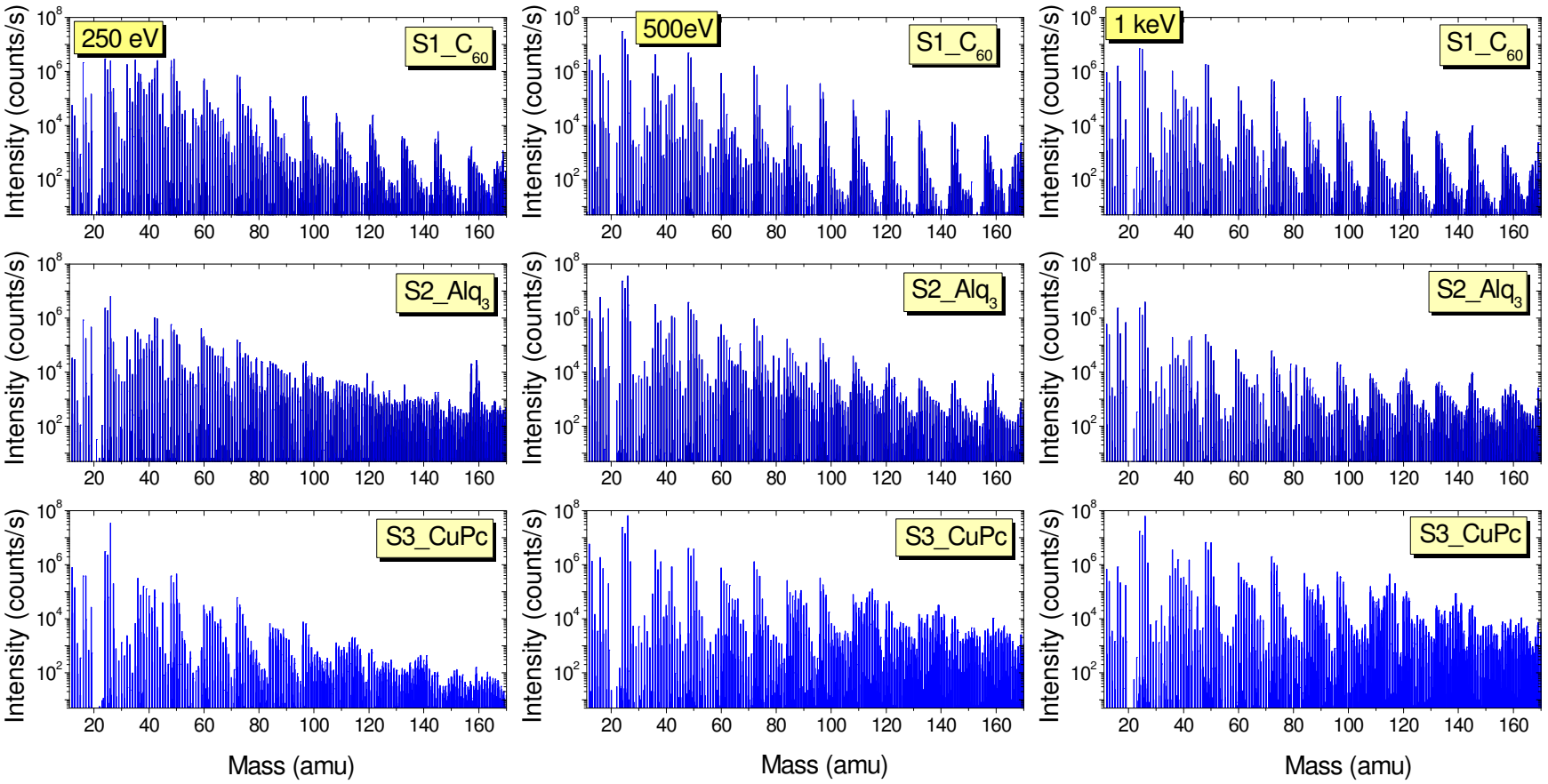

Figure III.1: *Mass spectra of S1_C60, S2_Alq3, S3_CuPc at different impact energies (mass range from 11-170).*

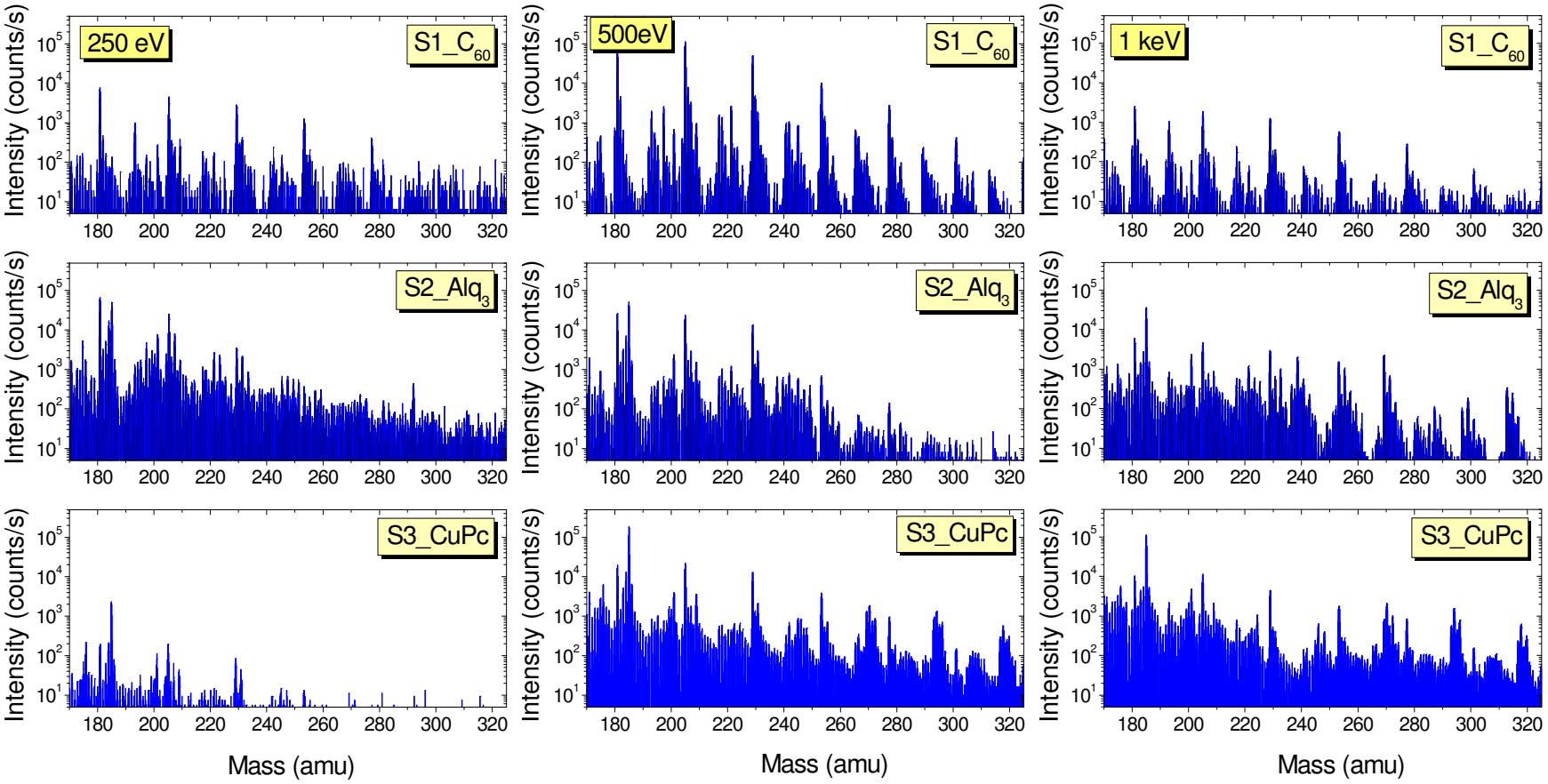

Figure III.2: *Mass spectra of S1_C_{60}, S2_Alq_3, S3_CuPc at different impact energies (mass range from 170-325).*

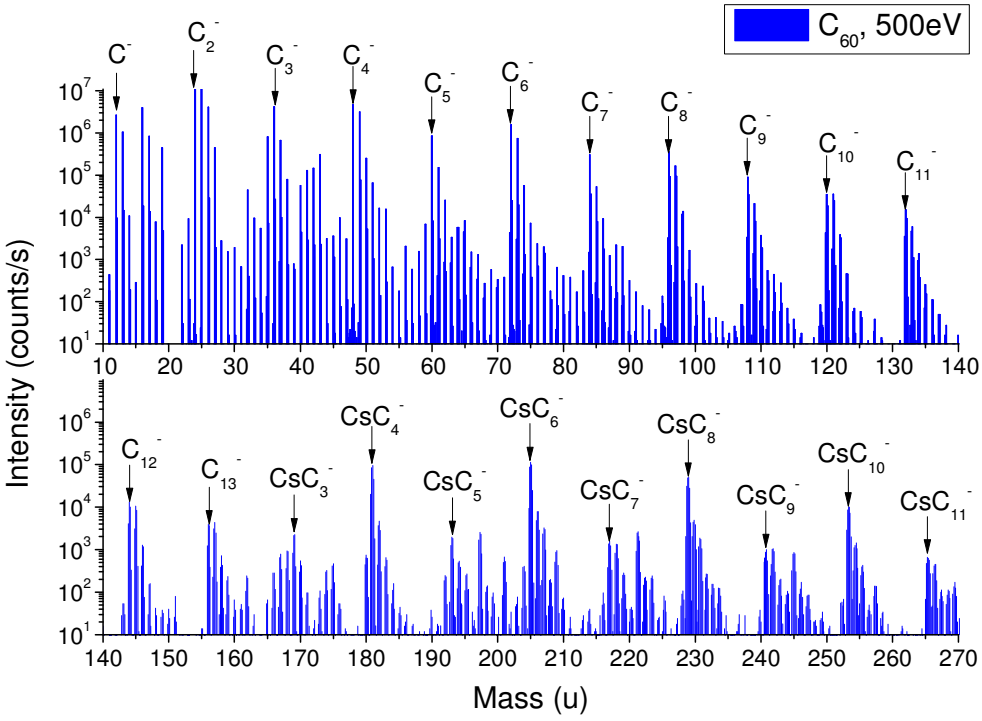

Figure III.3: *Mass spectrum of S1_C_{60} at an impact energy of 500 eV.*

Figure III.3 shows the mass spectrum of C_{60} at 500 eV. The most important peaks have been identified. As C_{60} contains only the different carbon isotopes, its mass spectrum contains mainly clusters of carbon isotopes i.e. the high peak intensities are C_n^-, C_kCs^- clusters as well as some clusters with carbon atoms combined with atoms from residual gas in the analysis chamber such as hydrogen, nitrogen, and oxygen ($C_nH_x^-$, $C_kH_xCs^-$, … clusters).

For Alq_3 and CuPc samples, both molecules contain nitrogen and/or oxygen in addition to carbon which results in a larger variety of secondary ion clusters. Thus the mass spectra contain more information than the C_{60} sample. For the different molecules, characteristic peaks are identified. Figures III.4, III.5 and III.6 zoom into the mass spectra at 1 keV for the mass ranges of 50-100, 100-150 and 150-200 amu, respectively. Some typical peaks are compared for this energy. At all other impact energies, the trend is similar. In Figure III.4, the peaks at 79 and 81 amu are much more important in the mass spectrum of Alq_3 than in any other. These characteristic twin peaks correspond to $AlC_2N_2^-$ and $AlC_2N_2H_2^-$. The mass spectrum of CuPc contains some similar peaks at 115 and 117 amu coming from the $CuC_2N_2^-$ and $CuC_2N_2H_2^-$ clusters. There is

one additional peak at 139 amu due to $CuC_4N_2^-$ (Figure III.5). Compared to the mass spectrum of C_{60}, the mass spectra of Alq_3 and CuPc show an important peak at 185 amu which is due to the $C_2N_2Cs^-$ cluster (Figure III.6). Thus, the different molecules can be identified using characteristic peaks of the mass spectra recorded in the negative mode. However, no typical peak corresponding to the whole molecular structure, or fragments larger than the $MC_2N_2H_2^-$ or $MC_4N_2^-$ clusters could be found for Alq_3 and CuPc. This suggests that the organic molecules undergo a strong fragmentation during low-energy bombardment. In the next section, these fragmentation mechanisms will be studied more in detail by looking at some cluster abundance distributions of high intensity cluster ions.

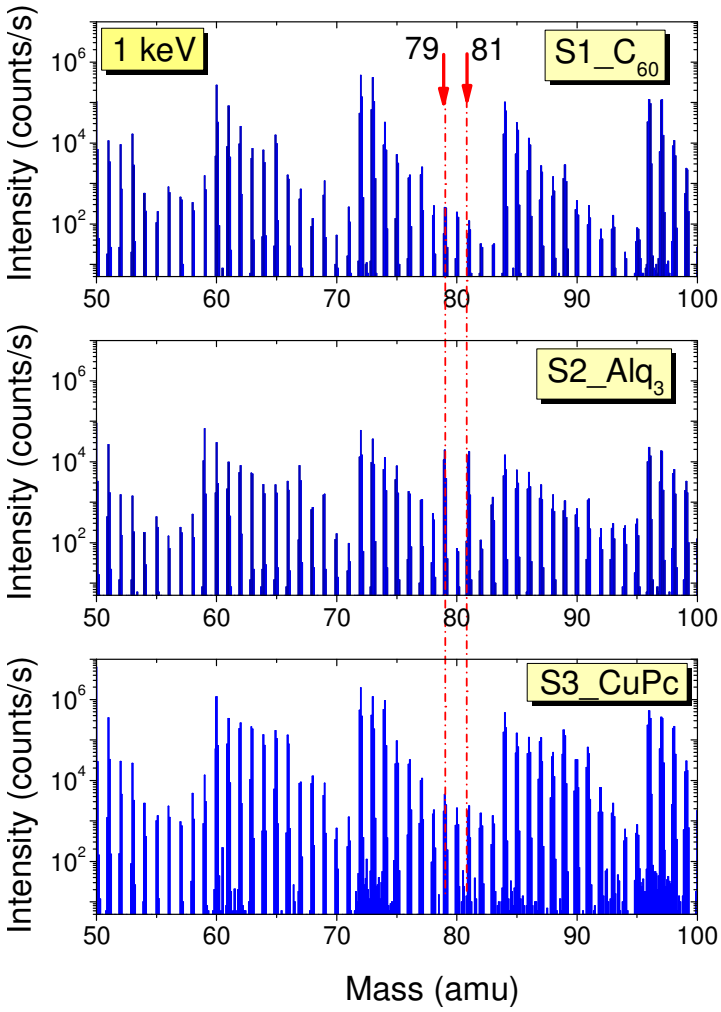

Figure III.4: *Mass spectra of S1_C_{60}, S2_Alq_3, S3_CuPc at an impact energy of 1 keV (mass range of 50-100 amu).*

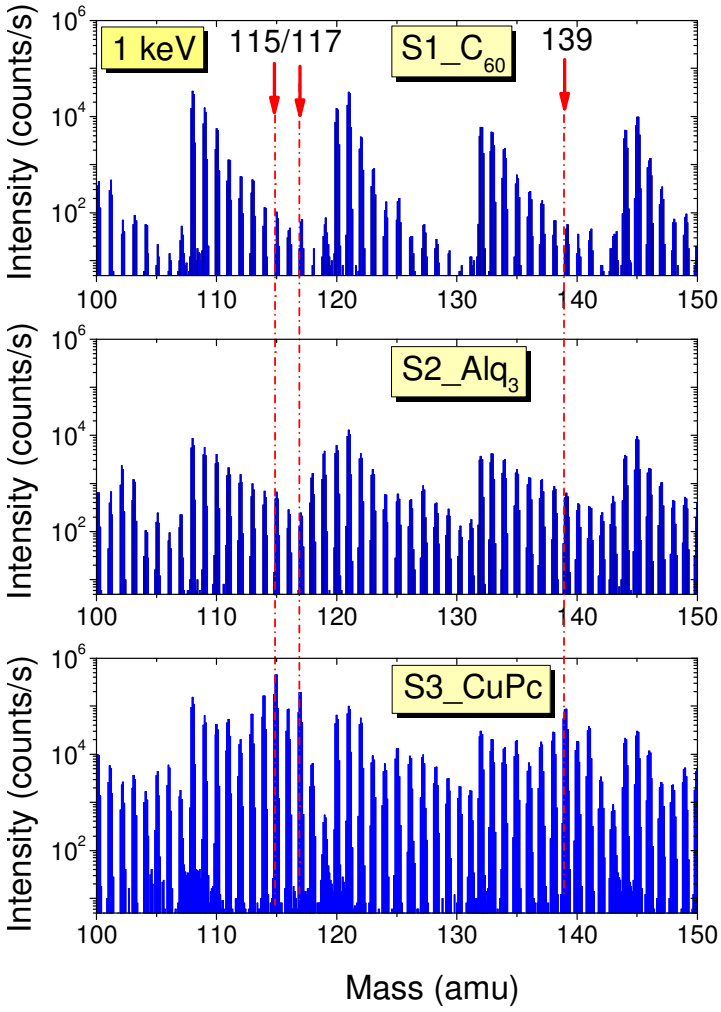

Figure III.5: *Mass spectra of S1_C_{60}, S2_Alq_3, S3_CuPc at an impact energy of 1 keV (mass range of 100-150 amu).*

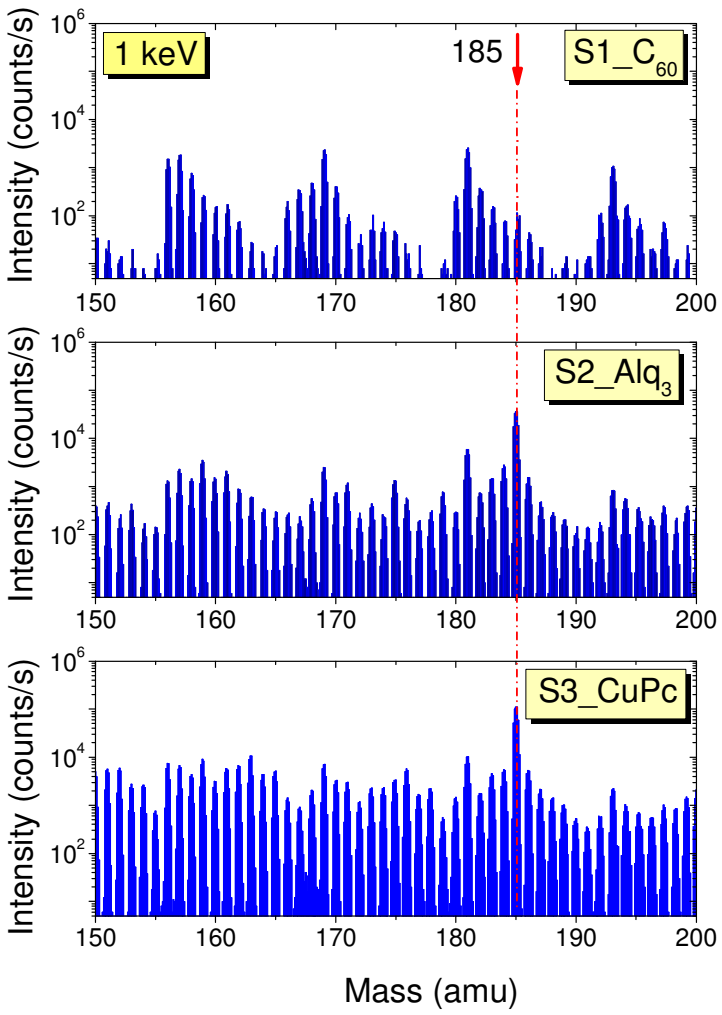

Figure III.6: *Mass spectra of S1_C_{60}, S2_Alq_3, S3_CuPc at an impact energy of 1 keV (mass range of 150-200 amu).*

III.3. Carbon clusters

As shown in the previous section, characteristic fragments of the different molecules can be identified. However, the information of molecular structure seems to be lost to a large extent. In this section, we investigate the fragmentation by locking at the abundance distributions of C_n^- and C_kCs^- clusters sputtered from the different organic molecules at different impact energies. The results from this study are compared to the results found in literature at higher impact energy (>5 keV) on different types of carbon containing materials, i.e. graphite, fullerite and SiC. This will reveal possible differences

between the emission at low impact energies in this study and at high impact energies in literature as well as between the small organic molecular thin films used in this work and the other materials in literature.

For all graphs, cluster intensities are normalized with respect to cluster size n=6 because this normalization results in the best overlay of the cluster size distributions.

III.3.1. C_n^-

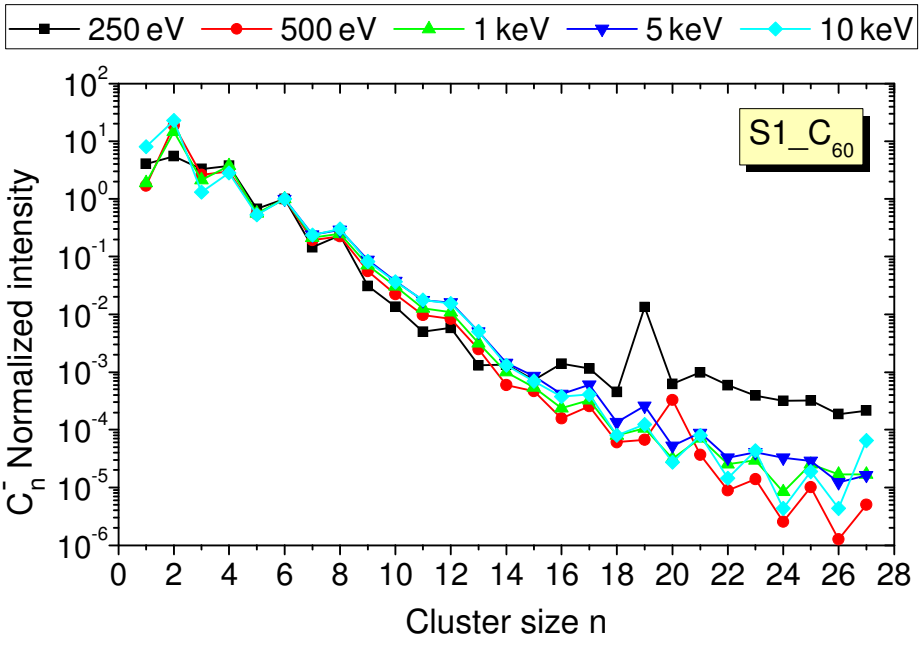

Figure III.7: *Abundance distribution of C_n^- clusters as a function of the cluster size n for different impact energies, sputtered from S1_C_{60} (normalized with respect to C_6^- intensities).*

Figure III.7 shows the secondary ion intensities of the singly-charged C_n^- clusters sputtered from C_{60} as a function of the cluster size for different impact energies. For the studied impact energies, the abundance distributions of the C_n^- clusters are similar. For the small clusters, an oscillation of the cluster abundances is observed, with the even-numbered clusters being more abundant than the odd-numbered clusters. Around n=9, a change in the periodicity occurs: the odd-even oscillations become less pronounced and

above n=16 the odd-numbered clusters dominate. This behaviour agrees with previous studies[103,136,143] (section II.1.2). According to these results, the distribution of C_n^- cluster ions of the C_{60} sample in the range from 250 eV to 10 keV can be attributed to the change in the cluster geometry, which reflects the variation of the electron affinity.

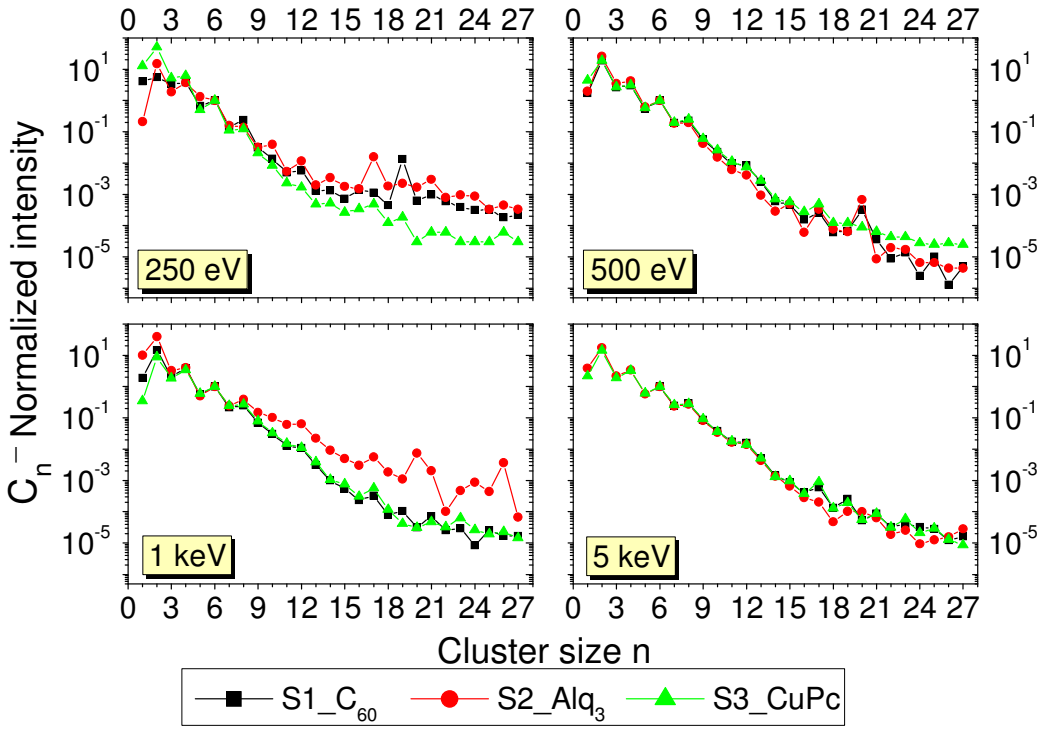

Figure III.8: *Abundance distribution of C_n^- clusters as a function of the cluster size n for different impact energies, sputtered from S1_C_{60}, S2_Alq_3 and S3_CuPc (normalized with respect to C_6^- intensities).*

Results of the C_n^- abundance distributions of Alq_3 and CuPc have been compared to C_{60} for each impact energy (Figure III.8). For the studied materials and impact energies, the abundance distributions of C_n^- clusters are unchanged and similar to the results from graphite[103,136] and silicon carbide[143]. Thus, the difference in structure and properties between our three molecules and graphite or silicon carbide does not play a significant role in the sputter-formation of the C_n^- clusters. In every situation, the initial structure of the target gets destroyed and graphitization occurs. The abundance distribution of other clusters sputtered from these three molecules will be presented next.

III.3.2. HC_n^- and C_kCs^-

Figure III.9 presents the abundance distributions of clusters at m/z=(1+12·n) amu for the different materials as a function of cluster size n and impact energy. The clusters should correspond to the mass of the HC_n^- clusters, but suffer from mass interferences in some situations. The intensities of $^{13}C^{12}C_{n-1}^-$ clusters are much smaller than those of the $H^{12}C_n^-$ clusters, so that they can be neglected. For n=1 to 11, the oscillation of the HC_n^- cluster intensities is similar to the C_n^- clusters. The clusters with even n have more important intensities than those with odd n. For n≥11, the intensity at m/z=(1+12·n) is a mixture of C_kCs^- and HC_n^- ion clusters. This point will be discussed more in detail later on. First, we will focus on the general behaviour of the distributions.

At all impact energies, the overall trend of the oscillations in the abundance distributions is the same for the three molecules (Figure III.9). However, for Alq_3 the abundance distribution differs for some cluster sizes when compared to C_{60} and CuPc, especially at the impact energies of 1 keV and 5 keV (Figure III.9). At 1 keV, the cluster intensities of Alq_3 are significantly higher for n>9, while some discontinuity in the oscillations is observed for n=17 at 5 keV. Furthermore, at 500 eV the cluster intensities of Alq_3 and CuPc start decreasing for n>20. At 250 eV, secondary cluster intensities of the different molecules start to differ for n>10. At 250 eV and 5 keV, the differences between the molecules are observed in the region of transition from predominantly HC_n^- emission to mainly C_kCs^- cluster emission. So, target composition may have an influence. The other differences cannot be explained with certainty. Nevertheless an experimental incertitude is possible. For instance, charge compensation is used for the CuPc and Alq_3 samples and varying conductivity for a decreased remaining layer thickness during the sputtering may have influenced the distributions.

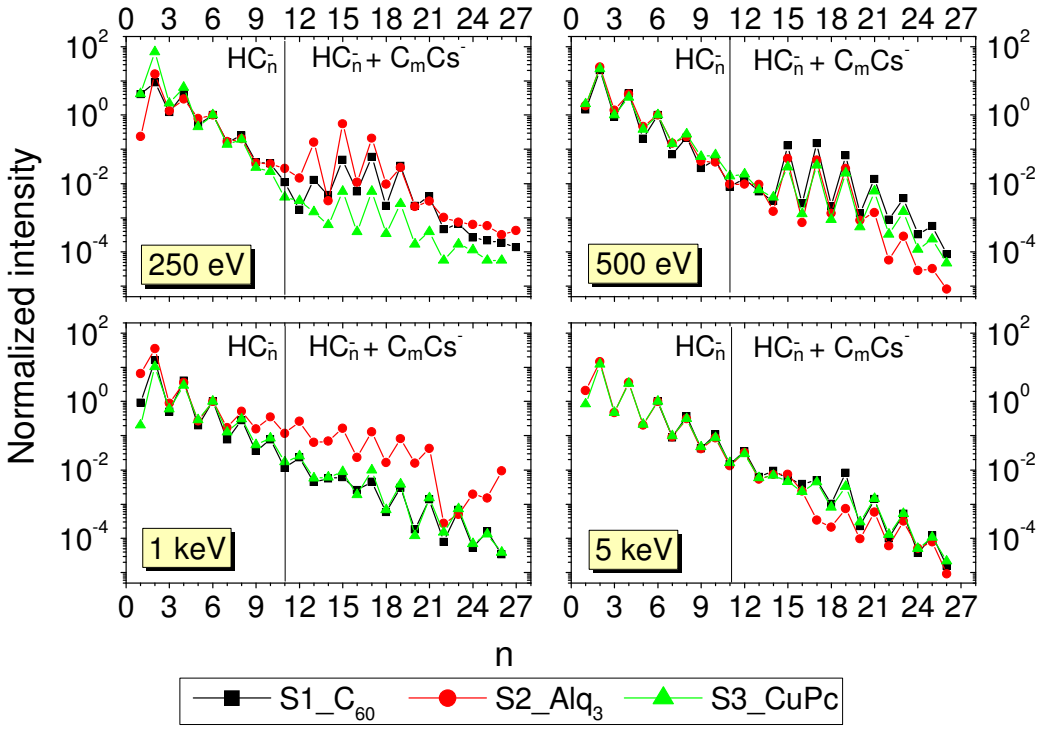

Figure III.9: *Abundance distributions of clusters at m/z=(1+12·n) amu as a function of the cluster size n for different impact energies and sputtered from S1_C$_{60}$, S2_Alq$_3$ and S3_CuPc (normalized with respect to HC$_6^-$ intensities).*

C_kCs^- clusters produce major mass interferences in the distributions. For our analysis conditions, the mass resolution of 400 is not enough to separate the two peaks at M_{Cs} = 132.9054 and M_{HC11} = 133.12663 as well as any peaks at m/z=(133+12·m). We carried out therefore some experiments at higher mass resolution (3000 instead of 400) at 500 eV which confirmed that the C_kCs^- intensities are present and are even dominant for some masses compared to the HC_n^- clusters (Figure III.10). At 500 eV, HC_{12}^- and HC_{14}^- intensities are particularly high compared to CCs^- and C_3Cs^-. For higher masses, the C_kCs^- intensities are dominating the m/z=(1+12·n) peaks (more than one order of magnitude higher). This behaviour depends however on the impact energies (Figure III.9).

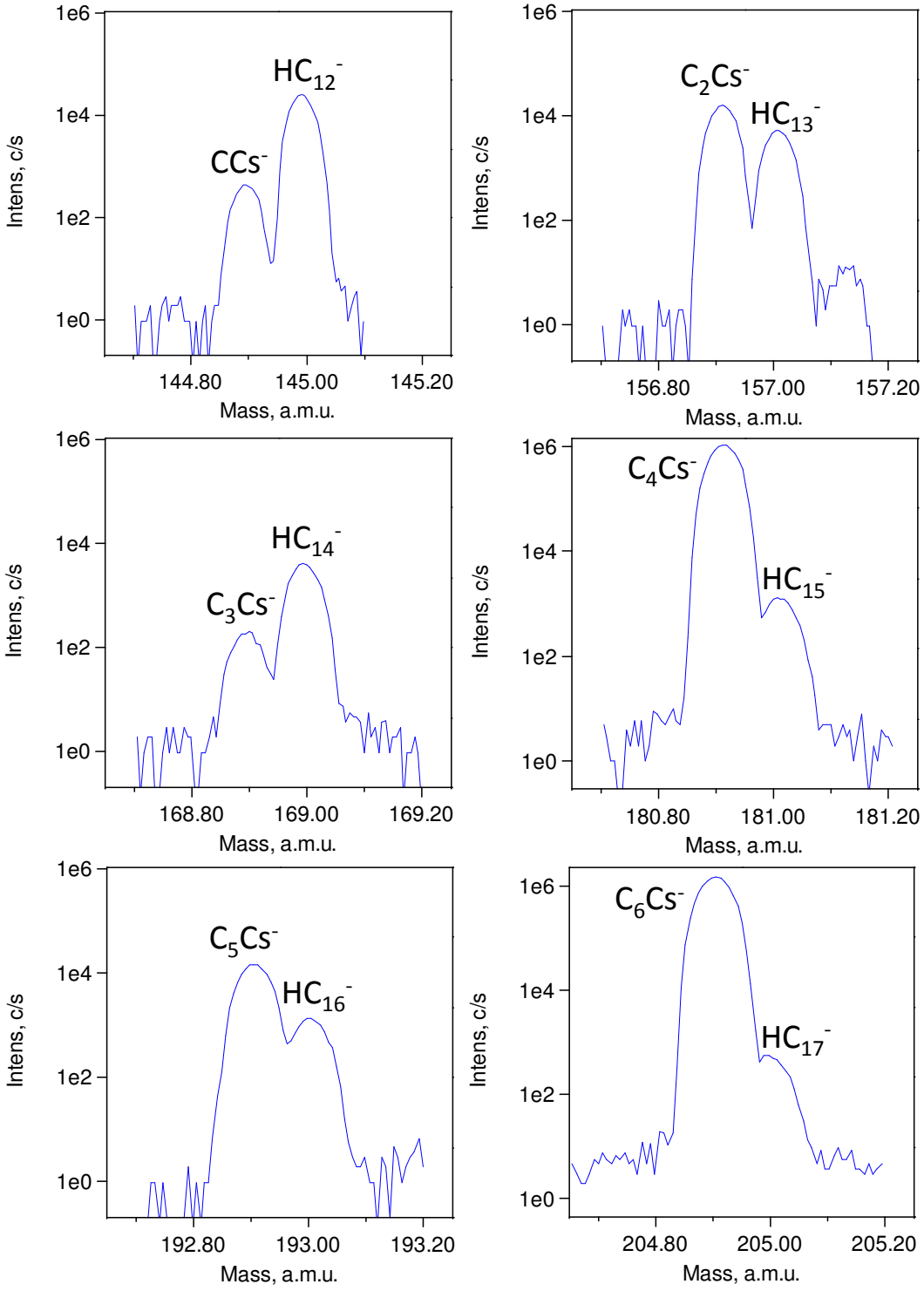

Figure III.10: *Abundance contributions of HC_n^- and C_kCs^- clusters at m/z={1+12·n) amu as a function of the cluster size n=12-17 sputtered from S1_C_{60} at 500 eV with a mass resolution of 3000.*

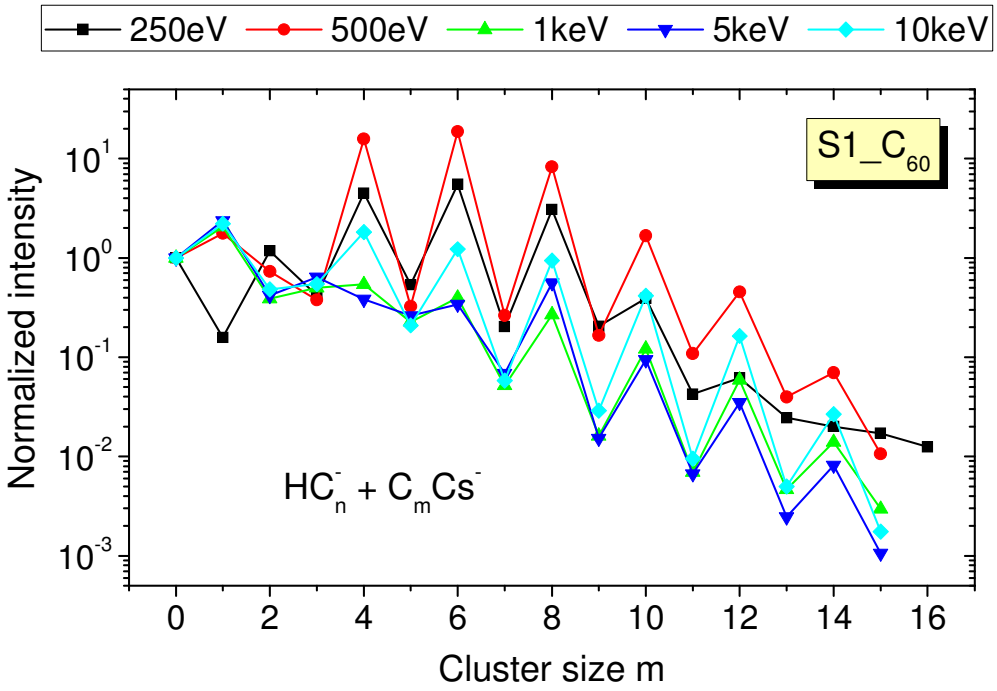

Figure III.11: *Abundance of clusters at m/z=(133+12·k) as a function of the cluster size n for different impact energies, sputtered from S1_C_{60} (normalized with respect to Cs intensities).*

For C_{60}, a more detailed comparison is given in Figure III.11. It shows the influence of the impact energy on the distribution of clusters at m/z=(133+12·k) which have the same mass than clusters at m/z=(1+12·n) with n≥11. For 250 eV, even-odd oscillations observed from k=1 to k=13 are similar to the C_n^- alternations, but much more pronounced. The behaviour of the first three clusters changes for the 500 eV impact energy: the oscillations start only at k=3 and continue until k=15, which is the highest mass that can be observed in our mass spectrometer. For the higher impact energies (1 keV and 5 keV), the oscillations are less pronounced than for the low-energy bombardment. Furthermore, the oscillatory behaviour is observed only for k>2 and k>5, respectively. For 10 keV, m must be larger than 2. The distributions observed here are a mixture of C_kCs^- clusters and mass interferences with HC_n^- clusters. The latter are assumed of having a similar abundance distribution than the C_n^- clusters. Then, the even-numbered HC_n^- clusters dominate below n=11 and the odd-numbered cluster above n=16. Thus, above the mass of 193 amu (n=16 for HC_n^- clusters and k=5 for C_kCs^- clusters), the odd-even

oscillations of HC_n^- clusters coincide with and enhance the distribution of C_kCs^- clusters. However, the oscillations of the C_kCs^- clusters with k≤5 are disturbed more or less by the HC_n^- clusters, with n changing from 11 to 16. The HC_n^- clusters have only quite a small influence on the C_kCs^- distribution at 250 eV. For higher energies these clusters disturb more. The distribution at 250 eV is similar to the results of Gnaser at 14.5 keV[103,136] (section II.1.2.iv). Differences between Gnaser's results and ours at high impact energies could be related to the different impact energies and angles which control the Cs surface concentration. Gnaser's results were obtained on a Cameca IMS 4f instrument with the primary column at 30°. On the Cameca Sc-Ultra instrument, the incidence angle is close to 38° at 250 eV. At this energy, the distribution is still similar to the results of Gnaser. The distributions start to differ from his results for the impact energies of 500 eV (incidence angle of 47°), 1 keV (angle of 51°) as well as 5 keV and 10 keV (angle of 56 °). Thus, the difference between the different impact energies and angles might be caused by changing sputtering yield Y (section II.1.2.ii), , which relates to the stationary Cs concentration c_{Cs} by the formula[224]:

$$c_{Cs} = \frac{1}{1+Y} \qquad \text{(III.1)}$$

For C_kCs^- clusters, formation mechanisms are far less studied than for MCs^+ clusters (with M being any element), but the influence of the Cs surface concentration can be supposed to be similar[225-227]. For too low Cs concentrations (high impact energies) the probability to form a cluster could be low because of the lack of Cs atoms. Changing Cs surface concentrations influence probably the ionization mechanisms, but this is difficult to study in this kind of materials.

III.4. Carbon-Nitrogen clusters

The carbon-nitrogen cluster ions have not been studied in detail up to now. The only study found is about the emission and formation of C_nN^- clusters by Gupta et al.. In addition, in his study the maximum cluster size is limited to n=10. In this study, the presence of the $C_nN_x^-$ (x=1-3) clusters is found for the Alq_3 and

CuPc samples, both of which contain nitrogen in the molecule. However, the aforementioned distributions are influenced by mass interferences from H-containing clusters like $H_yC_n^-$ (y=2-6) due to low mass resolution. Therefore, the $C_nN_x^-$ abundance distributions will not be discussed in detail. The problem of mass interferences will be explained and the suitability of the CN^- cluster as characteristic fragment for the CuPc and Alq_3 molecules will be proven.

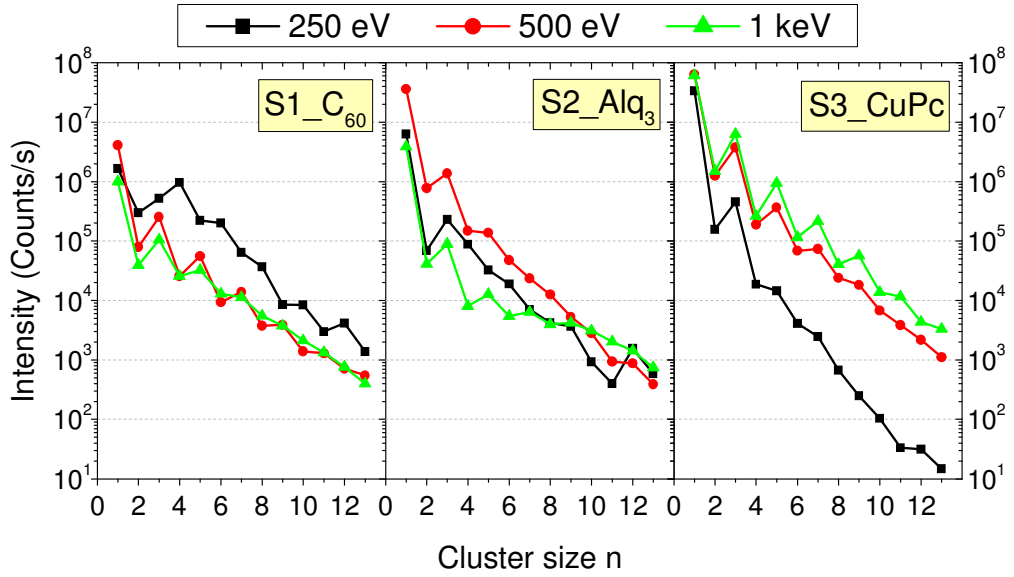

Figure III.12: *Abundance distribution of clusters at m/z=(14+12·n) as a function of the cluster size n for different impact energies.*

Among the three molecules studied, the C_{60} molecule contains only C, thus the presence of peaks at m/z=(14+12·n), which corresponds to the mass of C_nN^- clusters, is due to $H_2C_n^-$ clusters. The distribution of $H_2C_n^-$ clusters in the C_{60} sample (Figure III.12) is similar to the one of HC_n^- clusters: for impact energies from 500 eV to 1 keV, the oscillations with the even number of C atoms in the clusters are dominant. The total intensity reduces when n varies from 2 to 12. The distribution is limited to n=13 because of the strong mass interferences with the Cs containing cluster at higher masses. For the impact energy at 250 eV, the oscillations with predominantly odd-numbered peaks starting from n=5 for the $H_2C_n^-$ clusters could not be explain.

The general trend of the abundance distributions of the clusters at m/z=(14+12·n) in CuPc at 500 eV and at 1 keV and in Alq_3 at 500 eV is similar to the abundance distribution of the $H_2C_n^-$ clusters in C_{60} (Figure III.12).

The presence of both C_nN^- and $H_2C_{n+1}^-$ cluster ions at the mass of (14+12·n) amu is also verified for CuPc by ToF-SIMS. In addition, the intensities for CuPc and Alq_3 in Figure III.12 are several times higher than the intensity of $H_2C_n^-$ ions for C_{60}. For the C_nN^- clusters from the CuPc sample, the even – odd oscillations with a maximum for the odd-numbered C atom clusters take place until n=11. This behaviour agrees with the results shown by Gupta et al.[138]. The change in the distributions for CuPc at 250 eV and for Alq_3 at 250 eV and at 1 keV could not be explained in this study. It seems like the secondary ion clusters are not very stable and the peak intensity at the high masses become more sensitive to the analysis conditions.

Comparing the raw intensities at mass of m/z=26 amu for all three impact energies and all three molecules, the intensities from the C_{60} sample are the lowest for each impact energy, with the intensities from the Alq_3 sample being a few times higher and the intensities from CuPc being highest with more than one order of magnitude higher than the one from C_{60}. The intensities of the C_n^- cluster ions in the different samples are however similar. The difference in intensity at m/z=26 is explained by the nitrogen concentration in these molecules: C_{60} contains no nitrogen, Alq_3 5.8 atomic % of nitrogen and CuPc 14 atomic % of nitrogen. Due to the different nitrogen concentrations in the molecules, the contribution of the CN^- ions to the mass of m/z=26 amu is less in the Alq_3 molecule than in the CuPc molecule. Therefore, the secondary ions at m/z=26 can be used to identify the three molecules with high secondary ion intensity (>10^8 counts/s). Furthermore, this cluster presents much higher intensities than any other typical cluster, e.g. $MC_2N_2^-$ and $MC_2N_2H_2^-$ where M is the metallic element in molecule (<10^6 counts/s). CN^- ions allow depth profiling of the organic layers with much higher sensitivity.

III.5. Conclusions

In this chapter, the objective is to identify typical secondary ions for the different organic molecules and to study the effect of low energy Cs^+ bombardment on the fragmentation. To reach these goals, the cluster

formation was investigated for organic molecules (C_{60}, CuPc and Alq_3) under various impact energies from 10 keV down to 250 eV.

At first, despite the low impact energies, the molecular structure is largely lost in the steady-state conditions due to the fragmentation of the organic chains. However, some characteristic fragments persist and the different molecules can be distinguished by secondary ion clusters containing the specific species of each molecule and producing high secondary ion intensities. They include $MC_2N_2^-$ and $MC_2N_2H_2^-$ clusters where M is the metallic element in the molecule.

Next, the distributions of C_n^-, C_kCs^- and $C_nN_x^-$ cluster emission has been explored at low impact energies and compared to bibliographic references at high impact energies on other types of C-containing samples. The distributions of the C_n^- do not depend on the impact energy, at least not in the energy range between 250 eV and 5 keV. Similarly, the distributions at $m/z=(1+12\cdot n)$ for $n<11$ are due to HC_n^- and are identical for the different impact energies and the three organic samples. For HC_n^- clusters with $n>11$, mass interferences with C_kCs^- clusters exist and become even dominant. They can only be avoided at high mass resolution. In contrast to other clusters, the distribution of the C_kCs^- cluster intensities changes with the impact energy: for impact energies at 250 eV, oscillations are observed over the whole abundance distribution. For the other impact energies, the oscillations of the cluster intensities start only at larger cluster sizes. This energy dependence of C_kCs^- distribution is probably caused by the variation of the Cs surface concentration. Furthermore, the distributions of the C_n^- and C_kCs^- (at 250 eV) cluster intensities are similar to the results published for graphite, amorphous C, fullerene and SiC by other authors, indicating that the emission and ionization mechanisms for these different kinds of materials at low impact energy in dynamic SIMS should be similar. For the $C_nN_x^-$ clusters (with $x=1,2,3$), the mass interferences with $C_nH_y^-$ are important. Nevertheless, the abundance distribution of $m/z=(14+12\cdot n)$ up to $n=13$ is similar to the results of Gupta. Furthermore, the CN^- ion allows identifying the different organic molecules used in this study. CuPc shows the highest intensity at $m/z=26$ while the C_{60} shows the lowest intensity.

For the depth profiling discussed in chapter V, the secondary ions C_n^-, CN^-, $MC_2N_2^-$ and $MC_2N_2H_2^-$ etc. could be chosen to characterize the C_{60}, CuPc and Alq_3 molecules. However, due to its high secondary ion intensity and its

capability to identify the different molecules, the more simple CN^- ions is preferred for depth profiling. This cluster does not present many mass interferences, so that the mass resolution of 400 can be used in order to keep high secondary ion intensities.

Chapter IV
Study of Cs aggregation in SIMS craters

As presented in chapter II, the desorption of Cs implanted into samples during the sputtering by Cs^+ primary ion beams has been observed for inorganic materials. Up to now, the behaviour of implanted Cs in general and its desorption in particular have not been studied for organic materials. In addition, for SIMS applications the Cs oxidation of Cs^+ bombarded surfaces under the presence of oxygen has not been studied. However, understanding the implantation and desorption of Cs on sample surfaces in vacuum as well as in air is important and necessary when the SIMS technique is combined with other techniques for complementary information on complicated samples. In such situations, the surface at crater bottoms must not been modified during sample transfer.

This chapter is about the possible impacts of Cs diffusion and oxidation on subsequent analyses for the craters formed by Cs^+ sputtering. Subsequent analyses include imaging by the NanoSIMS50 instrument for chemical composition or AFM measurements for topography information. These results are important to avoid any artefacts in the next chapter when SIMS depth profiling is combined with AFM imaging.

To reach these objectives, two organic materials are used: Alq_3 and CuPc. The elemental mapping of previously Cs-sputtered craters is compared before and after air exposure. The change in chemical composition of the crater after air contact is studied by NanoSIMS and XPS and is combined with the topographical information obtained by AFM. The results by the different techniques are studied as a function of exposure to air. Possible explanations for the phenomena are discussed. This work will help to avoid artefacts in the interpretation of surface roughness for Cs-implanted surfaces when exposed to air during sample transfer (chapter V).

IV.1. Samples and characterization

Metal/organic layered sample		Layer thickness (nm)	Deposition temperature
A1	Ag/Alq_3	30	RT
A2b	Ag/CuPc	30	RT
C1	Ag/CuPc	13	-60 °C
Single organic layer		**Layer thickness (nm)**	**Deposition temperature**
S4	Alq_3	80	RT
S5	CuPc	80	RT

Table IV.1: *List of samples and preparation conditions.*

In this study, we use three metal/organic bi-layered samples (samples A1, A2b and C1) and two single layered organic samples (samples S4 and S5). Their characteristics are listed in table IV.1. More information about the preparation conditions is given in I.4.

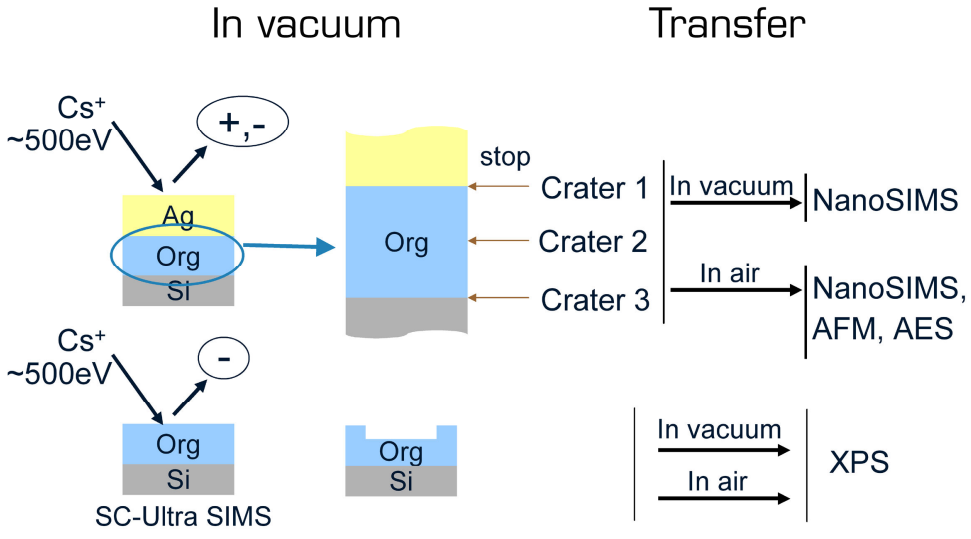

Figure IV.1: *Schematic diagrams showing experimental processes for bi-layered samples and single layered samples.*

A schematic detailing the craters prepared by SIMS is shown in Figure IV.1. Topography and elemental mapping are performed on the bi-layered samples. Complete SIMS depth profiles are recorded at first at 500 eV in the negative mode. Using the same conditions, samples are sputtered to different depths, i.e. crater 1 is stopped at the Ag – organic interface, crater 2 in the middle of the organic layer and crater 3 at the organic – Si interface. Then, after air exposure the surface roughness is measured as a function of time in air by AFM. Elemental mapping of the surface before and after air exposure is carried out in vacuum using SIMS and AES. This allows us to determine the composition of the crater bottoms. Samples S4 and S5 are bombarded by Cs^+ ions and then analyzed by XPS. These XPS spectra allow us to determine the difference in surface concentration and bonding before and after air exposure. Differences related to the two materials Alq_3 and CuPc are also explored.

IV.2. Cs oxide aggregation

The AFM measurements on sample A2b (Ag/CuPc on Si) show the variations in topography with crater depth (Figure IV.2). The images were recorded after transferring the samples in air from the SIMS instrument to the AFM instrument. The surface is smoothed during the sputtering of the 30 nm Ag layer down to the Ag/CuPc interface. After sputtering away half the CuPc layer, the surface topography develops with small and dense dots (in crater 2 at a depth of about 45 nm). Bigger and more distributed dots appear at the CuPc/Si interface (crater 3 with a depth of about 60 nm). Similar periodic features in a Cs^+-bombarded surface of silicon rich oxy-nitride films have been seen by Barozzi et al.[228]. The author explains the appearance of the features by artefacts due to sample rotation during SIMS analyses. Cs is not mentioned as an explanation. For further understanding, we characterize the Cs^+ bombarded surface under vacuum and after exposure to air (Figure IV.3).

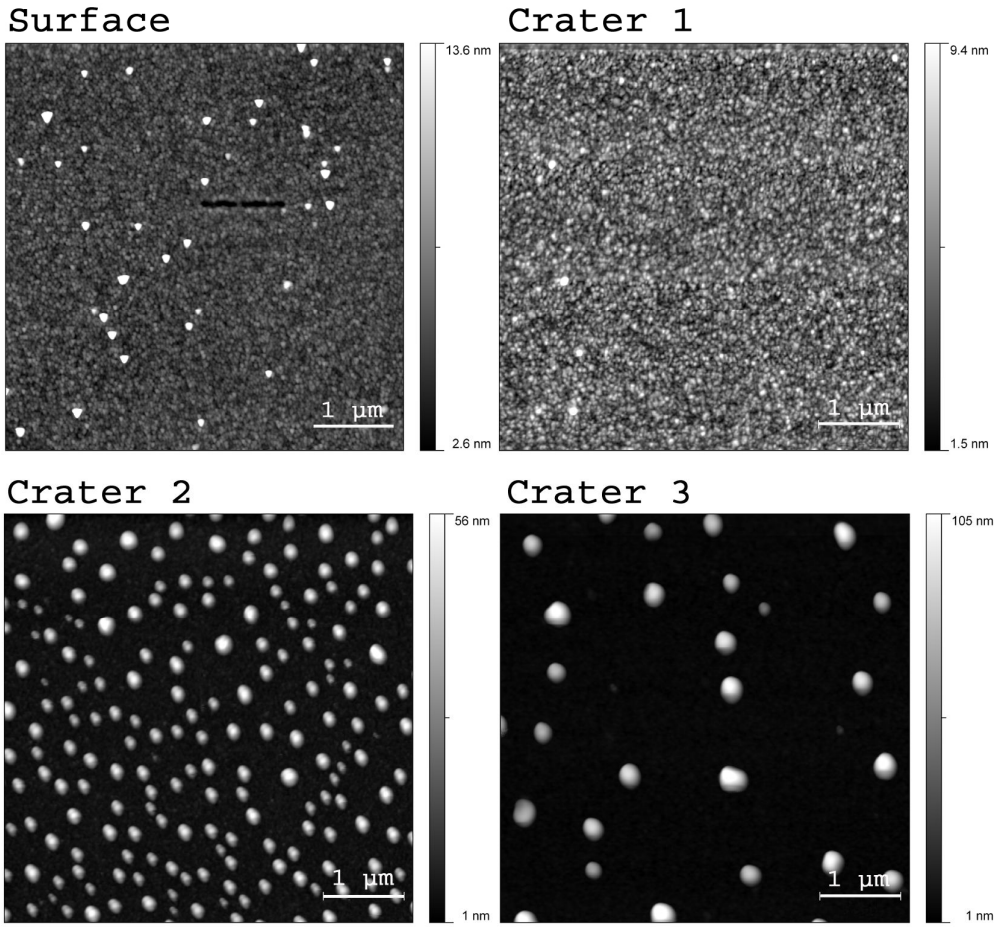

Figure IV.2: *AFM images (5 x 5 µm^2) at the bottom of craters of sample A2b, after 4 days of exposure to air: at the sample surface; at the bottom of crater 1 at a depth of 30 nm (Ag/CuPc interface); at the bottom of crater 2 at a depth of ~45 nm (middle of CuPc layer); at the bottom of crater 3 at a depth of ~60 nm (CuPc/Si interface).*

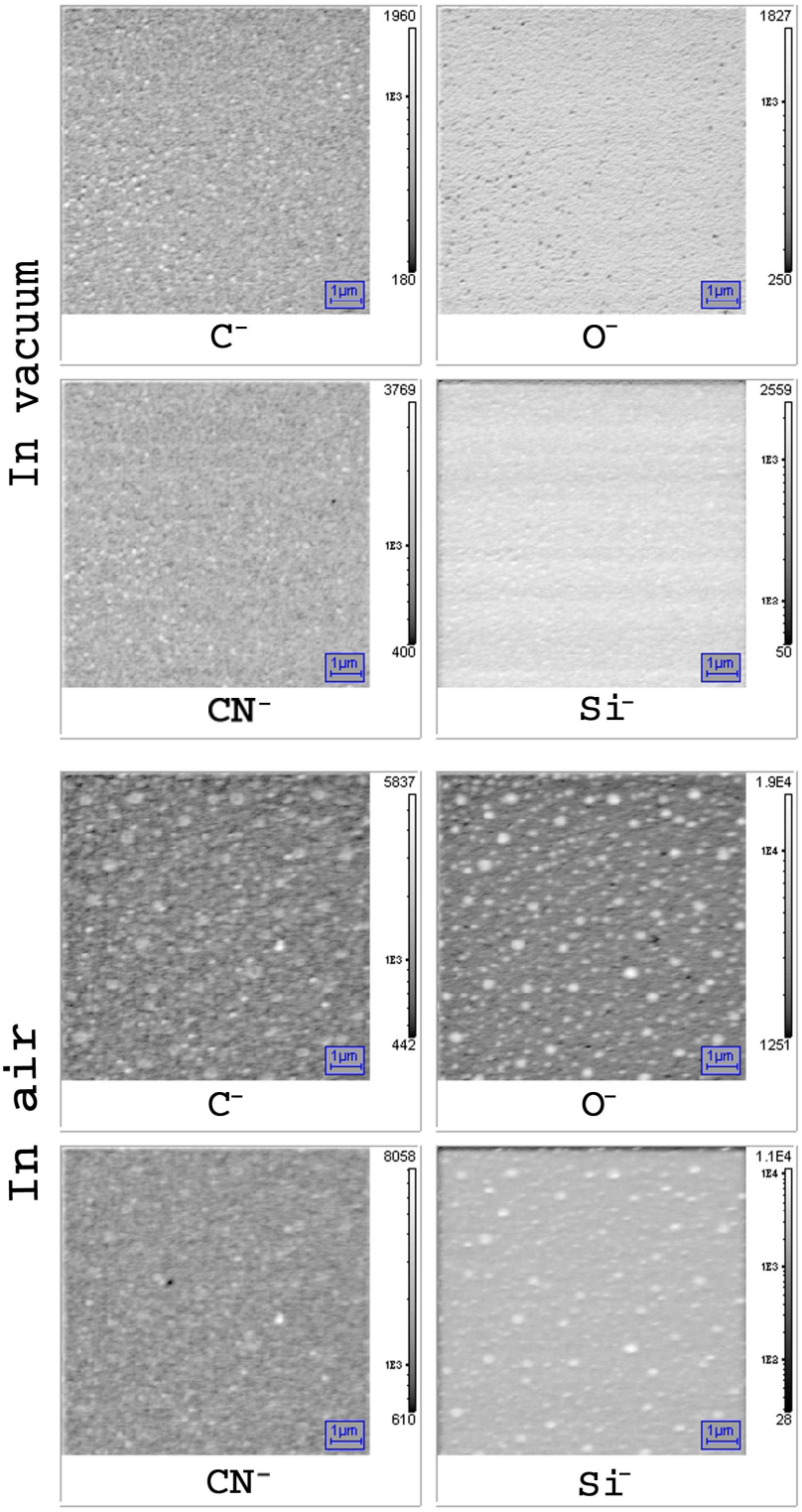

Figure IV.3: *C, O, CN and Si images (10 x 10 µm²) by NanoSIMS50 at the bottom of crater 3 of sample A2b: after 3 days in vacuum at ~10⁻⁷ mbar (top) and after 42 days exposure to air (bottom).*

The previous hillocks are proved to appear only after exposing the Cs bombarded craters to air. Elemental mapping by NanoSIMS50 shows the effect of air exposure on the Cs at the crater bottom. Figure IV.3 shows C^-, O^-, CN^- and Si^- images before and after exposing crater 3 of sample A2b to air. The direct image of Cs is not possible in this experiment as the Cs^+ primary ion beam was used to get high lateral resolution. Due to the optical design of the NanoSIMS50 instrument, the primary and secondary ions must have opposite polarities. Thus, in our experiment only the negative secondary ions can be detected. The images of the sample kept in vacuum are homogenous while those exposed to air develop a patterned surface. In the SIMS images of the sample exposed to air, the intensity of O^-, C^- and Si^- secondary ions is highest on the dots. The size of these dots agrees with the hillock size found in the AFM images. This shows that the exposure of Cs irradiated samples to air changes not only the topography but also the chemical composition of the sample surface for subsequent SIMS analyses. These artefacts may lead to a wrong interpretation of the AFM and NanoSIMS50 results, and thus prove to be of particular importance for imaging applications.

In Figure IV.4, the Cs image from the AES analysis of crater 2 of sample A2b is compared to the AFM image, which was recorded after 1 day of exposure in air. Although the AES spots are a bit bigger compared to the AFM dots, the similarity between the patterns in these two images confirms that the hillocks observed by AFM are riche in Cs. Thus, the previous conclusion from the NanoSIMS50 images that a chemical change accompanies the topographic evolution is confirmed. For more precise information, the AES elemental analysis was recorded in some spots and outside the spots. The areas are selected from a SEM image (Figure IV.5). The crater 3 was chosen for the selection of the analysis points (inside and outside the dots) because the dots are less dense than in crater 2. The results show a higher amount of Cs and O and a lower C and N content in the hillocks than outside these hillocks (table IV.2). In addition, the Cu concentration is quite small in the particles as well as outside them. Therefore, the hillocks seen by AFM are composed of Cs and Cs oxide(s).

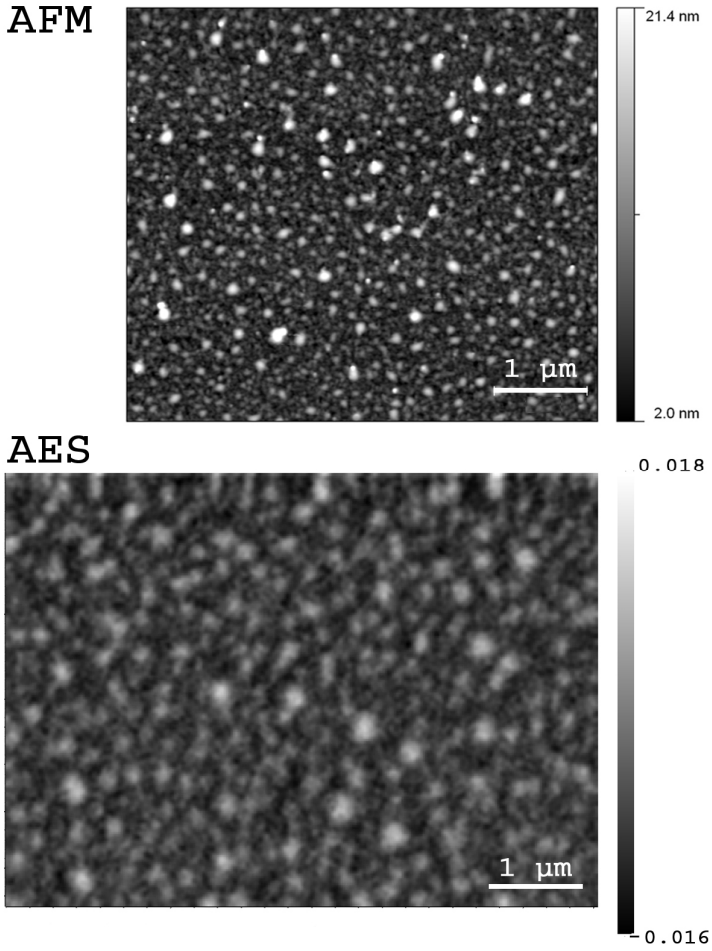

Figure IV.4: *Crater 2 (stopped at a depth of about 45 nm) of sample A2b: AFM image (5 x 5 µm^2) after air exposure (top image) and Cs image from AES (6.25 x 4.6 µm^2) recorded after 1 day in air (bottom image).*

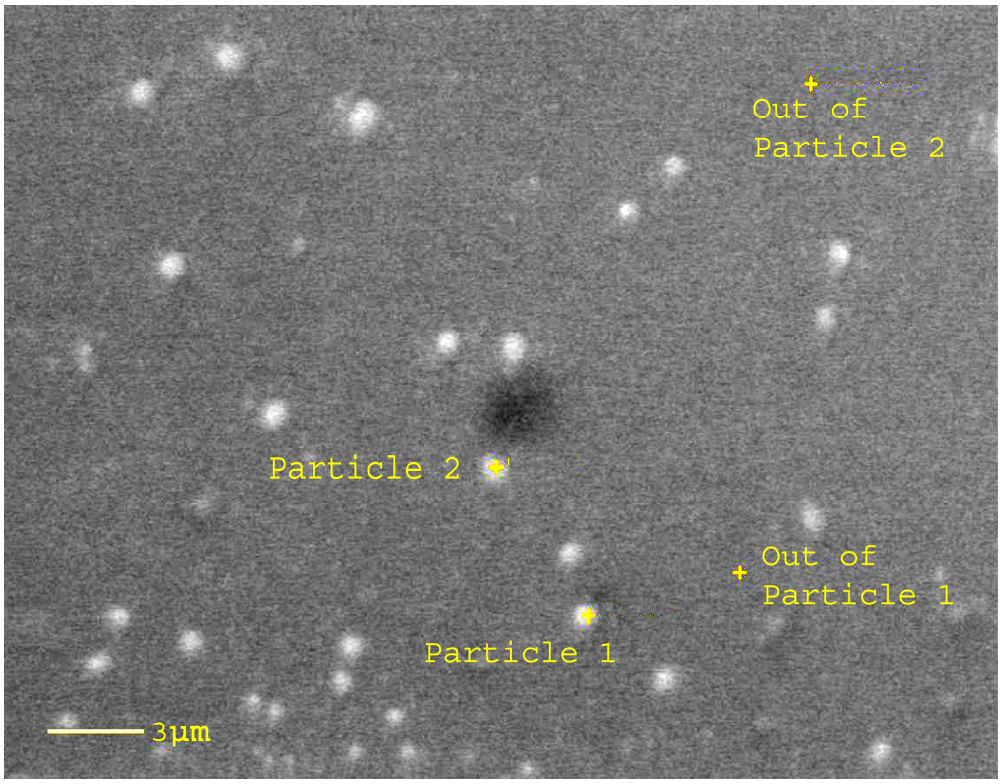

Figure IV.5: *SEM image (30.9 x 22.6 µm²) of crater 3 (stopped at a depth of about 60 nm) of sample A2b, after 1 day exposed to air.*

Atomic relative composition (at%)	Cs	O	C	N	Cu
Particle 1	39.0	9.3	44.8	5.4	1.5
Particle 2	42.2	13.8	39.2	3.4	1.4
Out of Particle 1	23.0	7.0	57.7	9.9	2.4
Out of Particle 2	21.0	7.0	60.5	10.5	1.0

Table IV.2: *Relative atomic composition calculated from AES at different points in crater 3 of sample A2b (Figure IV.5). The analysis was recorded after 1 day exposure to air.*

Using the oxidation mechanism proposed by Woratschek[123] (in chapter II), the hillocks seen in AFM and NanoSIMS50 in our SIMS craters can be explained as

follows. During the bombardment, Cs is implanted into the sample. After exposure to air, Cs on the outermost surface reacts with O_2 to form $Cs_{11}O_3$, Cs_2O_2 and then CsO_2. As long as the amount of Cs implanted near the surface is high enough and Cs diffuses to the surface, the ceasium oxide islands are formed (Craters 2 and 3 in Figure IV.2). Under the high oxygen pressure in air, the transformation of Cs_2O_2 to CsO_2 and the formation of the CsO_2 topmost layer are expected instantaneously after exposing the Cs-bombarded surface to air (cf. II.1.2.iii.b). This layer acts as passivation layer that retards further oxygen penetration and its reaction with underneath Cs. Thus the Cs-O hillocks consist of several oxide forms. The atomic ratio Cs to O is of 3.7, 2.0, 1.0, 0.5 in the different $Cs_{11}O_3$, Cs_2O, Cs_2O_2 and CsO_2 oxides, respectively. The Cs to O ratio outside the dots of 3.1 compares to the values of about 3.6 in the particles (Table IV.2). This means inside the dots exists more Cs in lower oxidation states than outside. Moreover, the atomic concentration of C and N in the particles is less than outside. The AES calculation gives the relative atomic concentration. Thus, when more Cs and O are present the calculated C and N concentrations decrease. In SIMS elemental images (Figure IV.3), however, the C^- intensity is higher inside than outside the dots. This is known as matrix effect in SIMS, which is explained by the increase of the secondary ion ionization probability due to the low electron work function of Cs and its oxides[123].

From crater 2 to crater 3, the bombarded surface changes from the middle of the CuPc layer (15 nm from the Si substrate) to the CuPc/Si interface. The change of the bombarded surface leads to a different sputtering yield Y, which relates to the stationary Cs concentration c_{Cs} by the formula III.1[224]. Therefore, the two depths of the craters 2 and 3 correspond to a different Cs implantation, which creates the different hillock development on these craters (larger and more distributed hillocks in crater 3 than in crater 2). Detailed explanations and more XPS and AFM evidence are shown and discussed next.

IV.3. Topography variation as a function of time

Further investigation on the topography of craters 1 to 3 in sample A2b was carried out using AFM. The roughness is characterized using the root mean square (RMS) roughness calculated from the AFM images. Two roughness values are defined: roughness with the Cs-O hillocks calculated from the original AFM images and roughness without the Cs-O hillocks calculated from the AFM images where the hillocks are removed by a mask (Figure IV.6). To define the mask, the Cs-O grains were marked by the thresholding algorithms using the Gwyddion software[229]. The grain statistics function allows calculating the total number of marked grains, the mean equivalent square size of grains as well as the total grain volume.

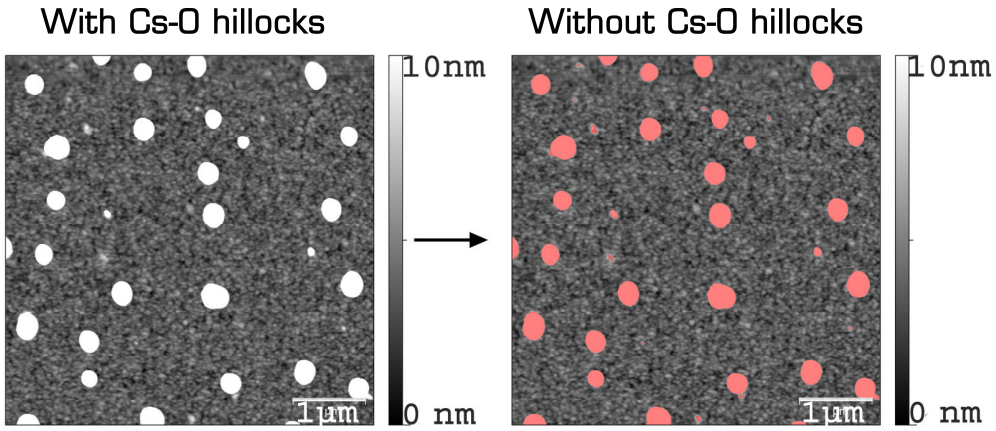

Figure IV.6: *Example showing the AFM images for calculating the roughness. The original image (left) is used to obtain the roughness by considering Cs-O hillocks, the Cs-O dots masked image (right) is for the roughness calculation without considering the Cs-O hillocks.*

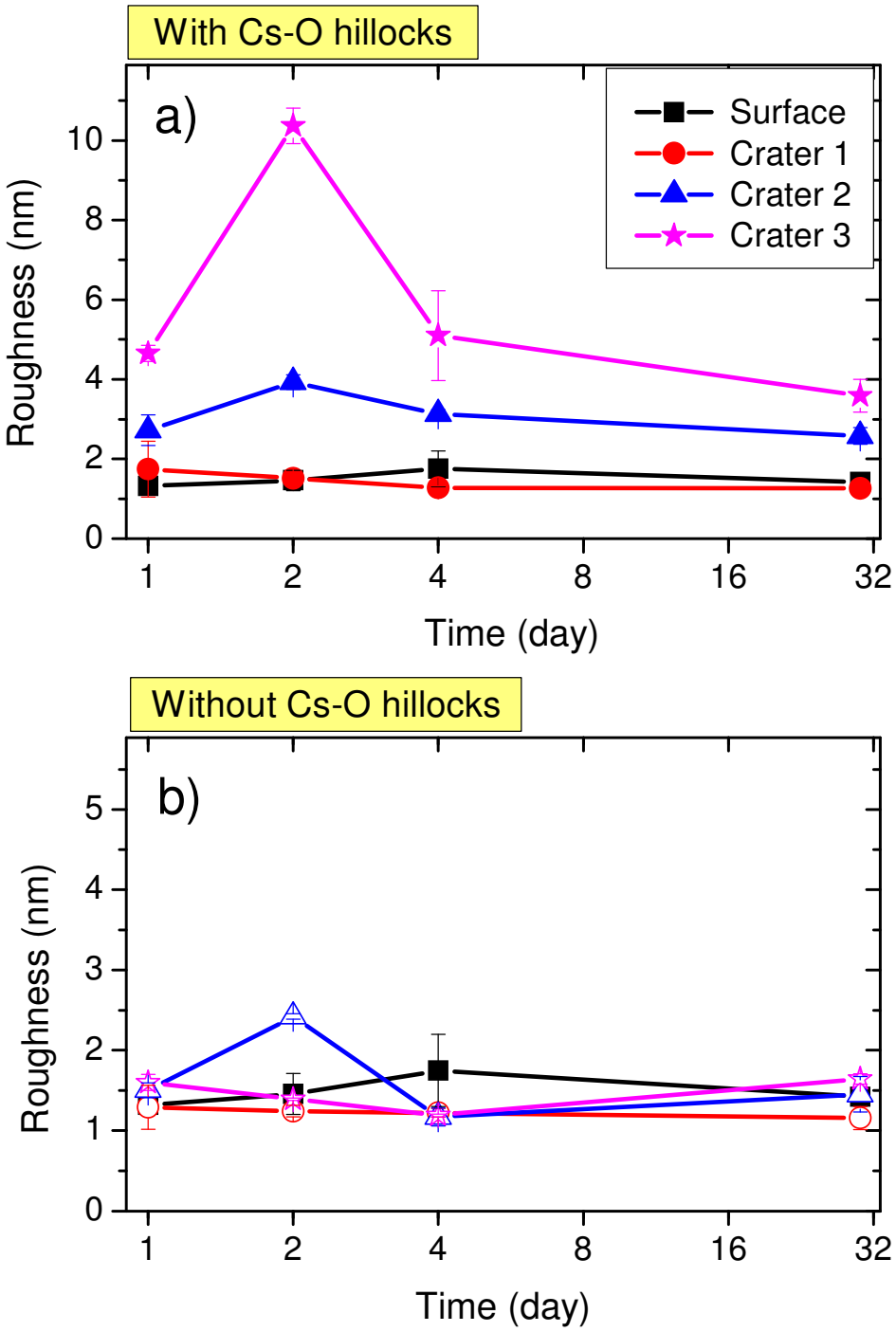

Figure IV.7: *Development of crater roughness, including Cs-O hillocks (a) and without Cs-O hillocks (b) as a function of the time exposed to air for sample A2. The time scale is in log_2 of days.*

Figure IV.7 shows the roughness variation calculated (a) with and (b) without Cs-O hillocks as a function of time where the sample is exposed to air. The

roughness of the sample surface outside the craters does not change much with time (<0.4 nm). Thus it proves that the AFM instrument was calibrated correctly on the different analysis days and that the AFM measurements on different days can be compared to one another. Similar to the surface, there is no remarkable change in crater 1 (at the Ag/CuPc interface at a depth of 30 nm) after 30 days exposure to air. Interestingly, a strong variation in roughness as a function of time in air has been seen in the deeper craters (crater 2 and crater 3). For these two craters, after two days of exposure to air, the roughness increases and reaches more than 10 nm for crater 3 and about 4 nm for crater 2. The measurements repeated after 4 and 32 days in air show a strong decrease of the roughness in the period between the 2nd and 4th day at air. Between the 4th and 32nd day, the roughness decreases slowly to a constant value. The roughness variation in crater 3 is more important than in crater 2.

For the roughness excluding Cs-O hillocks, no remarkable variation is seen (Figure IV.7.b). The roughness of sample surface and at the bottom of craters 1 and 3 in all the first 32 days is constant and has values less than 2 nm. The roughness at the bottom of crater 2 shows a little variation at the 2nd day (from 1.5 nm to 2.5 nm). This is attributed to a calculation uncertainty due to small, dense and overlapping Cs-O dots (Figure IV.9, 2nd day, crater 2) which hinders the effective masking. Thus, the hillocks which cannot be masked increase the roughness in crater 2 at the 2nd day. In summary, except the limitation to the small Cs-O hillocks, the roughness in the craters stays unchanged as a function of the duration of exposure to air.

Figure IV.8 presents the development of the mean grain size and the total grain volume as a function of days in air for sample A2b. Similar to the surface roughness, the change of Cs-O mean grain size and total grain volume as a function of time of air exposure in craters 2 and 3 shows the same trend as the RMS roughness calculated including the Cs-O hillocks. Moreover, the grains in crater 3 are about 30 nm larger than the ones in crater 2 (first and second day of exposure to air). In addition, the total grain volume in crater 3 increases much more than the total grain volume in crater 2 (second day at air). However, after two days, both the grain size and the total grain volume of crater 3 shrink to the values of crater 2. The difference between crater 2 and

crater 3 will be explained latter. The variation as a function of air exposure is caused by the building up and disappearance of Cs-O hillocks and is discussed using Figure IV.9.

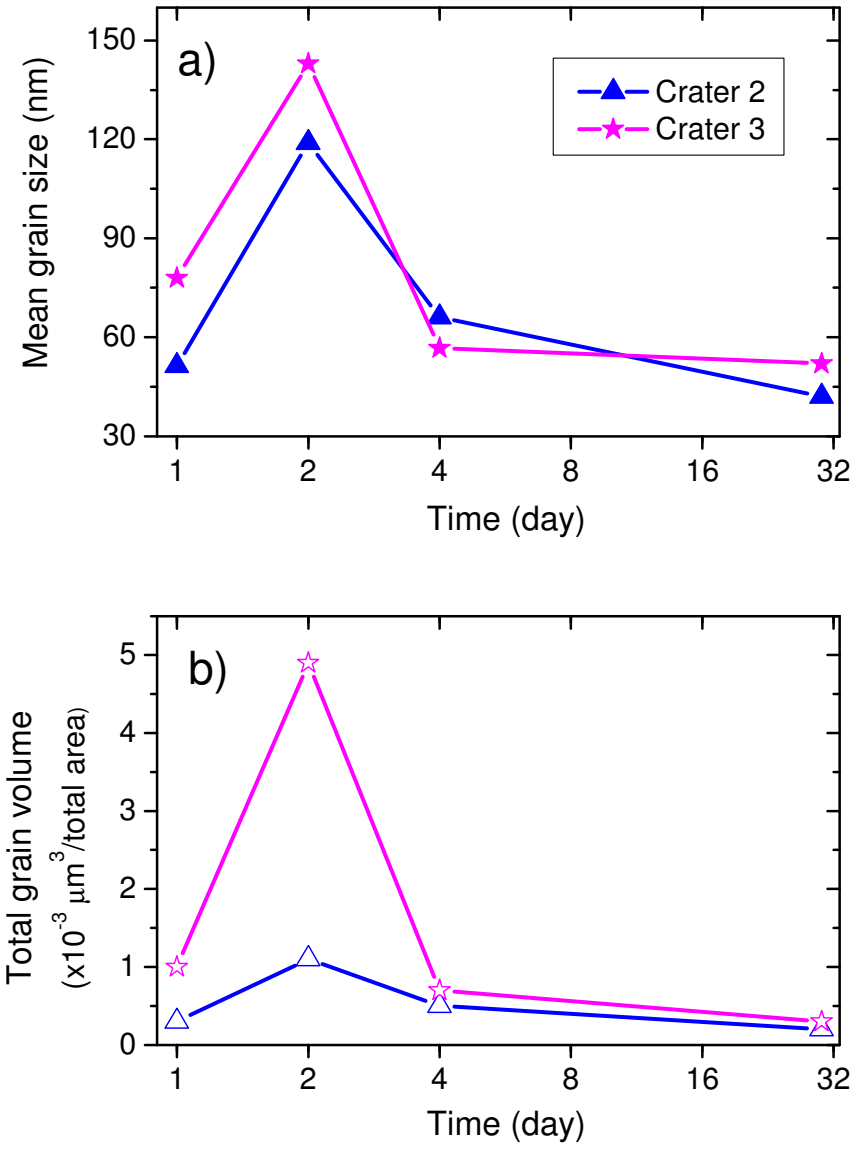

Figure IV.8: *Development of mean grain size (a) and of total grain volume (b) as a function of days in air for sample A2b. The time scale is log_2 of days.*

As described in chapter II, the desorption of Cs implanted into inorganic substrates during Cs low-energy bombardment in dynamic SIMS[118,119,230] has been proven. Otherwise, in organic materials, the migration of implanted Cs

from inner-layers towards the surface is observed only when exposing the sample surface to O_2[124].

Similarly, in our vacuum conditions Cs atoms can migrate during sputtering to the sample surface and desorb. However, the residual O_2 pressure in the analysis chamber is not high enough to produce the Cs-O hillocks. Thus, SIMS imaging of craters kept in vacuum produces homogeneous images (Figure IV.3). After exposure to air, feeling the oxygen driving force, the implanted Cs diffuses towards the surface and reacts with O_2 to form successively $C_{11}O_3$, Cs_2O_2 and CsO_2. The absorption of O_2 on $C_{11}O_3$ creates rich oxygen zones, which are nuclei for Cs_2O_2 and the hillocks (Figure IV.9, 1st day at air). The migration of Cs atoms from underneath layers towards the rich oxygen spots on the sample surface leads to the growth of Cs-O dots (Figure IV.9, 2nd day at air). As a result, the roughness and the hillock volume increase strongly during the 2 first days in air (Figure IV.7, IV.8). After the 2nd day, the Cs migration slows down or stops, and the hillocks are oxidized gradually to CsO_2. This oxidation leads to the decrease of the hillock size between the 4th and 32nd day at air (Figure IV.9, the 4th and 32nd day at air). Contrary to the growth, Cs-O islands disappear slowly, and some remain even after more than 30 days. The incomplete transformation from Cs_2O_2 to CsO_2 is observed by other authors[123,124]. It can be explained by the slow O_2 diffusion into the hillocks due the outermost CsO_2 layer, which acts as diffusion barrier. Thus, the complet disappearance of the Cs-O hillocks is not seen in AFM images even after 30 days (Figure IV.9).

Moreover, the total hillock volume in crater 3 is much larger than in crater 2, to some extent for the 1st day and especially for the 2nd day (Figure IV.8.b). This difference is due to the different crater depths of craters 2 and 3 (crater 2 is at the middle of the CuPc layer and crater 3 is at the interface CuPc/Si just above the Si substrate). These different bombarded surface materials facilitate the Cs implantation and migration differently, and result after exposure to air, in dissimilar topographies. The solubility of Cs seems to be lower in the Si lattice and enhances the migration of Cs atoms towards the surface[118,119]. Thus after exposure to air, crater 3 produces larger hillocks than crater 2 (Figure IV.8). This difference decreases after 4 days in air, i.e. when the size of the Cs-O hillocks starts decreasing.

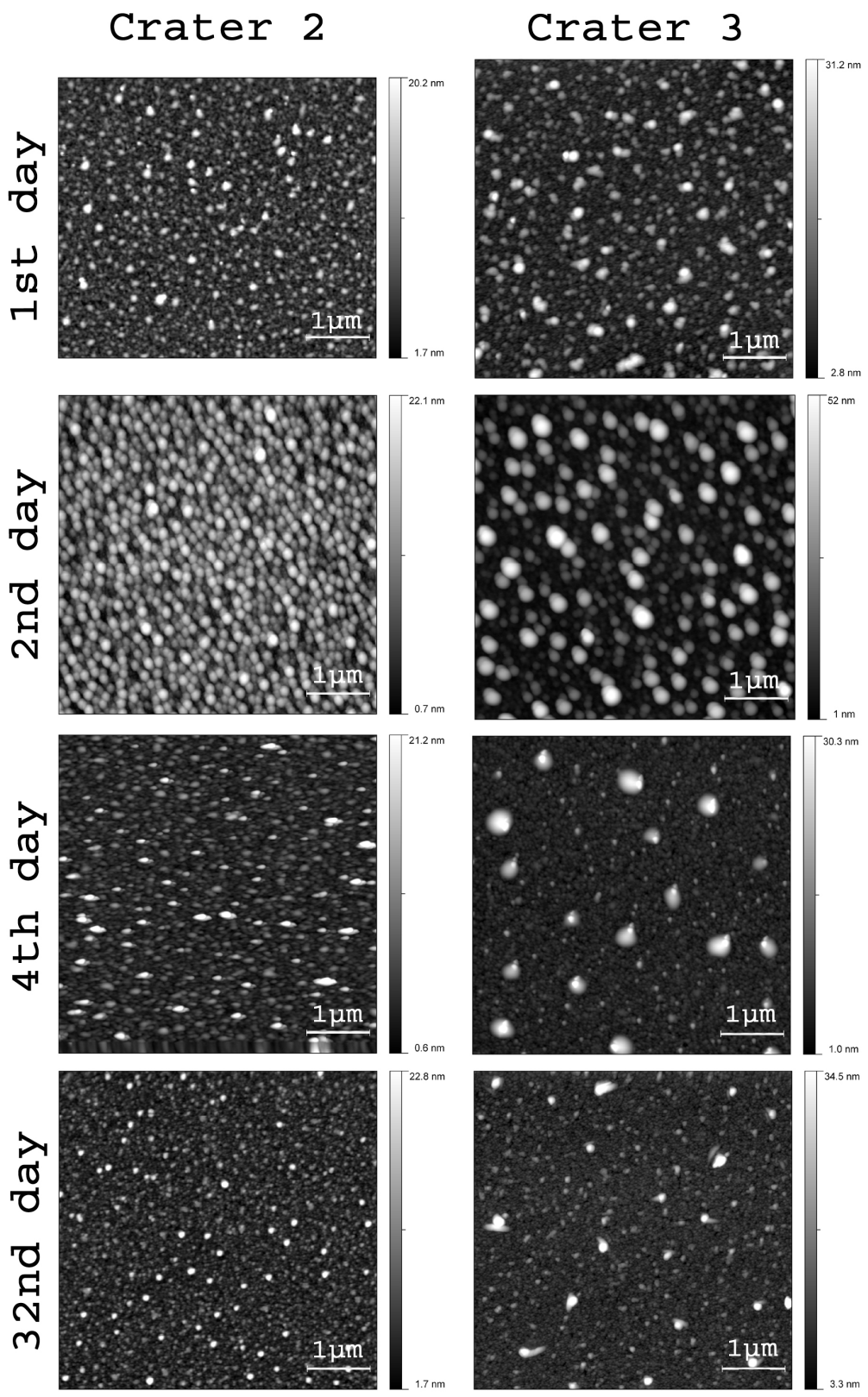

Figure IV.9: *Development of Cs-O hillocks in AFM image as a function of days in air for sample A2b.*

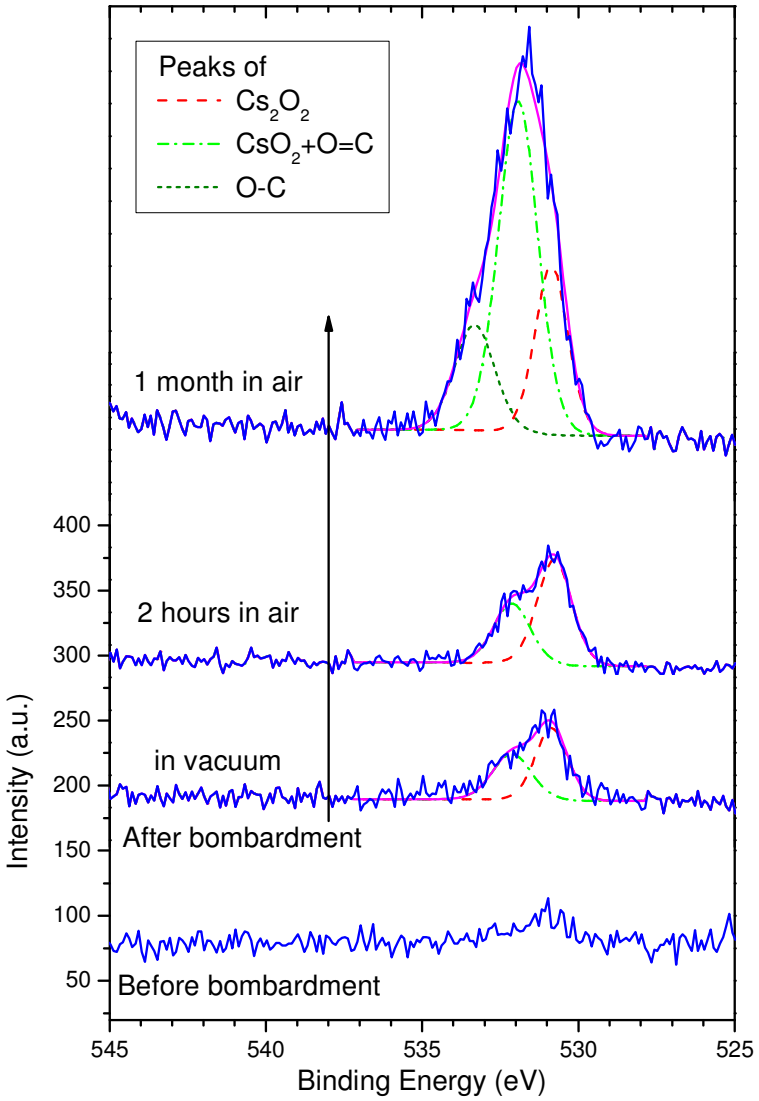

Figure IV.10: *O1s XPS spectra obtained for samples before and after bombardment by low-energy Cs^+ ions: kept in vacuum, exposed to air for 2 hours and for more than a month in air for sample S5.*

XPS spectra were recorded on the surface of thick CuPc films (sample S5) before and after bombardment by low-energy Cs^+ ions. The spectra were recorded for samples kept in vacuum, exposed to air for 2 hours and for more than a month in air. The energy of the XPS spectra in the craters were calibrated by moving all Cs $3d_{5/2}$ peaks to the position of caesium oxides at the 724.2 eV binding energy (BE)[125]. The O1s spectra are shown in Figure VI.10. On the surface of non-irradiated CuPc films, O_2 adsorption was found. Different Cs oxides were found on the craters stored under vacuum conditions (~ 10^{-8}

mbar). The spectrum of O 1s contains a main peak at ~530.3 eV and a small one at ~531.8 eV, which correspond to Cs_2O_2 and CsO_2, respectively[124,125,132]. After exposure to air, a much larger amount of O_2 is detected in the craters. Both O 1s peaks for Cs_2O_2 and CsO_2 were found in those craters. Compared to the crater kept in vacuum, the intensity of O 1s spectrum of the crater exposed to air is more important; especially the CsO_2 peak grows. After more than 1 month at air, the O 1s peak at 531.8 eV (CsO_2) becomes the main peak, however, the enlargement of this peak shows that irradiated organic matter was also oxidized during that time period. During the same period, the development of a C 1s peak at 288 eV and the enlargement of the C 1s peak at 284 eV towards higher BE after exposing the sample to air proves the formation of C=O (287.9 eV) and of C-O (286.6 eV) bonds.

With these results, the impact of air contact for Cs-implanted surfaces on subsequent analyses becomes obvious. For SIMS, the presence of oxygen can increase the Cs surface concentration, which reduces the electron work function and changes the secondary ion ionization probabilities. With the dots, the ionization probabilities are changing locally and leading to artefacts as shown in Figure IV.3. Interpretation of AFM images becomes also challenging. Therefore, good vacuum conditions are necessary to maintain the original surface. For subsequent analyses, transfer under UHV conditions is also required.

IV.4. Influence of sample composition on Cs-O hillocks formation

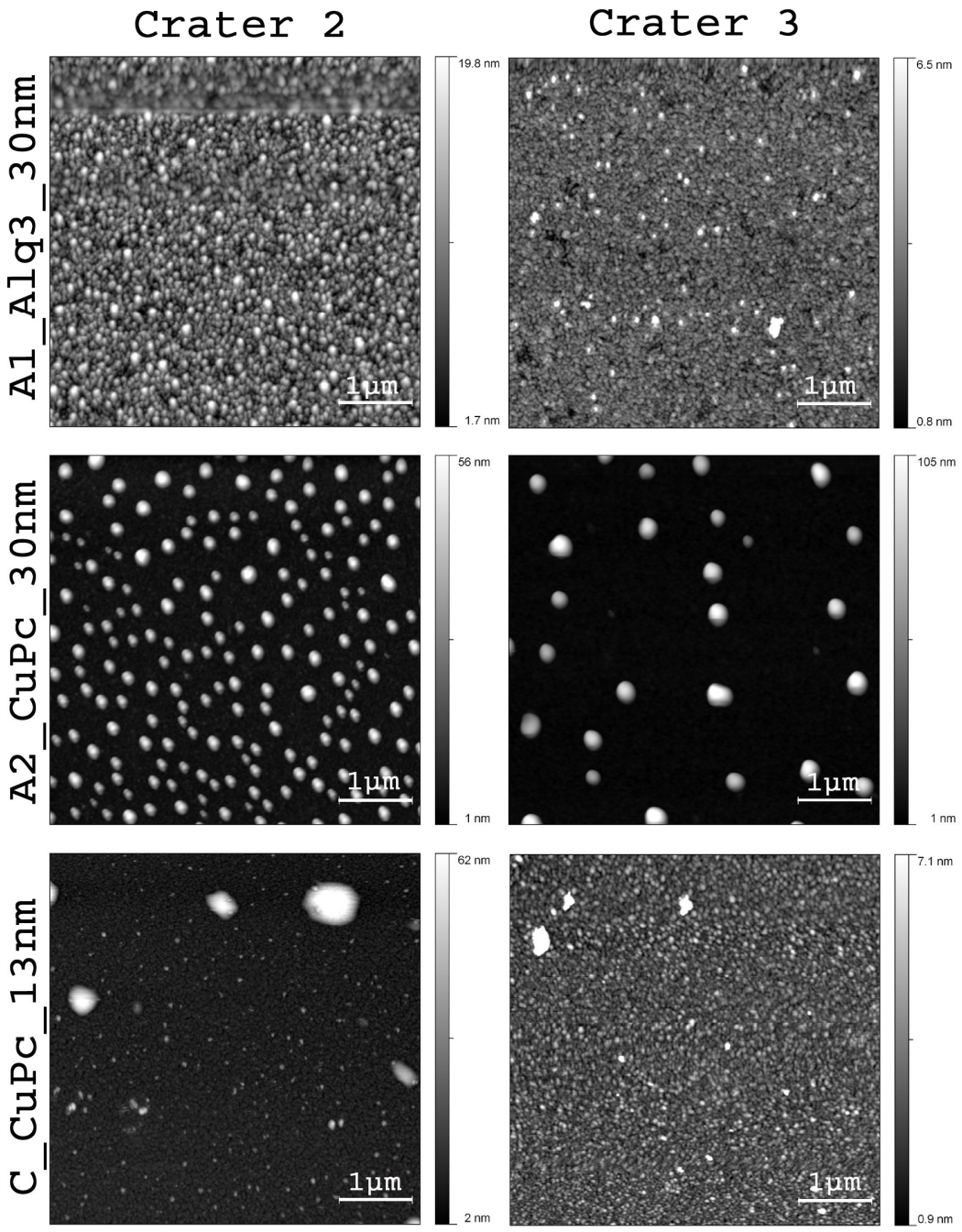

Figure IV.11: *5 x 5 µm² AFM images of craters 2 (left) and 3 (right) of sample A1, A2b and C1 after air exposure of 4 days.*

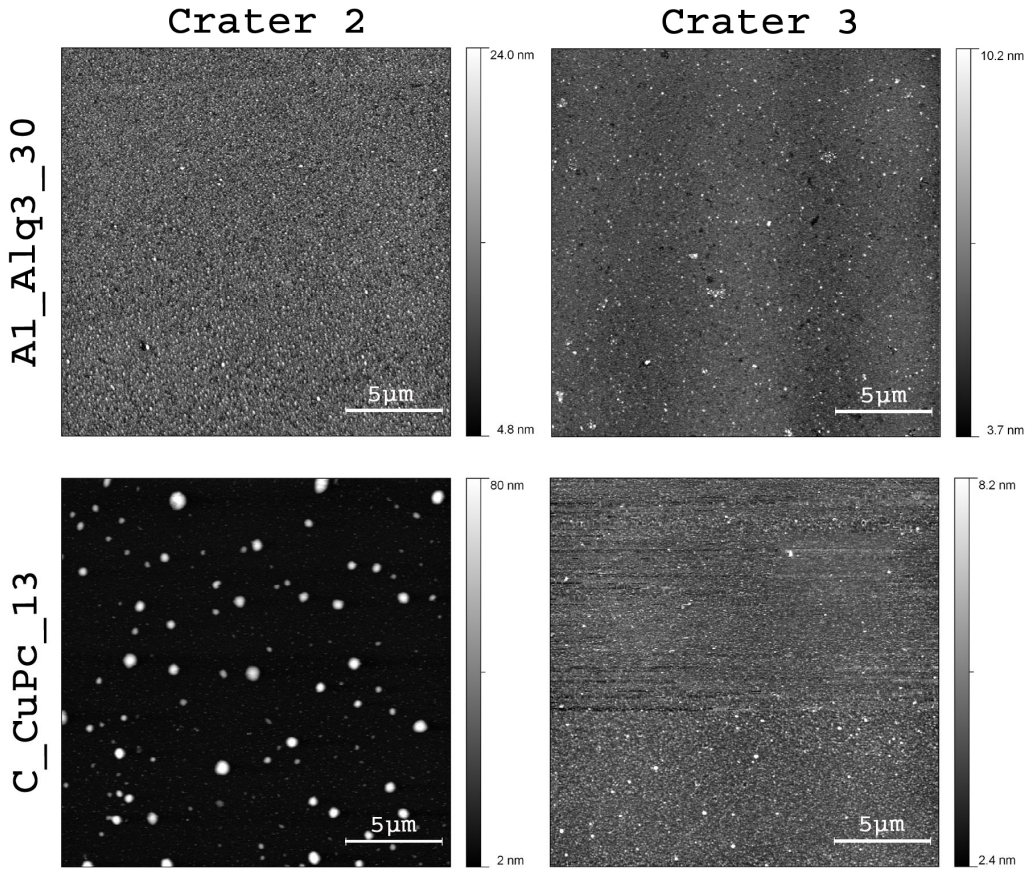

Figure IV.12: *20 x 20 µm² AFM images of craters 2 (left) and 3 (right) of sample A1 (top) and sample C1 (bottom) after air exposure of 4 days.*

In Figure IV.11 and IV.12, the dot formation after exposure to air is compared for samples of different organic materials (Alq_3 and CuPc) and of different thicknesses and preparation methods (samples A2b and C1). The results show that the Cs-O hillock appearance depends not only on exposure time but also on sample composition and preparation. Figure IV.11 shows the AFM images of craters 2 and 3 of the samples A1, A2b and C1. In samples A2b and C1 containing CuPc, Cs islands appear in craters with varying amount and size (Figure IV.11). Compared to sample A2b described above, sample C1 has a thinner CuPc layer (13 nm for sample C1 and 30 nm for sample A2b) and was prepared using a cryo stage. Varying the deposition temperature was proven to change the film morphology[34,36] and to reduce the surface roughness[36,39]. Therefore, the difference in deposition temperature should create dissimilar

layer densities and interface qualities. This changes the implanted stationary Cs concentration during Cs^+ bombardment from sample C1 to sample A2b. Therefore, after exposure to air, less islands of Cs_2O_2 are formed in sample C1 than in sample A2b. Moreover, comparing the Alq_3 and CuPc samples, no clearly discernable hillocks appear in all craters of sample A1_Alq_3 (Figure IV.11), even in the AFM images of 20 x 20 μm^2 size (Figure IV.12), while the hillocks in the craters of sample A2b_CuPc are dense and well defined (Figure IV.11). Therefore, the diffusion and reaction of Cs with O_2 in air and the Cs-O evolution in the Alq_3 and CuPc samples are different. The XPS results from craters of single films of Alq_3 and CuPc (samples S4 and S5) will reveal the difference (Figure V.13).

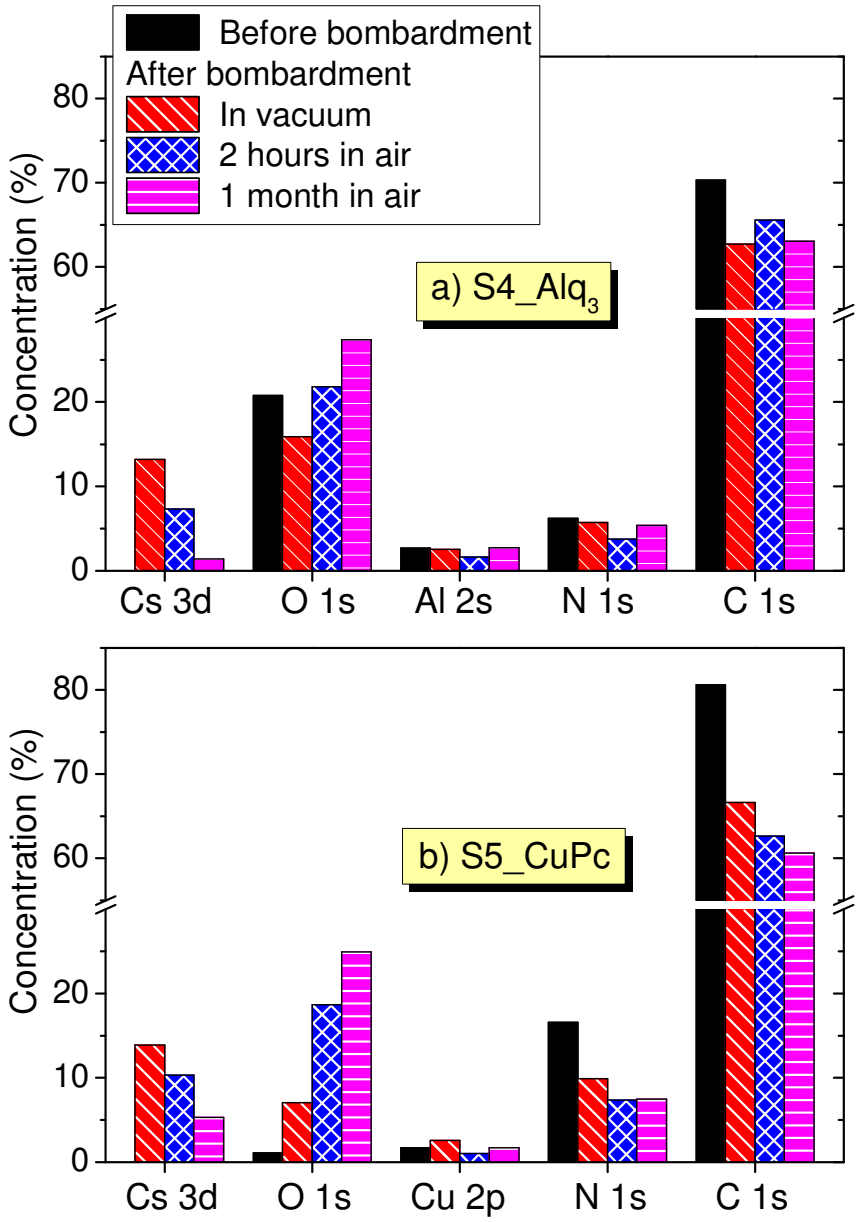

Figure IV.13: *Elemental concentrations by XPS of samples S4_Alq$_3$ (a) and S5_CuPc (b).*

Figure IV.13 shows the atomic concentration of the different elements on the S4_Alq$_3$ and S5_CuPc surfaces calculated from XPS analysis for different conditions: before bombardment, after bombardment including ultra high vacuum transfer, after 2 hours in air and after 1 month in air. No remarkable variation in metal concentration is seen for both samples. We will concentrate only on the variation of Cs and O atomic concentrations, as they reflect the Cs diffusion and the O_2 absorption onto the surface. The variations of N and C

concentrations are only due to the increased amount of O and Cs. Before bombardment, no Cs was found in either pristine sample. There was only ~1% of O detected in the pristine CuPc due to absorption compared to about 20% of O content in the pristine Alq_3. Compared to the theoretical concentration of Alq_3 (~9%), the O surface concentration in the pristine Alq_3 from XPS is quite high and is caused by O_2 and mostly water adsorption during storage in air[231]. After Cs^+ bombardment and transfer under UHV conditions, the Cs surface concentration in Alq_3 is approximately the same as the one for CuPc while the O surface concentration increases for CuPc and decreases for Alq_3. This means that after bombardment in vacuum lower than 10^{-7} mbar, the adsorption of O_2 is observed on CuPc, but less on Alq_3. After exposure to air, more O_2 adsorption is revealed for CuPc (an increase of absolute 17.5% compared to the pristine surface before bombardment and of absolute 11.5% compared to the surface after bombardment but kept in vacuum). This O_2 adsorption is clearly more important than that on the Alq_3 sample (increase of only 1% compared to the surface before bombardment and of 6% compared to the surface after bombardment and stored in vacuum). After higher O_2 adsorption on CuPc, the Cs surface concentration is expected to be reduced more than in the Alq_3 sample. Interestingly, the reduction of the Cs surface concentration after exposure to air in CuPc is less than in Alq_3. The contact with air causes a reduction in Cs of 3.5% in CuPc and of 6% in Alq_3. This signifies that an important amount of Cs diffused to the CuPc surface and that this process is less pronounced for Alq_3. Thus, the different crater topographies for the silver-organic samples of CuPc and Alq_3 (samples A1, A2b and C1) can be explained as follows: in the craters of sample Alq_3, the presence of O in the molecule allows only a small amount of Cs to diffuse to the sample surface after exposure to air, and only a small amount of O_2 absorbs on the surface. Thus no Cs-O hillocks are observed for sample A1_Alq_3. Conversely, in the CuPc sample, which contains no O in the molecule, O_2 absorbs to the Cs containing surface in craters even in high vacuum (~ 10^{-8} mbar). The difference seen between Alq_3 and CuPc proves the arguments of Wehbe about the low efficiency of Cs^+ in Tof-SIMS analysis on the materials containing high amount of oxygen[165,166]: the electropositive Cs has a strong affinity to bond with oxygen atoms in the substrate. This weakens the C-O bonds and leads to a strong fragmentation in ToF-SIMS. In addition, after

exposing the crater of the CuPc sample to air, O_2 absorption becomes even stronger. This becomes possible because of the important migration of Cs from the bulk to the sample surface. Thus the Cs_2O_2 hillocks are formed on the CuPc surface (observed on samples A2b and C1). As previously discussed, O_2 absorption continues during air exposure (seen both for CuPc and Alq_3). In CuPc, after more than 1 month in air, the disappearance of the Cs-O hillocks (recorded on sample A2b) goes along with the increase of the ratio of O to Cs up to 5 (XPS result on sample S5).

IV.5. Conclusions

In this chapter, the topography and the surface composition of Cs^+ bombarded surfaces of metal-organic samples of different organic molecules, thicknesses and preparation methods were investigated by various techniques. The formation of Cs–O grains in SIMS craters of CuPc samples after air exposure has been evidenced using SIMS imaging and AES analysis. The variation of Cs-O hillocks size during exposure to air was recorded using AFM. The appearance and subsequent disappearance of Cs oxide dots was explained by the migration of the implanted Cs to the sample surface where it reacts with O_2 to form $Cs_{11}O_3$, Cs_2O, Cs_2O_2 and CsO_2 successively. The diffusion of Cs to the surface to form Cs_2O_2 in air causes the growth of hillocks after 2 days. Subsequently, the slow transformation from Cs_2O_2 to CsO_2 explains the disappearance of the hillocks after a few days exposure to air. In contrast to inorganic samples where the Cs implanted during the bombardment migrates to the surface and desorbs even under vacuum conditions, in the organic substrates of this study at least a part of the Cs diffuses to the surface only after exposure to air and forms Cs-O islands. The XPS results in craters of CuPc single layered samples in vacuum and after 2 hours and 1 month of exposure to air show the diffusion of Cs to and the absorption of O_2 on the sample surface as well as the transformation from Cs_2O_2 to CsO_2. Metal-organic bi-layered samples of CuPc prepared using different conditions show different sizes and densities of Cs-O hillocks caused by different Cs concentrations in the SIMS craters. In contrast to bi-layered samples of CuPc, the bi-layered sample of Alq_3 does not show any well-defined Cs-O hillocks. The XPS analysis of the Alq_3 single layer sample

shows much less O adsorption and Cs migration than the CuPc samples. This difference is due to the presence of oxygen in the Alq_3 molecule. The oxygen in Alq_3 hinders the diffusion of Cs atoms towards the surface and as a result no well-defined Cs-O hillocks are formed. As far as known, there is no record on the Cs-O dot formation in Cs^+ bombarded craters in SIMS up to now. Therefore, this study can be considered as a first study on Cs-O hillock formation when exposing the Cs^+ bombarded surface to a O_2 rich environment. It presents and explains the formation, the development as a function of exposure to air and variety of Cs-O formation on different materials. When Cs-implanted samples need to be transferred to different instruments for subsequent analyses, UHV transfer is of utmost importance in order to avoid any artefacts. This study includes examples for SIMS, AFM, AES and XPS. For SIMS, the Cs-O hillocks induce local variations in secondary ion yields and topography is changed for AFM. In AFM analyses, the Cs-O hillocks appear only after air exposure and should not be taken into account when characterizing the surface. This remark is important for the surface roughness study in chapter V.

Chapter V
Study of interface width and surface roughness in bi-layered samples

To my knowledge, studies using dynamic SIMS for organic materials in optoelectronic devices are rare. One of the first depth profiles carried out in organic materials was in 1994[232] with a Cs^+ and O_2^+ ion beam at 1 keV. The samples are alternating layers of tetraphenylporphyrins and phthalocyanines. The results show the possibility to separate the different layers in a multi-layered sample with several repeating units. However, the dynamics of the secondary ion signal is poor (less than one order of magnitude) and no comment on interface widths is given. Later, SIMS at low impact energy is used to characterize the degradation/diffusion due to aging in OLED devices[233,234]. The results proved that SIMS can reveal the change in OLED structure. However, neither the origin of the metal diffusion into the organic layer nor the interface widths were taken into account.

In this project, the characterization of interfaces in organic-based optoelectronic systems by low-energy secondary ion mass spectrometry (LE-SIMS) is the main objective. Using the typical cluster ions found in chapter III, an organic multilayer sample has been depth profiled by LE-SIMS at the beginning of the thesis[235]. The different organic layers can be distinguished in the SIMS depth profiles[235]. However, relatively poor resolution at interfaces is a challenge that prevents the characterization at nanometer scale. For optoelectronic devices this is nonetheless an important parameter because the interfaces between layers decide on the performance of the devices (chapter I).

Therefore, in this chapter the interfaces of a series of bi-layered samples presenting a silver and an organic layer on silicon are investigated with a low energy monatomic Cs^+ ions beam. Various conditions have been explored and

compared to surface roughness measured by AFM. Results of depth profiles, interface widths and surface roughness are presented along with possible explanations for the phenomena observed. At the end, the optimal conditions for low-energy Cs^+ analysis are achieved.

V.1. Samples and characterization

In this study, different silver – organic bi-layered samples are studied by SIMS and AFM. Altogether, different organic molecules as well as different layer thicknesses and deposition conditions are studied. The samples A2a and A2b have the same characteristics but were prepared at different times. The sample properties are listed in table V.1.

The SIMS depth profiles are carried out using a Cs^+ primary ion beam at impact energies from 250 eV to 1 keV in positive and negative secondary ion mode on a Cameca SC-Ultra instrument. The impact angle is of 64° for analyses in the positive mode and it varies slightly in the negative mode: 38°, 46° and 51° for 250 eV, 500 eV and 1 keV respectively. Sample rotation is used for the study of irradiation induced roughness. The experimental details for SIMS are described in II.1.4.i.b. After analysis, the time scale in the depth profiles is converted into a depth scale as shown in Figure V.1. The interface is defined at the point of 50% of the maximum intensity of a raising or decreasing edge in a depth profile, i.e. in Figure V.1 the interface InP/Si is at 50% of the secondary ion intensity on the raising edge of the depth profile of $SiCs^+$ or on the decreasing edge of the PCs^+ depth profile. Then, knowing the layer thickness and supposing that the erosion rate is constant in each layer, it is calculated by dividing the depth by the sputtering time. The depth scale is obtained by multiplying the time with the sputtering rate in each layer. For our bi-layered samples, the layer thicknesses are measured by a calibrated QCM during deposition and the Si sputter rates are calculated from TRIM simulation[236-238]. Afterwards, information on interface roughness formed during the growth of the layers is obtained from the SIMS depth profiles by calculating the interface widths.

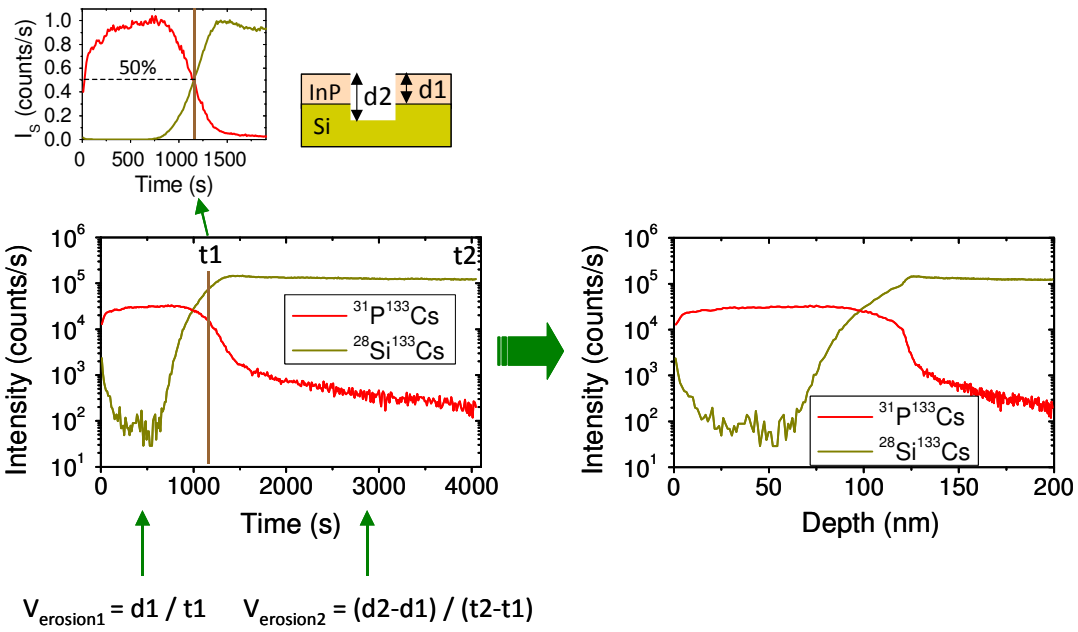

Figure V.1: *Converting the time scale to the depth scale in SIMS depth profiles of a sample of InP on Si.*

The measurement of radiation-induced roughness is similar to the one described in chapter IV. At first, for each sample a depth profile throughout the different layers down to the substrate is realized. Then, using the same conditions, the craters for AFM are prepared by stopping the sputtering at certain depths (at Ag/organic interface, at the middle of the organic layer and at the organic/Si interface). Samples A1, B1, B2 and C1 are bombarded in the negative mode and samples A1, A2b, C1 are bombarded in the positive mode. The samples are transferred in air to the AFM instrument. Finally, the surface roughness in the sputtered craters is measured on a Molecular Imaging PicoSPM LE AFM instrument.

Name	Sample	Layer thicknesses (nm)	Deposition system	Deposition temperature
A1	Ag/Alq_3	30	Angstrom	Room temperature
A2a, A2b	Ag/CuPc	30	Angstrom	Room temperature
A3	Ag/Pc	30	Angstrom	Room temperature
A4	Ag/FePc	30	Angstrom	Room temperature
A5	Ag/ZnPc	30	Angstrom	Room temperature
B1	Ag/CuPc	12	Superlattice	Room temperature
B2	Ag/CuPc	48	Superlattice	Room temperature
C1	Ag/CuPc	13	Angstrom	- 60 °C
C2	Ag/CuPc	30	Angstrom	- 60°C

Table V.1: *List of samples and preparation conditions. For more information, see chapter I.*

For craters sputtered into the CuPc layer, the AFM images exhibit some high hillocks, which evolve as a function of time during which the sample is exposed to air. As described in the previous chapter, these hillocks are formed by Cs-O dots and appear only after exposing the Cs^+ sputtered craters to air. They are not present in vacuum and should not be considered for the calculation of surface roughness. Therefore, in this chapter, the RMS roughness is the roughness without considering the hillocks. It is calculated from the AFM images where the dots are removed by a mask (in IV.3)

V.2. Interface width

V.2.1. Depth profiles and the calculation of interface width

The fragmentation of CuPc and Alq_3 molecules under low energy Cs^+ bombardment has been described in chapter III. For depth profiling, we selected a characteristic fragment of the organic layers leading to high secondary ion yields, i.e. CN^- at m/z=26. The secondary ions of the metals (Cu for CuPc or Al for Alq_3) produce too low secondary ion intensities. The inorganic layers are characterized by Ag^- (m/z=107) and Si^- (m/z=28) intensities. Using these low mass secondary ions we limit the mass interferences, thus the mass resolution of 400 can still be used in order to keep high secondary ion intensities.

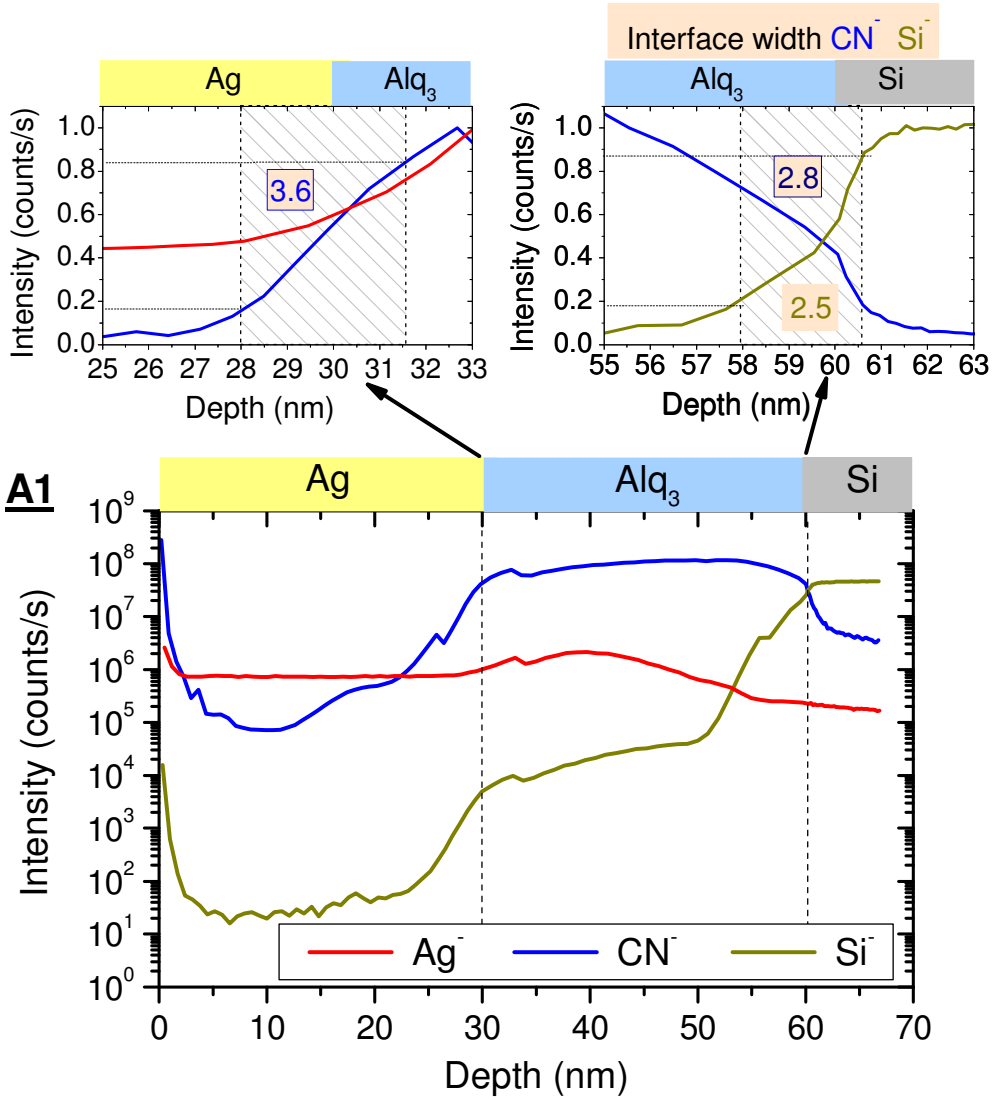

Figure V.2: *Secondary ion intensities as a function of depth in 500 eV Cs^+ energy bombardment for sample A1. Interface widths at Ag/organic and organic/Si interfaces are shown in insets with a linear scale for y axis and the depth profiles are normalized to the maximum intensity. The interface width at the Ag/organic interface is calculated from the CN^- depth profile and at the organic/Si interface is calculated from the CN^- (in blue) and the Si^- (in dark yellow) intensities.*

The depth profiles at 500 eV in the negative mode of sample A1 are shown in Figure V.2. The organic layers are characterized by high intensities of the m/z=26 (CN^-) cluster ions (about 10^8 counts/s in organic layer compared to less than 10^6 counts/s in Ag layer). The high m/z=26 (CN^-) intensities in the Ag

layer are due to mass interferences caused by residual gas in the analysis chamber. The Si substrate is characterized by an increase of the intensity at m/z=28 (Si^-) above 10^7 counts/s. In the depth profile of sample A1, the intensity at m/z=28 increases by more than one order of magnitude when the depth profile passes from Ag layer to Alq_3 layer (less than 10^2 counts/s in Ag layer and about 10^4 counts/s in Alq_3 layer). This is caused by mass interferences with secondary ion clusters at m/z=28 containing C, N, H, O … which originate from the organic molecules. The high m/z=107 (Ag^-) intensity in the organic layer and in the Si substrate will be discussed in the chapter VI.

In insets of Figure V.2 and in table V.2, the different SIMS interface widths at 500 eV are compared. The two insets in Figure V.2 show the depth profiles and the interface width at two interfaces. At the Ag/organic interface, no drop in the Ag^- depth profile is seen while an almost linear increase is seen in the CN^- depth profile. However, this behaviour is not seen at the organic/Si interface, where both CN^- and Si^- depth profiles present a change in slope when passing the interface. The changes in slope are also influenced by the difference in erosion rates between the organic and Si films: the sputtering rate in Si substrate is quite low comparing to the one in organic layer. In reality, the sputtering rate change gradually when passing from one layer to the other, however for simplifying the calculation, the erosion rate was supposed to be constant in each layer and changes abruptly at the interface. The interface width at the different interfaces is calculated using the distance between 84% and 16% of the maximum secondary ion intensities[239] at the rising edge of the CN^- (Ag/organic interfaces) and Si^- depth profiles (organic layer/Si interfaces) as shown in the insets of Figure V.2. For the last interface, the interface width is compared to the one calculated from the falling edge of the CN^- depth profiles. Calculating interface width at the Ag/organic interfaces using the falling edge is not possible because the intensity of silver containing cluster ions does not decrease.

Interface width (nm)	Ag/Organic	Organic/Si	
	Rising edge of CN^-	Rising edge of Si^-	Falling Edge of CN^-
A1	3.6	2.5	2.8
A2a	5.9	2.9	3.5
B1	3.9	2.0	3.3
B2	9.2	4.0	6.7
C1	2.2	1.4	2.5

Table V.2: *Interface widths at 500 eV at the Ag/CuPc interface of samples A2a, B1, B2 and C1.*

The interface widths of samples A1, A2a, B1, B2 and C1 are presented in table V.2 (depth profiles are in Figures V.2, V.3 and V.4). In all samples, the interface width is larger at the Ag/organic interface than at the organic/Si interface. Moreover, at the organic/Si interface, the interface width calculated from the rising edge of Si^- is smaller than the one calculated from the falling edge of CN^-. In literature, the interface width calculated from the rising edge is shown to be less influenced by the primary ion beam (e.g. impact energy, incidence angle) than the one calculated from the falling edge[70,240]. Therefore, although the interface width calculated from falling edge represents well the sputter-induced mechanisms and is usually used in SIMS[241], the one calculated from rising edge should fit better the real interface roughness. Consequently, from now onwards, only the values calculated from the rising edge of CN^- and Si^- depth profiles in negative mode and of CsC^+ and $CsSi^+$ depth profiles in positive mode are used to characterize interface roughness at the Ag/organic and organic/Si interfaces.

V.2.2. Comparison of positive and negative mode

In this part, the depth profiles in negative mode and in positive mode are presented. Figure V.3 shows the depth profiles of sample A2a in both positive and negative mode at 500 eV. In the negative mode, the depth profile is similar to the one of sample A1 presented previously (Figure V.2). However, for sample A2a, the m/z=28 (Si^-) and m/z=26 (CN^-) intensities in the Ag layer are one order of magnitude higher than in sample A1 (2.10^3 counts/s for m/z=28 and 3.10^5 counts/s for m/z=26). A possible reason is the mass interferences coming from the organic layer as this sample got scratched during the transport.

In the positive depth profile, the organic layers are characterized by high intensities of the m/z=145 (CsC^+) cluster ions (about 10^3 counts/s in organic layer compared to less than 10^1 counts/s in Ag layer). The Si substrate is characterized by an increase of the intensity at m/z=161 ($CsSi^+$) of more than 10^3 counts/s. The high m/z=240 ($CsAg^+$) intensity shows the Ag layer. When comparing the depth profile in positive mode and negative mode, intensities of CsC^+ and $CsSi^+$ are about 4 orders of magnitude lower than the intensities of CN^- and Si^- ions. The high secondary intensities of CN^- and Si^- ions are the result of negative secondary yield enhancement when using a Cs^+ primary ion beam[242]. However, the behaviour of these depth profiles in positive mode are similar to the ones in negative mode. The non-zero intensity at m/z=145 (CsC^+) in Ag layer is due to mass interferences caused by residual gas in the analysis chamber at 10^{-8} mbar. Moreover, because of mass interferences from secondary ion clusters at m/z=161 containing C, N, H, O and coming from the organic layer, the intensity at m/z=161 ($CsSi^+$) increases when the depth profile passes from the Ag layer into the CuPc layer. In addition, the Ag containing secondary ions in both positive and negative mode of sample A2a show a similar trend than in sample A1 (Figure V.2). Similar to the negative mode, the interface widths are calculated from the rising edge of CsC^+ and $CsSi^+$ intensities. There is a large diffusion of Ag into the organic layer. However, in the insets of Figure V.3, at the Ag/organic interface, the depth profile in the negative mode (with an incidence angle of 46°) shows a more important Ag diffusing than in the positive mode with 63° even though it has a

smaller interface width. This will be discussed in more detail in chapter VI. At the CuPc/Si interface, there is a peak in the $CsSi^+$ depth profile near the interface with the Si substrate. It is due to the matrix effect coming from the native oxide layer on Si. Moreover, in the inset, the change of the slope of the curves due to changing erosion rates at the CuPc/Si interface is more pronounced in the positive mode than in the negative mode.

The interface widths in negative mode are smaller than the one in positive mode and this for both Ag/CuPc and CuPc/Si interfaces. It is also true for the other samples analysed at different impact energies in Figure V.4. This difference has probably two origins. It can be caused by the different incident angles (38-51° in negative mode and 64° in positive mode, see SIMS analysis conditions in chapter 2), which influence the surface roughness[199]. This will be discussed later.

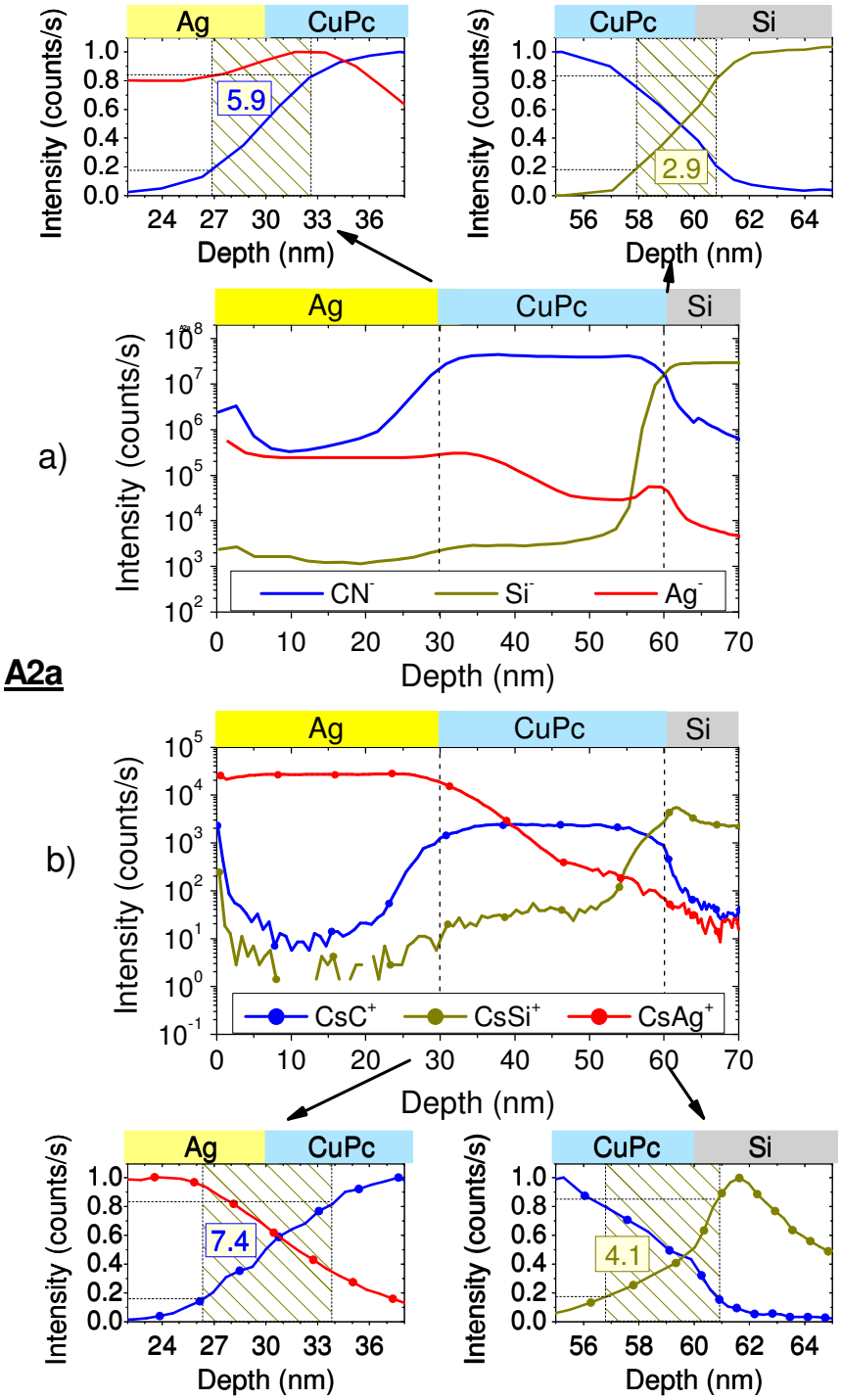

Figure V.3: *Secondary ion intensities at 500 eV as a function of depth for sample A2a a) in negative mode and b) in positive mode. Interface widths at the Ag/organic and organic/Si interfaces are shown in insets with a linear scale for y axe and the depth profiles are normalized to the maximum intensity. The interface width at the Ag/organic is calculated from the CN⁻ and CsC⁺ depth profiles and at the organic/Si is calculated from the Si⁻ and CsSi⁺ depth profiles.*

V.2.3. Different organic molecules at different impact energies

Figure V.4 shows the interface widths of different impact energies in positive and negative mode for the sample A1 of Alq_3 and the samples A2a, A3, A4 and A5 of different phthalocyanine derivatives (For depth profiles see Figures VI.2 and VI.3 in the chapter VI). Similar to the result at 500 eV from the A1_Alq_3 sample presented previously, the interface widths at both interfaces in negative mode are smaller than in positive mode for a sample at the impact energies of 500 eV and 1 keV. The explanation has been given in the previous paragraph: the different incident angles in negative and positive modes where the larger incidence angles in the positive mode are expected to produce more roughness (section V.2.2.).

At a given impact energy and at each interface, the interface widths may vary by up to 4 nm for the different samples. For the impact energy at 1 keV, they lie between 2.7 - 4.8 nm at the Ag/organic interface, and between 1.3 - 3.0 nm at the organic/Si interface in negative mode. In positive mode, the interface width shows larger values: between 5.9 - 7.5 nm at the Ag/organic interface and between 3.7 - 5.2 nm at the organic/Si interface. Moreover, for some samples they tend to worsen when reducing the impact energy, at both the Ag/organic and organic/Si interfaces in the negative and positive modes. Comparable data is difficult to find for organic matter. For inorganic samples, Cs^+ bombardment has been largely studied[199,240,243,244]. In these studies, the resolution parameters are better at low impact energies. In this context, as mentioned in II.1.3.iv, Wittmaack stated[153,245] that for a given primary ion species and a fixed impact angle, profile broadening increases with increasing beam energy. Furthermore, profile broadening is expected to worsen for larger incidence angles. This was observed by Fukumoto who shows an increase of RMS roughness on SiC sample when the 1 keV Cs^+ beam impact with an incident angle of around 60°[199]. Similarly, Kataoka et al. analyse depth profile a 6 Sb deltas on Si substrate with a spacing of 5 nm by Cs^+ beam at impact energy from 250 eV to 1 keV. His results suggest that to avoid surface roughening and profile shifts, the impact angles should be from 45 to 50° for

250 eV, 50 to 55° for 500 eV and 55 to 60° for 1 keV[197,198]. Above these incident angles, the sputtering – induced roughness and below these incident angles, the distortion in the profile due to the accumulation of Cs at the sample surface are reasons for the worse depth resolution[197]. Both results agree with those of van der Heide[246]. As the organic molecules get completely damaged during sputtering, mechanisms leading to roughness formation can be expected to be similar. For our results, in positive mode, the incident angle of 64° is above the critical angle which means an important contribution of roughness to interface width broadening. However, in negative mode, the incidence angles are below the critical angle (38° at 250 eV, 46° at 500 eV and 51° at 1 keV). In this situation, difference in interface width when changing the impact energy would be related to variations in impact angle which are linked to the energy. This point needs further investigation which will be done in the section V.3. Other mechanisms might contribute to the loss in depth resolution.

In addition, the interface widths at the organic/Si interface separates into two groups, one of the three samples A2a, A4 and A5 are quite close in most situations and the other group with the two samples A1 and A3 about 1 nm above the previous group. As described in section I.1, the samples A1 and A3 have a low density and contain only the light atoms Al, C, N, O in the molecules. The samples A2a, A4, A5 have all a similar molecular structure, with a complex with a metal atom in the centre of the phthalocyanine group. They have a slightly higher densities and contains also the larger transition metals Fe, Cu, Zn in the molecules. The difference in structure of these two groups leads to different displacements of the surface target atoms, thus possibly creates different surface roughness. This roughness difference may be the reason for the 1 nm difference in interface width between the two groups.

Furthermore, similar to sample Alq_3, the SIMS interface widths of the MPc samples at the Ag/organic interface are much larger than the one at the organic/Si interface. This is valid for both negative and positive secondary ion mode with the impact energies varying from 250 eV to 1 keV. This may be due to the intrinsic property of the samples and also to the analysis method. At first, for all samples, the deposition of the organic film on a Si substrate certainly develops a surface roughness on top of the organic layer. In addition,

the metal deposition on organic layer may cause metal diffusion into the organic layer. Thus, the Ag/organic interface width is naturally larger than the organic/Si interface. At second, in SIMS analyses, the mean depth of origin of the sputtered atoms is inversely proportional to the material density[203-205]. In this situation, the density of the organic material studied (in I.2) is clearly smaller than the one of Si (d_{Si}=2.33[247] g/cm^3). Therefore, sputtering–induced mixing is more pronounced in the organic layers than in the Si substrate, thus the sputter–induced broadening may be more important at the Ag/organic interface than at the organic/Si interface.

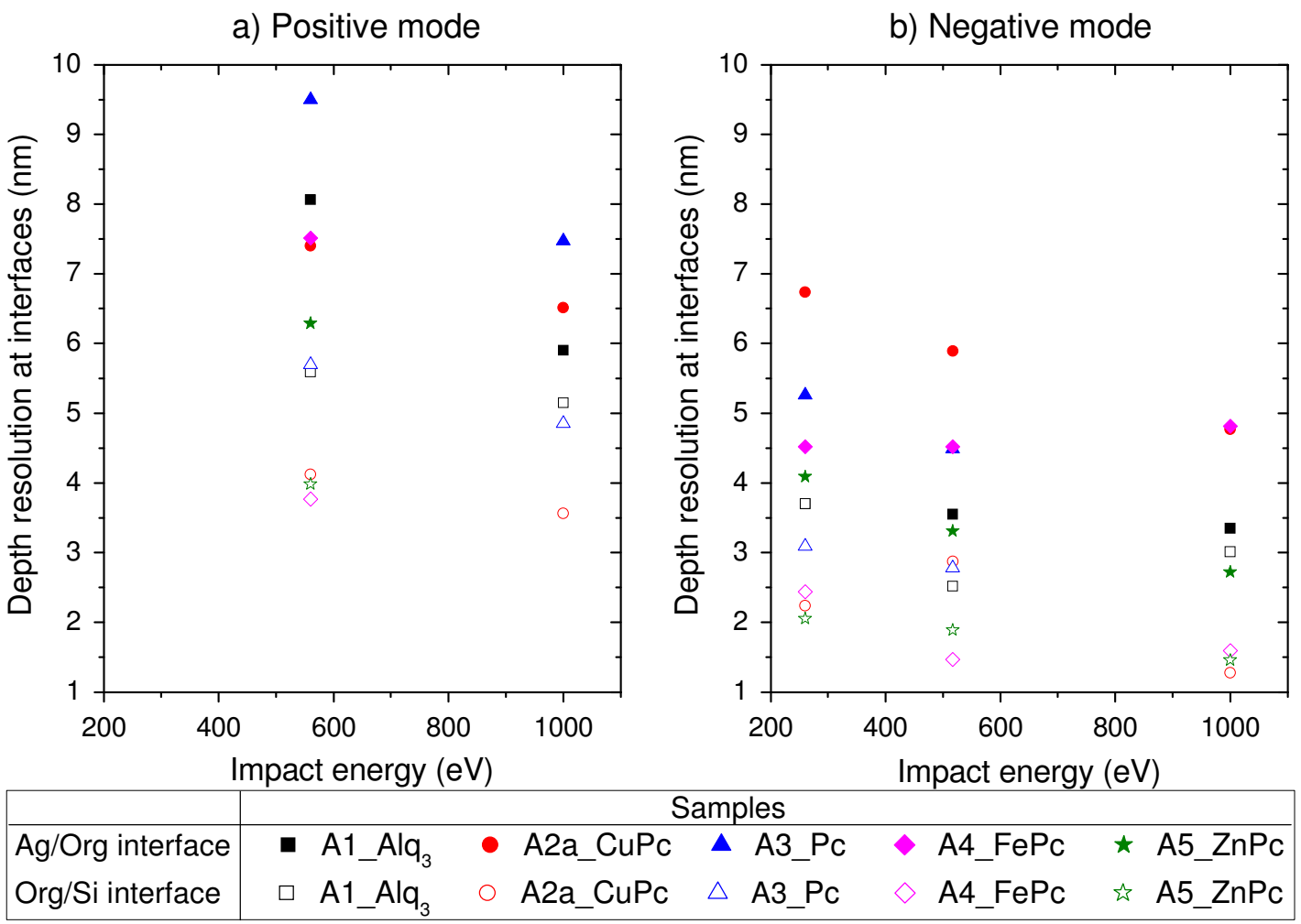

Figure V.4: *Interface widths of samples A1-A5, in a) positive mode at 250 eV, 500 eV and 1 keV and b) negative mode at 560 eV and at 1 keV.*

V.2.4. Different layer thicknesses

Figure V.5 presents the depth profiles in the negative mode and the interface widths at the two interfaces of samples B1 and B2. In sample B1, the intensity at m/z=26 (CN^-) and at m/z=28 (Si^-) in the Ag layers are higher than in the sample B2 (~10^7 counts/s for m/z=26 and ~10^3 counts/s for m/z=28). Similar to sample A2a in V.2.2, it is due to mass interferences coming from the CuPc layer (scratched surface). Similar to the samples A1 and A2a in the Figures V.2 and V.3, the inset of depth profiles at the Ag/organic interface of B samples show a smooth slope after converting the time scale into a depth scale. In addition, the Ag diffusion is also clear in these samples. At the organic/Si interface, the matrix effect is seen in sample B1 but not in the sample B2 and the change of erosion rate from the organic layer to the Si layer is less brusque than in the samples A1 and A2a.

The samples B1 and B2 have been prepared using the same conditions in the lab built superlattice VTE instrument. However, the interface widths of sample B2 are larger than those of the thinner sample B1. They are of 9.2 and 4 nm for sample B2 and 3.9 and 2 nm for sample B1 at the Ag/CuPc and CuPc/Si interfaces respectively. As the sample B2 has a thicker organic layer than sample B1, it is expected having a rougher organic surface and a larger Ag/organic interface width. Our SIMS interface width at the Ag/CuPc interface agrees well with this assumption. The smaller interface width at the CuPc/Si interface of sample B1 compared to sample B2 may be a result of roughness development during ion bombardment, which will be discussed in the next section.

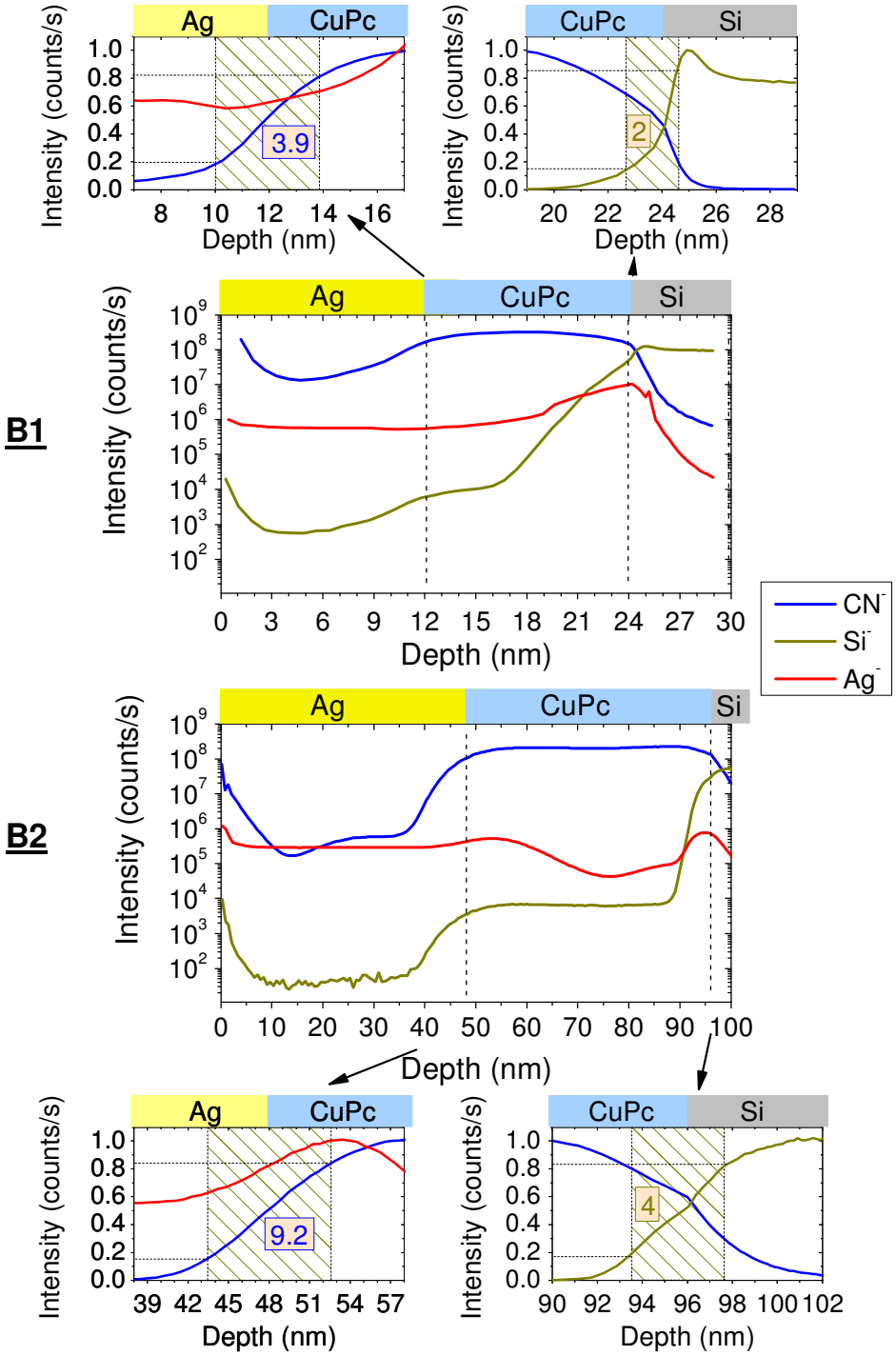

Figure V.5: *Secondary ion intensities as a function of depth for samples B1 and B2. Interface widths at Ag/organic and organic/Si interfaces are shown in insets with a linear scale for y axis and the depth profiles are normalized to the maximum intensity. The interface width at the Ag/organic interface is calculated from the CN⁻ depth profile and at the organic/Si interface is calculated from the Si⁻ depth profile.*

Furthermore, when compared to the samples A2a – A4 prepared in the Angstrom VTE instrument with slightly thinner layers (30 nm layer thicknesses), the interface widths in the negative mode of sample B2 are largely worse than in the A samples. This is probable due to the thicker layers in sample B2 and also the different preparation instruments. The lab-built VTE system has a typical design with a sample – sources distance of haft the one of Angstrom system and different deposition rates (chapter I). This leads to different surface roughness as well as different film properties (density, structure…). As a result, the SIMS analyses give different interface widths.

V.2.5. Low temperature deposition

Figure V.6 shows the depth profile in negative mode of sample C1 prepared at low temperature and the interface width at two interfaces. Similar to sample B1, due to mass interferences coming from the organic layer, the intensity at m/z=26 (CN^-) ions in the Ag layer and of m/z=28 (Si^-) in the Ag and CuPc layers are higher than in the A samples. Both samples B1 and C1 have less than 13 nm layer thicknesses. Therefore, scratches on the sample surface become easily deeper than one layer. Although the Ag^- depth profile shows similar Ag diffusion as in other samples, the sample C1 is the only sample in our experiments that shows also a small decrease in the Ag^- intensity at about 2 nm before the interface Ag/CuPc. Although the sample B1 has similar layer thicknesses than sample C1, the Ag^- depth profile of sample B1 does not change when passing from the Ag layer into the CuPc layer. A remark for the sample C1 is that the interface width is calculated based on the interval between 16% and 84 % of the highest and lowest intensities in the raising edge in the CN^- and Si^- depth profiles. Due to mass interferences, the lowest intensities are relatively high (which is not observed for other samples). In addition, the interface widths in SIMS depth profiles at the Ag/CuPc and CuPc/Si interfaces are all larger in sample B1 (3.9 and 2 nm) than in sample C1 (2.2 and 1.4 nm). Similar trends have been obtained for the other samples. Their data is shown in table V.3.

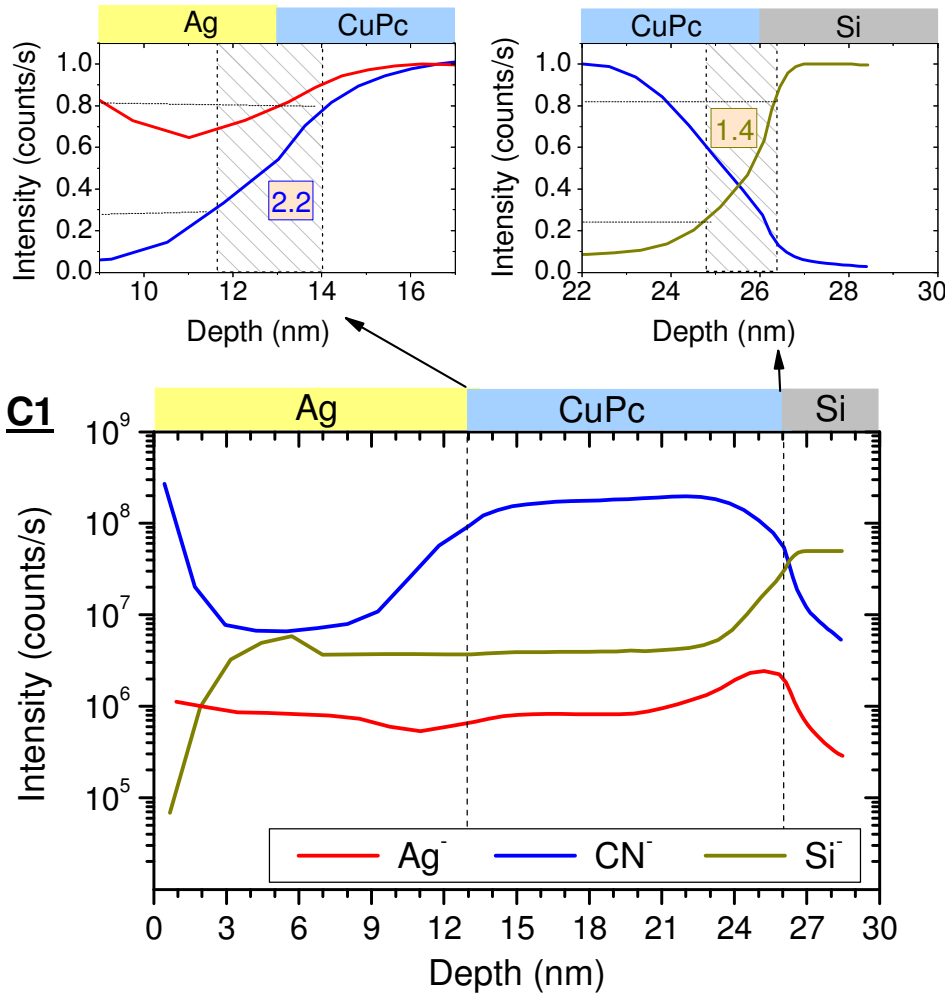

Figure V.6: *Secondary ion intensities as a function of depth for sample C1. Interface widths at the Ag/organic and organic/Si interfaces are shown in insets with a linear scale for y axis and the depth profiles are normalized to the maximum intensity. The interface width at the Ag/organic interface is calculated from the CN depth profile and at the organic/Si interface is calculated from the Si depth profile.*

Sample	Layer thicknesses (nm)	Ag/organic interface	Organic/Si interface
Low temperature deposited sample			
C1	13	2.2	1.4
C2	30	3.2	1.8
Room temperature sample			
B1	12	3.9	2.0
B2	48	9.2	4.0
A2a	30	5.9	2.9

Table V.3: *Interface width at 500 eV in negative mode at interfaces of samples prepared at low temperature and at room temperature in negative mode. All the samples contain a CuPc organic layer.*

Table V.3 compares the interface width at the two interfaces of several CuPc containing samples with different layer thickness deposited at low temperature and at room temperature. Similar to the samples prepared at room temperature, the C samples prepared at low temperature have smaller interface width at the organic/Si interface (better than 1.8 nm) than at the Ag/organic interface (worse than 2.2 nm). When comparing the layer thickness, the result of the C samples is similar to the B samples: thinner sample has smaller interface width than the thicker ones. Moreover, compared to the samples prepared at room temperature, the C samples show smaller interface widths with less than 3.2 nm at the Ag/CuPc interface and less than 1.8 nm at the CuPc/Si interface. These results agree with the studies by others authors using different techniques[39,41,42]: i.e. thin films prepared at low temperature have smoother surface or a thicker film has a rougher surface than a thinner one (section I.2). Moreover, in our study, the SIMS depth profiles show well-defined Ag and organic films with layer thicknesses down to 12 nm. This agrees with the study of Jin et al.[39] on a series of three stacks of CuPc/Ag multilayers prepared in a similar method. For layers thinner than 8

nm, metal atoms and molecules get completely mixed during deposition and the layers cannot be distinguished by TEM.

V.2.6. Conclusions

In brief, the SIMS interface width depends not only on analysis conditions but also on sample properties. The latter includes interface position, organic layer composition and thickness as well as on sample preparation conditions. As the SIMS interface widths contain information on the samples and analysis artefacts, the latter needs to be minimized. In our study, the interface widths calculated from CsC^+ and $CsSi^+$ secondary ion intensities in positive depth profiles are larger than the ones calculated from CN^- and Si^- intensities in negative depth profiles. This is due to the roughness development during analysis and the mass interference observed for the high mass ions CsC^+ and $CsSi^+$. When increasing the impact energy, the SIMS interface width tends to reduce, at least for most samples. At the lowest impact energy, (38° at 250 eV) the interface width is always larger than at 500 eV or 1 keV. In the positive mode, the incident angle of 64° is above the "critical angle" for roughness formation, thus the increase of surface roughness leads to larger interface widths. Therefore, for the analysis of organic materials, reducing the impact energy to too low values is not recommended in the Cameca SC-Ultra instrument in order to achieve good depth resolution. In our study, for most samples with 30 nm individual thicknesses, the best analysis condition is in the negative mode at 1 keV and 51°.

In this study, SIMS analyses are shown to be able to characterize to some extent the properties of different interfaces. In the depth profiles of all samples and for all analysis conditions, the SIMS interface width at the organic/Si interface is better than at the Ag/organic interface. Both, sample properties and analysis artefacts contribute to this. Firstly, the roughness development during sample preparation and the metal diffusion cause larger interface widths at the Ag/organic interface than at the organic/Si interface. Secondly, the lower density of the organic materials results in a larger sputter–induced broadening at the Ag/organic interface than at the organic/Si interface. With

the same layer thicknesses and preparation conditions, the SIMS interface width for each analysis condition at each interface shows an interval of less than 4 nm for different organic materials. In each situation, at the organic/Si interface, the samples of MPc show a better SIMS interface width than the one of samples A1_Alq_3 and A3_Pc. This is due to the difference in density and molecular structure of the organic material. In addition, when using the same organic molecule, the SIMS interface width can reveal the influence of sample preparation conditions on the quality of the interfaces. For example, samples with thinner layers have better interface widths. This is due to the development of roughness during the deposition process. Moreover, when having the same organic molecule, the sample prepared using a cooled substrate during the deposition process shows a better SIMS interface width. This results from minimized surface roughness and material diffusion during deposition using a cooled substrate. In summary, different morphologies of metal - organic interfaces can be investigated by SIMS depth profiling.

To summarize, in SIMS depth profiling, the surface roughness development during analysis is one of the important factors which contribute to the analysis artefact when determining the SIMS interface resolution. 500 eV as well as 250 eV bombardment are expected to produce better results than 1 keV Cs^+ bombardment, but which is not always observed for our data. It is the subject of our next section, where the surface roughness is investigated at different positions in samples of CuPc and Alq_3 at different analysis conditions.

V.3. Roughness formation during SIMS analysis

The depth profiles and SIMS interface width at interfaces of metal – organic samples were shown in the previous section with impact energies from 250 eV to 1 keV. In this section the formation of surface roughness during SIMS analysis is studied to see if it is the main mechanism behind the degradation of depth resolution. The investigation of roughness formation is of interest for analysis conditions where the depth resolution is degraded, i.e. 500 eV and

250 eV. Investigating all conditions would have taken too much time, so we focus on 500 eV.

V.3.1. Results

In this part, the roughness is characterized at certain depths of the A1, A2b, B1, B2 and C1 samples. Figure V.7 shows the roughness at the crater bottom at different depths of samples A1 and A2b. For sample A1 at all analysis conditions, the roughness varies with crater depth. The surface is smoothened during the sputtering of the 30 nm Ag layer down to the Ag/Alq_3 interface. There is a roughness of ~1.3 nm on the non-irradiated surface and of ~1.0 nm at the Ag/Alq_3 interface. After sputtering half of the Alq_3 layer, the roughness increases by more than 1 nm (roughness of 2 - 2.5 nm), but reduces when coming close to the Alq_3/Si interface (roughness of ~1.0 nm). For this sample, roughness in the negative mode at an impact angle of 46° is not clearly reduced by using sample rotation during the SIMS analysis. In addition, the roughness in positive mode at 63° incident angle is not clearly larger than in negative mode. Furthermore, at the Ag/Alq_3 and Alq_3/Si interfaces, the surface roughness measured by AFM (~1.0 nm) is lower than the SIMS interface width (interface widths of 3.6 and 2.5 nm in negative mode, and of 8.1 and 5.6 nm in positive mode at Ag/Alq_3 and Alq_3/Si interfaces respectively). For sample A2b irradiated in the positive mode (500 eV at 63°), the behaviour changes. After bombardment, the roughness increases from 0.8 nm at the sample surface to 1.2 nm at the Ag/CuPc interface and remains constant throughout the organic layer. However, again, the interface width is not limited by roughness formation at the crater bottoms during the Cs^+ sputtering.

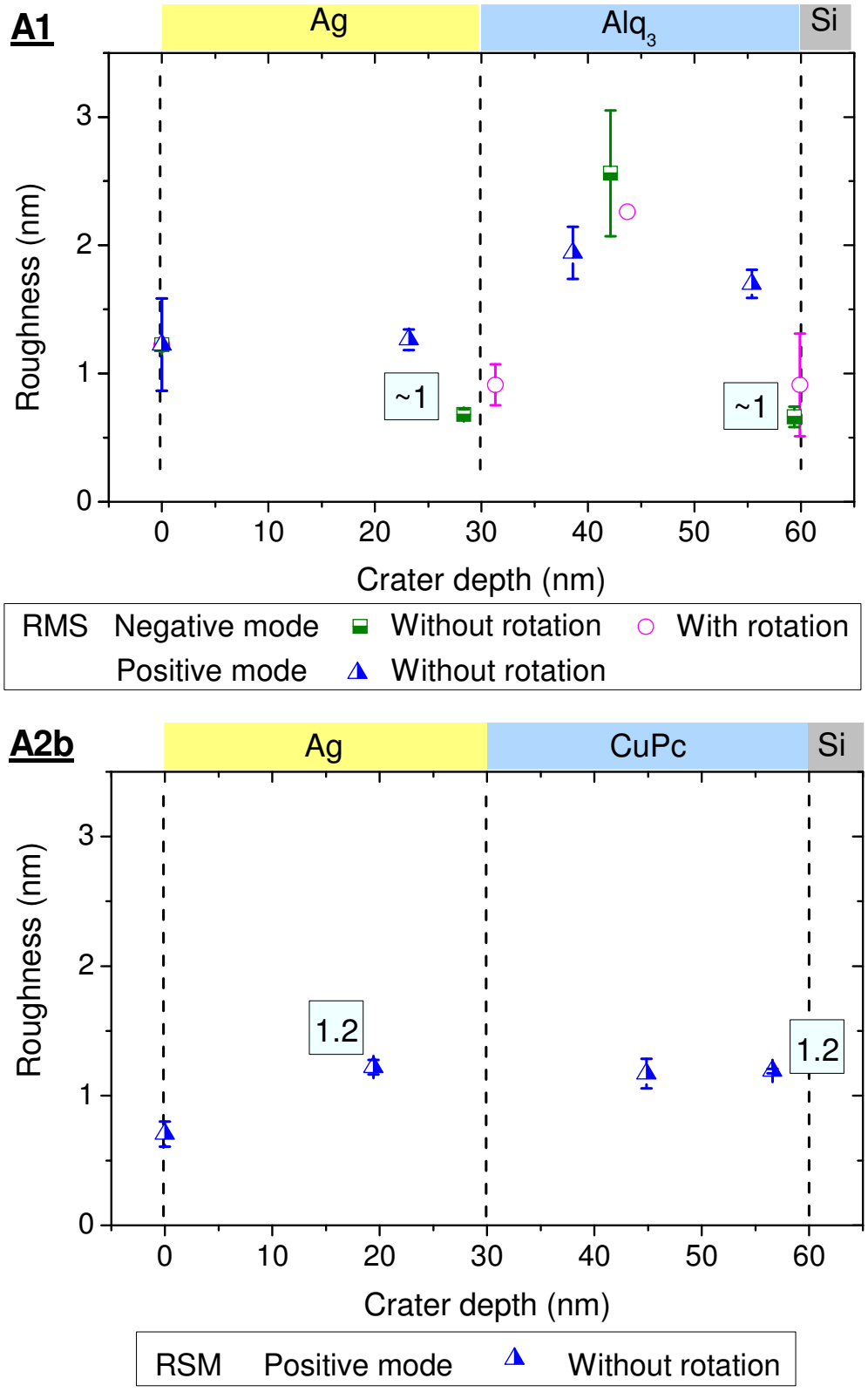

Figure V.7: *Roughness variation as a function of depth in Cs^+ 500 eV energy bombardment in positive and negative mode of samples A1 and A2b.*

Figure V.8 presents the results for roughness evolution for samples B1 and B2, which are prepared in the same conditions in the lab-built VTE instrument. The surface roughness of sample B1 with 12 nm layer thicknesses is smaller than the one of sample B2 with 48 nm layer thicknesses (0.6 nm for sample B1 and 1.5 nm for sample B2). This is evidence of the statement above about roughness development during the deposition process: thin layers have smoother surfaces than thicker ones.

For sample B1, the roughness varies from 0.6 nm at the sample surface to 0.9 nm at the Ag/CuPc interface. In the organic layer it increases up to 1.5 nm, then reduces to 1.4 nm at the CuPc/Si interface. For sample B2, roughness shows however a different behaviour. At first, it increases from 1.5 nm at the sample surface to 1.8 nm in the metal film and stays constant until the Ag/CuPc interface. Afterwards it decreases continuously in the organic layer until reaching 0.5 nm at the CuPc/Si interface. This behaviour is similar to the evolution of roughness for Si sputtered by a 1 keV Cs^+ ion beam on the same instrument[248]. However, similar to the samples A1, A2b and B1, the roughness induced by ion bombardment is always smaller than 2 nm.

The results for roughness evolution of samples C1 is presented in Figure V.9. Comparing the roughness of craters at different analysis conditions, it is obvious that roughness is reduced by using sample rotation in the negative mode (500 eV impact energy and 46° incidence angle). In 2nd and 3rd craters, the roughness in craters sputtered ain the positive mode (500 eV impact energy and 63° incidence angle) is worse by 1 nm than in the negative mode. However, the roughness of sample C1 shows a similar trend than sample B1: it is slightly higher (about 1 – 2 nm) in the middle of the CuPc layer than at the sample surface and at the Ag/CuPc and CuPc/Si interfaces. These differences in roughness variation between different samples will be discussed in more detail in the next section.

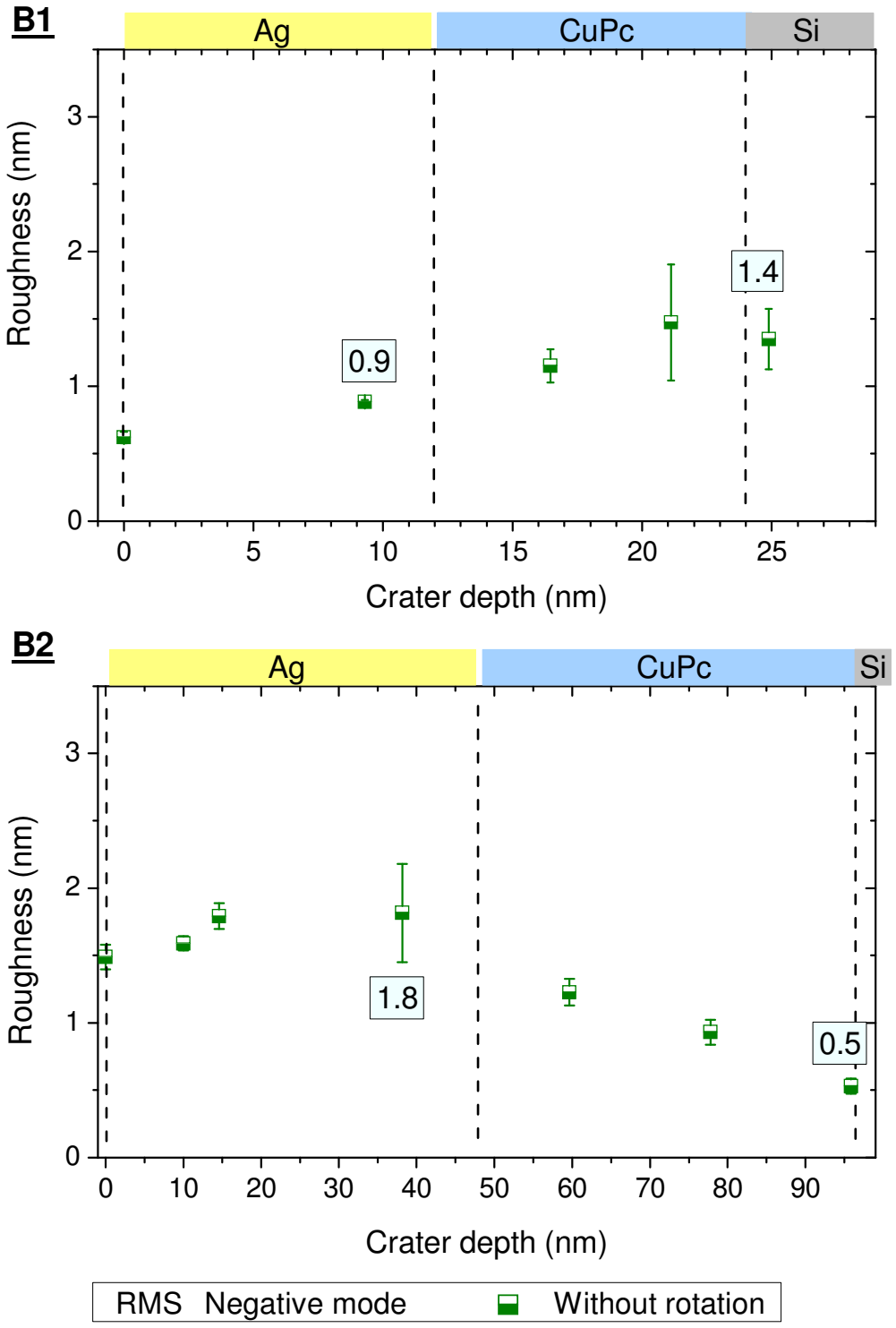

Figure V.8: *Roughness variation as a function of depth in Cs^+ low energy bombardment of samples B1 and B2.*

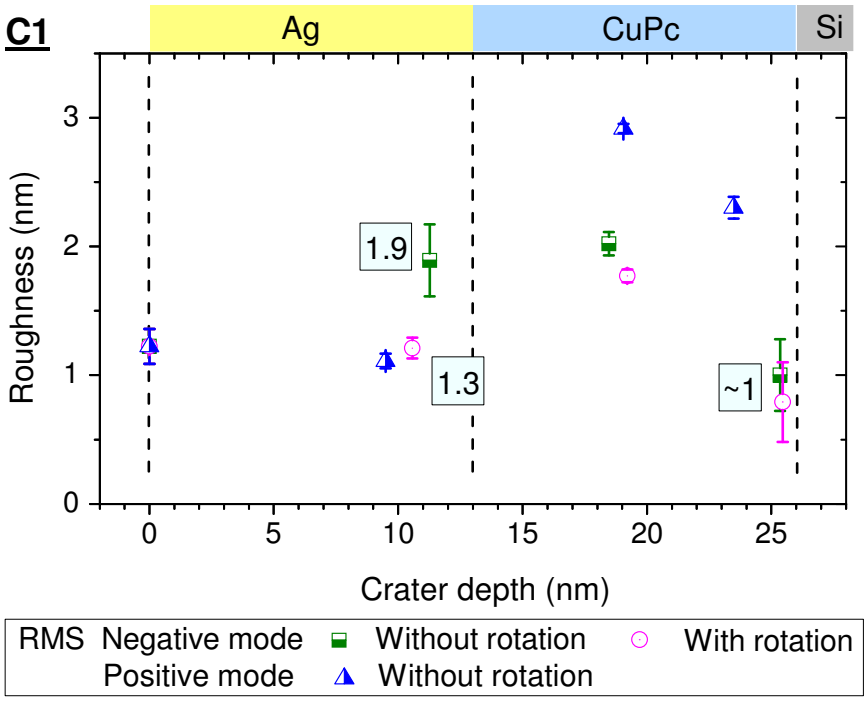

Figure V.9: *Roughness variation as a function of depth in Cs^+ 500 eV energy bombardment in positive and negative mode of sample C1.*

V.3.2. Discussion

In this study, all the craters irradiated by a 500 keV Cs^+ beam in the Cameca Sc-Ultra instrument show less than 3 nm of RMS roughness. For roughness variation in organic layers, two tendencies have been identified: roughness has a maximum value in the middle of the organic layer for sample A1 of Alq_3 and for CuPc samples with thin layer thicknesses (samples B1 and C1). Roughness remains stable or decreases during the bombardment of the CuPc sample with thicker layers (samples A2b and B2). Those differences are caused by Cs-O hillocks that develop to a different extend for the different samples. As presented in chapter IV, the craters sputtered into CuPc samples develop some Cs-O hillocks after exposure to air. The formation of those Cs-O hillocks, which are identified as Cs_2O_2 oxide, depends also on sample composition, on crater depth and whether it is located in a layer or at an interface. In craters of samples with a thick layer of CuPc, the Cs-O hillocks are large and well identified. In craters sputtered into samples with a thin layer of CuPc or with a

layer of Alq_3, the Cs-O hillocks are small and not easy to identify in the AFM images, and thus difficult to mask. Therefore, the two tendencies of roughness variation in the craters of our metal/organic samples are explained as follows: in samples A2b and B2 (thick CuPc layer), the Cs-O hillocks are easily masked and the effect of Cs-O dots can be removed from the RMS calculation. Otherwise, in samples B1 and C1 (thin CuPc layer) and in sample A1 (Alq_3), the Cs-O hillocks are small, difficult to mask in the AFM images and they contribute to the calculated RMS values. Consequently, for samples with a thin CuPc film or with Alq_3 films, the small Cs-O dots induce an increase of the RMS values, which constitutes an artefact. The Cs-O dots impede also the observation of roughness enhancement using sample rotation. In summary, in this study the surface roughness of Ag/organic samples induced by 500 eV Cs^+ bombardment at 46° or 63° incident angles is limited to less than 1.5 nm.

The sample rotation was used for the samples A1 and C1 during SIMS analysis to reduce the irradiation induced roughness[177,249], however, enhancement was seen only for sample C1. The surface roughness was also study on the samples A1 and C1 with different incidence angles: 46° in the negative mode and 63° in the positive mode. Similarly to the rotation study, no improvement is observed for sample A1 while the roughness in the craters in the CuPc layer and at the CuPc/Si interface of sample C1 is improved by 1 nm at 46° (negative mode) compared to 63° (positive mode). The increase of roughness by 1 nm at the incidence angle of 63° in the positive mode contributes surely to a more than 2 nm larger SIMS interface width in the positive mode compared to the negative mode. Other mechanisms probably contribute to the broadening. However, the reason is not fulfilled understood and would require further investigation.

Furthermore, in all situations, roughness at the different interfaces is smaller than the interface width calculated from the SIMS depth profiles. When the roughness is significantly smaller than the interface width and where the interface width at 500 eV is smaller than the one at 1 keV, the characterization of the organic multilayered samples is not limited by radiation-induced roughness. At 500 eV, the surface roughness is always limited to less than 1.5 nm. At the same impact energy in the negative mode, the interface width for A samples is in the range of 3.7-6.0 nm at the Ag/organic interface

and of 1.5-3.0 nm at the organic/Si interface. For the thin sample, the interface widths can reach to as good as 2.2 nm at Ag/organic interface and 1.4 nm at organic/Si interface. The SIMS interface width at organic/Si interface seems to be limited by atomic mixing. For CuPc, a much smaller interface width cannot be expected.

From the roughness results, the larger SIMS interface width at 63° (positive mode) compared to 46° (negative mode) incident angle is partially due to sputter-induced roughness. The difference in the SIMS interface width seen in samples with different organic molecules, different individual layer thicknesses (less than 30 nm) and prepared at different temperatures is not due to the change of sputtering-induced roughness. The contribution of sputtering-induced roughness to the SIMS interface width is about 1.5 nm for these samples.

As stated above, the roughness formation during SIMS analysis can be limited by analyzing at low incident angle. Roughness formation during SIMS analysis is not a major limitation for the characterization of interface widths in multilayered samples related to organic optoelectronic devices. As such SIMS is suited for this kind of analyses. However, a final issue is the increase of the interface widths observed for some samples when reducing the impact energy (Figure V.4). The roughness could not be characterized for all samples, and for the latter roughness formation still is the most probable reason for the increase in interface width. So, roughness formation must be closely observed when characterizing interface in this kind of samples.

V.4. Conclusions

In this study, the SIMS interface width depends not only on analysis conditions i.e. energy impact and incidence angle, but also on sample properties, i.e. interface position, layer composition, sample thickness and sample preparation.

The interface width calculated from the depth profiles in negative mode is smaller than the one in positive mode. The roughness development at too oblique incident angle in the positive mode is an explanation. Comparing different impact energies, for some samples the best conditions for depth

profiling of organic materials on the Cameca SC-Ultra instrument with Cs^+ ion beam in our study are surprisingly not at very low impact energies but at 1 keV where the incidence angle is equal to 51°. For other samples, the lowest interface width has been obtained at 500 eV, while it is in general worst at 250 eV. Roughness development is the most probable factor, and needs to be considered when characterizing interfaces. However, for some samples, the sputter-induced roughness is too small to explain the difference in interface width observed between the positive and negative modes. This could not be explained. Nevertheless when taking the necessary precautions, SIMS can be used successfully to characterize interfaces in organic optoelectronic devices. Unfortunately, characterizing roughness formation for all samples would have been too time consuming, so that a selection had to be made.

SIMS analyses are shown to be able to characterize to some extent the properties of different interfaces. For all samples and both secondary ion modes, the organic/Si interface shows a better SIMS interface width than the Ag/organic interface. Samples with Ag on MPc show a better SIMS interface width at the organic/Si interface, i.e. less atomic mixing and sputter–induced roughening than samples with Ag on Pc and Ag on Alq_3 (similar layer thicknesses and deposition conditions). Furthermore, samples with Ag on CuPc with thin layer thicknesses show a smaller SIMS interface width than samples with thicker ones. This relates to the development of surface roughness on the organic layer during deposition. For similar layer thickness, samples prepared using a cooling substrate present a SIMS interface width twice as small than when deposited at room temperature. This result agrees with results from literature where the cooled substrate produces smoother layer surfaces.

Furthermore, the optimal analysis conditions for roughness formation would require in situ characterization. The conventional AFM requires exposing a sample to air, thus the Cs-O hillocks may limit the result interpretation. At 250 eV, the high Cs surface concentration in the SIMS craters may create more Cs-O hillocks and hinder a proper characterization of the sputter-induced roughness.

Moreover, significant diffusion of Ag into the organic layer was seen in all samples. This will be the subject in the next chapter.

Chapter VI
Problem of metal diffusion in metal-organic samples

For the depth profiles presented in the previous chapter, the interface width calculated from the CN^- depth profile at the different Ag-organic interfaces varies in the range of 2.7 - 6.9 nm. This allows for the characterization of the interface widths, however the Ag depth profiles do not represent well the Ag layer. High intensities of Ag-containing secondary ion clusters are observed in the different organic layers. They cannot be lowered by using sample rotation and topography studies give a sputter–induced roughness of less than 1.5 nm (section V.3). Thus, Ag intensities are not related to irradiation-induced roughness during SIMS. Therefore, either, the presence of Ag is due to irradiation-induced diffusion during SIMS analyses or to diffusion during or after the deposition process.

This problem was already observed by other authors. Fostiropoulos et al. [250] investigate the metal diffusion into organic films by SIMS by comparing the depth profiles from a Ag/Mg/CuPc:C_{60} device with and without lifting-off the Ag/Mg cathode. The sample without cathode shows a clear Mg diffusion into organic due to deposit-induced diffusion. However, a higher Mg intensity is seen in the total device. This is attributed to sputtering-induced diffusion of the metal during analysis. Song et al. investigated the Ag/Alq_3 interface of samples using dynamic SIMS[233] and XPS[251]. The SIMS study reveals results similar to the depth profiles in chapter V. The Ag diffusion is also seen in XPS depth profiles using an Ar^+ beam for sputtering. However, in both studies the origin of the Ag diffusion is not clarified.

In this chapter, the origin of the diffusion of metal species into the organic layer as well as the influence of sample properties on these mechanisms will be investigates.

VI.1. Samples and characterization

Metal/organic layered sample		Layer thickness (nm)	Deposition temperature
A1	Ag/Alq_3	30	RT
A2a	Ag/CuPc	30	RT
A3	Ag/Pc	30	RT
A4	Ag/FePc	30	RT
A5	Ag/ZnPc	30	RT
B1	Ag/CuPc	12	RT
C1	Ag/CuPc	13	-60 °C
C2	Ag/CuPc	30	-60 °C
D	Al/CuPc	30	RT
Metal/metal/organic layered samples		**Layer thickness (nm)**	**Deposition temperature**
P	Ag/Al/CuPc	30	RT

Table VI.1: *List of samples and preparation conditions.*

In this study, we use metal/organic bi-layered samples, which are described in table VI.1. More information on preparation conditions is in I.4. To study the diffusion of metal into the organic layer during deposition, a peel-off method is used to characterize the metal/organic interface and to carry out back-side SIMS analyses. A schematic detailing the process is shown in Figure VI.1. An adhesive tape is put on the surface of the sample. After peeling off, the Ag and organic layers should stick on the tape and nothing should remain on the silicon substrate. For sample P, the method works properly and all three layers are removed with the C tape. For samples A, B, C and D, only the Ag layer is peeled off. This phenomenon can be explained through studies of other authors. Using photoemission spectroscopy and X-ray photoelectron

spectroscopy for the characterization of metal – organic interfaces, many authors demonstrated that Ag does not react with the organic layer[43,251,252], while there are a strong chemical interaction between Al and organic molecules[45,253]. Therefore, depending on the metallic layer, either the Ag/organic or the organic/Si interfaces presents the weakest bonds and either the Ag layer comes off alone or all three layers are removed by the tape. This was evidenced by Jin[39].

Afterwards, all samples are depth profiled by SIMS: the characterization of the original sample is called front-side analysis, the characterization of the Ag layer of the peeled-off samples starting from the metal-organic interface is called back-side analysis.

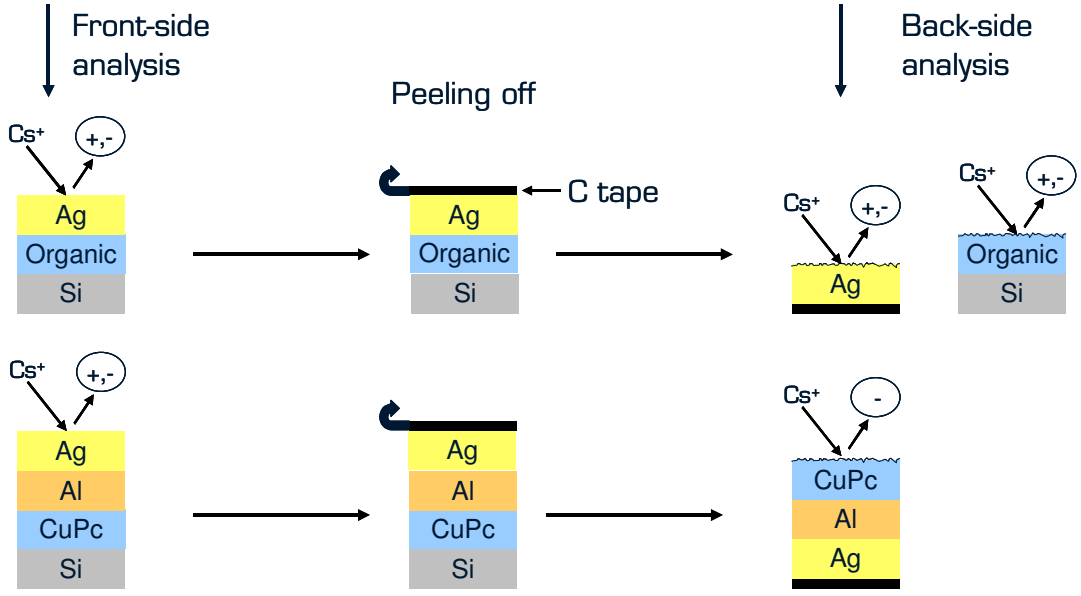

Figure VI.1: *Schematic showing front-side and back-side analysis.*

VI.2. Front-side analysis

In this section, the Ag diffusion in SIMS depth profiling of the metal – organic samples is investigated from the front-side. The depth profile of Ag is studied both in positive and negative mode for different sample compositions and preparation conditions and as a function of the primary ion impact energy.

VI.2.1. Different organic materials

The depth profiles of samples with different organic layers are compared in the negative (Figure VI.2) and the positive mode (Figure VI.3) for an impact energy of 500 eV. General comments on the depth profiles in the negative and positive modes are already presented in V.2. This chapter concentrates on the difference in depth profiles between different samples and between the different analysis conditions.

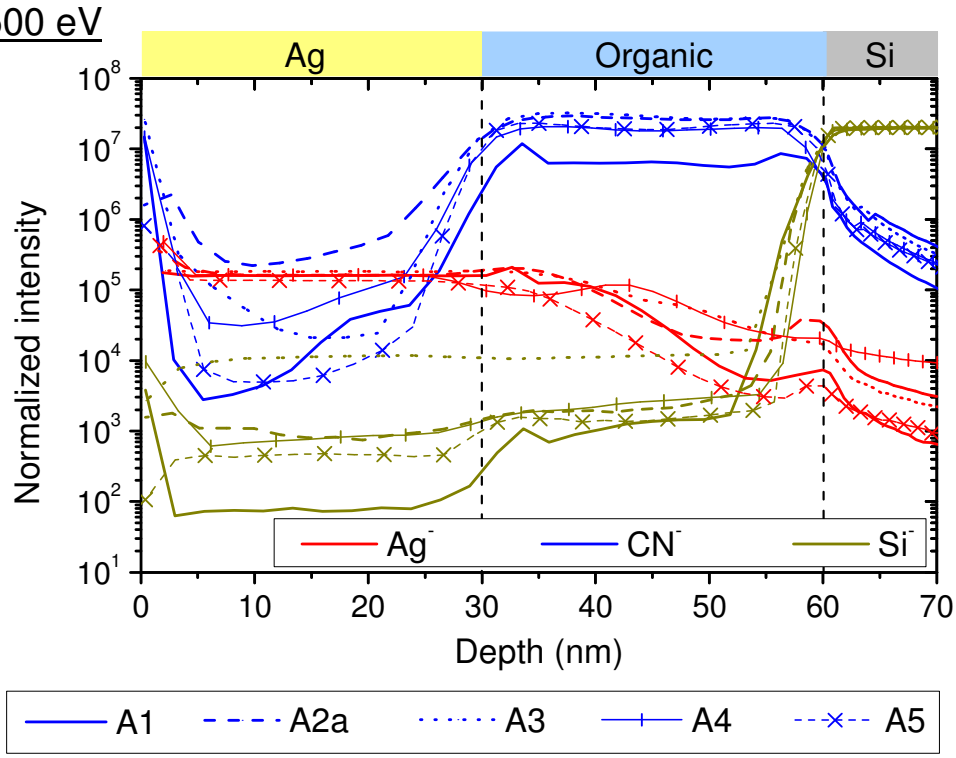

Figure VI.2: *Secondary ion intensities in negative mode as a function of depth at 500 eV Cs^+ bombardment. The depth profiles are normalized with respect to the bulk Si intensity at 2.10^7 counts/s.*

At 500 eV in the negative mode, after normalizing with the Si^- intensity in the Si substrate, the intensities of m/z=107 (Ag^-) in the Ag layers are almost identical for the different samples. The different organic layers have no influence on the properties of the thin Ag layers. The situation is changing for the organic layers. The intensity of the characteristic CN^- ions in the Alq_3 layer

of sample A1 is lower than in the phthalocyanine derivatives. This reflects the N concentration in the Alq_3 and MPc derivatives, which has been investigated in chapter III. In the organic layer, all the samples show also high intensities of m/z=107 (Ag^-) and they reduce only at the middle of the organic layer. Mass spectra recorded in the different organic layers (chapter 3), e.g. C_{60}, Alq_3 and CuPc, show the presence of negative cluster ions at the m/z =107, however their intensities are below 2.10^3 counts/s (intensity of CN^- was ~10^7 counts/s, i.e. similar to the intensity in figure VI.2) which means only about 1% of the counts is due to mass interferences.

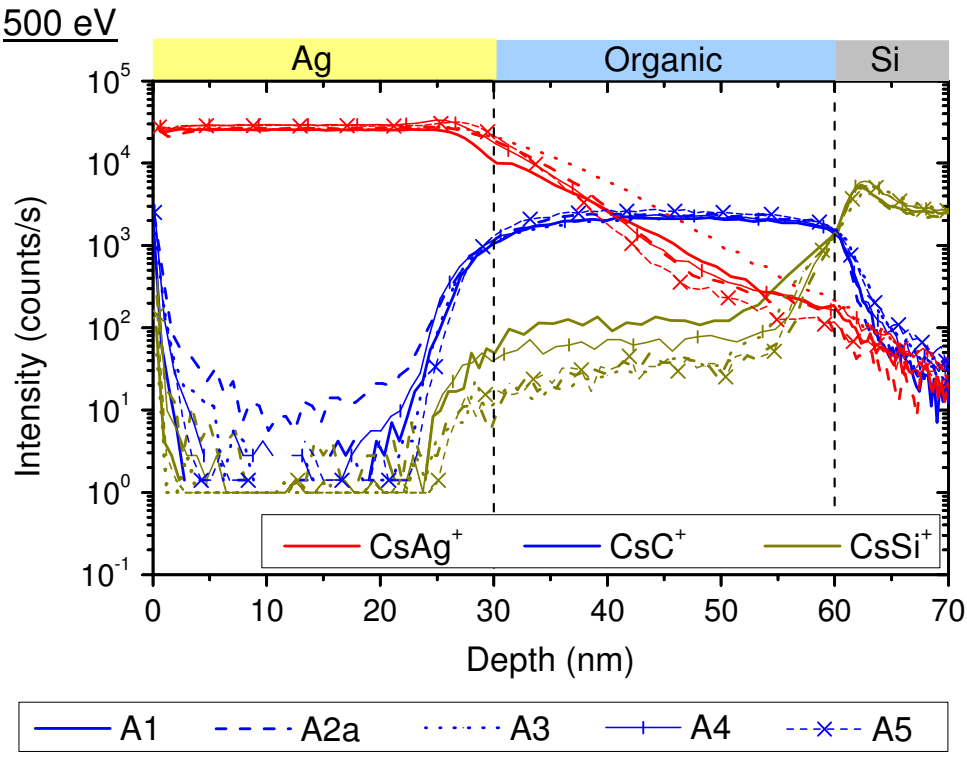

Figure VI.3: *Secondary ion intensities in positive mode as a function of depth at 500 eV Cs^+ bombardment. The depth profiles are normalized with respect to the Cs^+ intensities.*

In the positive mode, after normalizing with respect to the Cs^+ intensity, the intensity of $CsAg^+$, CsC^+ and $CsSi^+$ in the Ag layers, in the organic layers and in the Si substrate, respectively, are identical for the different organic molecules. Although the organic molecules include Alq_3 (51% atomic concentration of C)

and phthalocianine derivatives (56% atomic concentration of C), the CsC^+ intensity in organic layer stays unchanged. Moreover, similar to the negative mode, the $CsAg^+$ intensity decreases only slowly in the organic layers (Figure VI.3) which evidences that Ag enters into the organic layer by diffusion. In addition, the diffusion of Ag into the organic layers in the positive mode seems to be less than in the negative mode. Roughness formation is not at the origin of this difference. The surface roughness in craters bombarded in the two modes does not show difference for the A1_Alq_3 sample and it is a little worse in the positive mode at the middle of the organic film and the CuPc/Si interface of sample C1. Furthermore, the interface widths at the Ag/organic and organic/Si interfaces are larger in the positive mode than in the negative mode. The Ag diffusion could be partially due to sputter-induced diffusion. Differences between the negative and the positive mode could be due to the incidence angles of 47° and 64°. At the same time, different types of secondary ions are measured, where the matrix effects will be worse for the Ag^- intensities.

In addition to the results in literature, our results show that the irradiation-induced Ag diffusion is not depending a lot on the organic molecules, but more on the secondary ion type. Different formation mechanisms lead to changing matrix effects[114] and an influence of the impact angle for a given energy cannot be excluded.

VI.2.2. Variation of the impact energy between 250 eV and 1 keV

Figures VI.4 and VI.5 present the influence of impact energies on the Ag diffusion for samples A1, A2a and A4. For comparison, the depth profiles at the different impact energies are normalized with respect to the Si^- intensity in the Si substrate at 2.10^7 counts/s. For sample A1, the Ag^- intensity in the Ag layer is not changing with impact energy. However, the CN^- intensity at 1 keV is a little higher than at 500 eV and 250 eV. This is partially due to changing sputter rates, the sputter rate in the organic layer decreasing faster than the one in the inorganic layers. After normalisation, any variations due to changing

transmission of the mass spectrometer should be removed. The Ag^- depth profiles at 1 keV and 500 eV are similar. However, when the impact energy is reduced to 250 eV, the Ag^- depth profile changes. It increases when entering into the Alq_3 layer. Inside the organic layer it is at about one order of magnitude higher than at 500 eV and 1 keV. The increase is too important to be induced only by an increased ionization probability due to a higher Cs surface concentration, so that sputter-induced diffusion must be a major contribution.

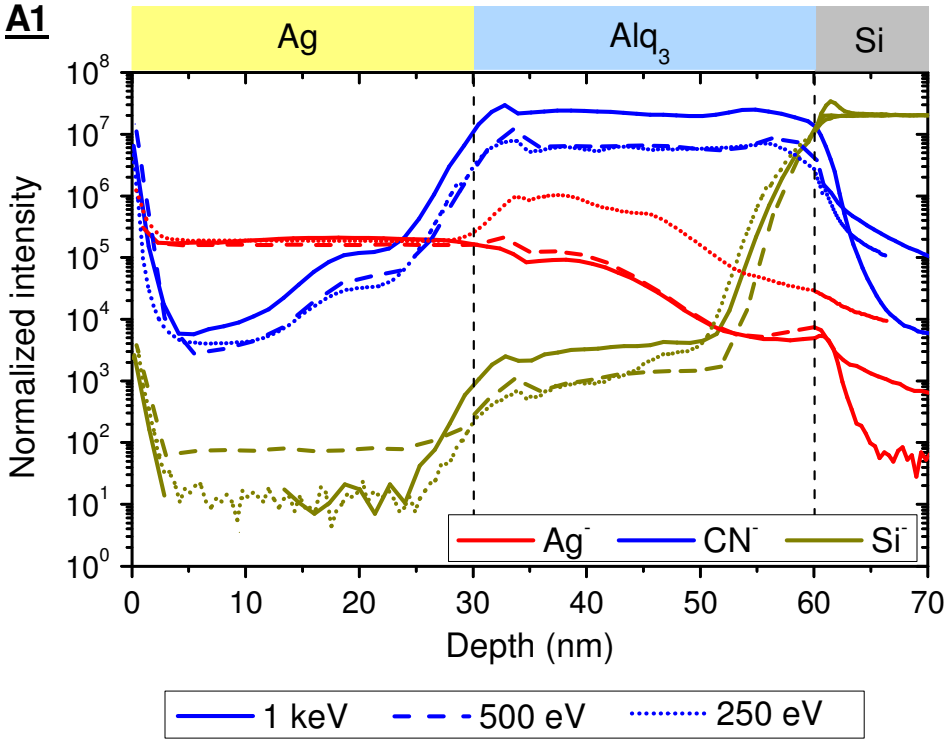

Figure VI.4: *Secondary ion intensities as a function of depth of sample A1_Alq_3 at different impact energies. The depth profiles are normalized with respect to the bulk Si intensity at 2.10⁷ counts/s.*

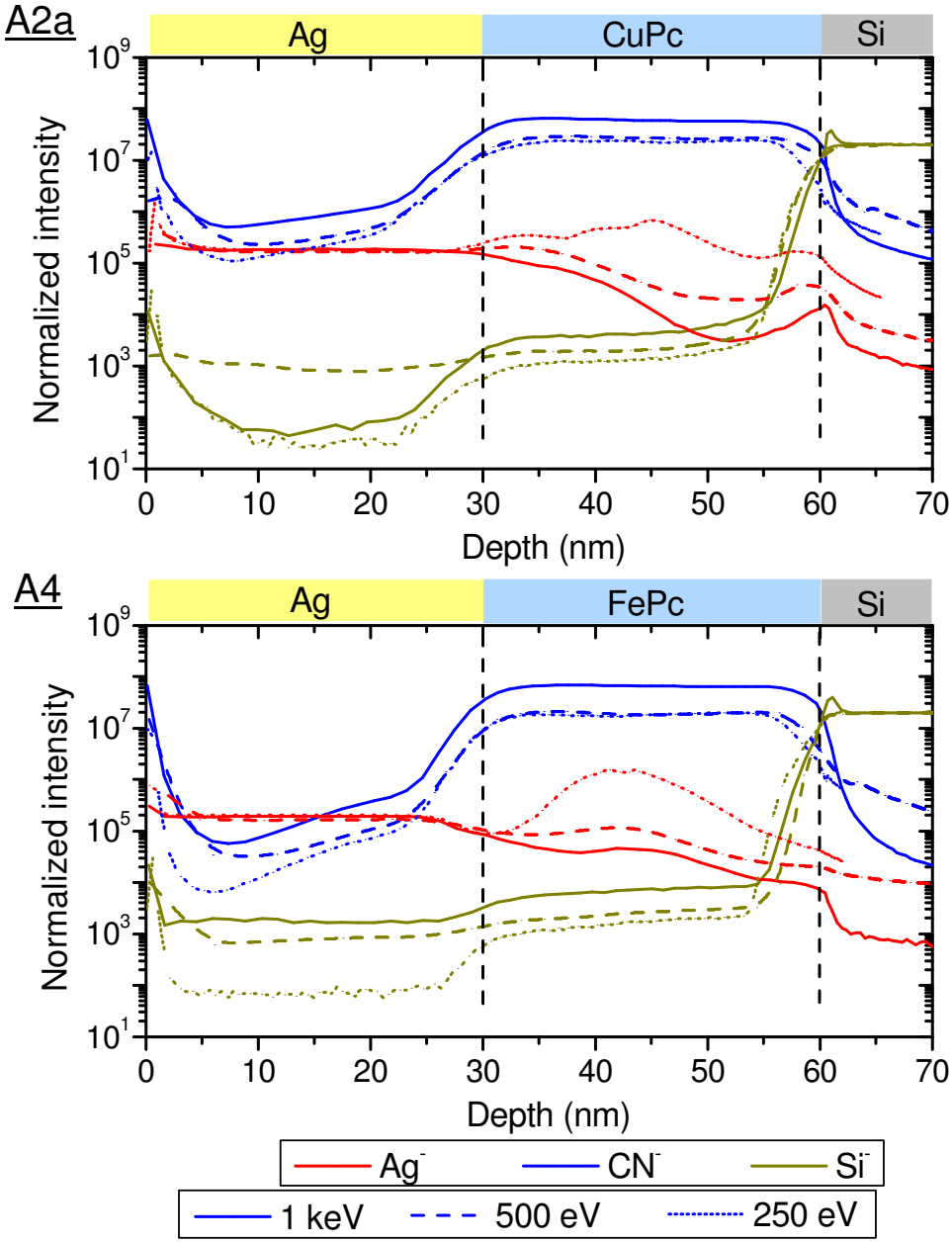

Figure VI.5: *Secondary ion intensities as a function of depth of sample A2a_CuPc and A4_FePc at different impact energies. The depth profiles are normalized with respect to the bulk Si intensity at 2.10⁷ counts/s.*

For samples A2a and A4, the depth profile tendencies are similar than for sample A1: after normalizing, the CN^- intensity is a little higher at 1 keV than at 500 eV and 250 eV and the Ag^- intensity in the Ag layers is always the same. Moreover, at 250 eV the intensity of Ag^- increases strongly in the organic layer. The Ag^- depth profile is also slightly different for the 500 eV and 1 keV

impact energies. Here, the 1 keV depth profile shows the lowest amount of Ag diffusion. As mentioned above, the intensity of mass interferences at mass m/z=107 in the organic layer is less than 2.10^3 counts/s (when Ag^- intensity is equal to 2.10^7 counts/s), so that the major contribution to m/z=107 is due to Ag diffusion. Close to the Ag/organic and organic/Si interfaces, the variation as a function of impact energy is probably caused by matrix effects. Major differences inside the layer are due to increased diffusion at lower impact energies, especially at 250 eV. The influence of the different incident angles, which are 38° at 250 eV, 47° at 500 eV and 51° at 1 keV, is not clear.

To conclude, the diffusion of Ag into the organic layer is seen at all impact energies, and it is the most pronounced at 250 eV. To limit the diffusion during sputtering, a not too low impact energy is required on the Cameca SC-Ultra instrument. Combining the diffusion results with the conditions for smallest interface width from chapter V, 1 keV impact energy (51° incidence angle) gives in general the best results for depth profiling of organic multi-layered samples for optoelectronic applications, at least at this point of the work.

VI.2.3. Influence of sample preparation at room temperature and at –60°C

Figure VI.6 presents depth profiles of sample A2a (prepared at room temperature) and sample C2 (prepared using a cooling substrate). As described in V.2.5, the samples C2 and A2a have the same layer thicknesses. At the same time, sample C2 shows a twice as good interface width at the different interfaces than sample A2a (3.2 and 1.8 nm for sample C2 and 5.9 and 2.9 nm for sample A2a at Ag/organic and organic/Si interfaces respectively). The diffusion of Ag into organic layer is seen clearly in both samples. However, the Ag^- depth profile shows also less diffusion in sample C2 than in sample A2a. Although sample C2 has higher Si^- intensity in the Si substrate and higher CN^- intensity in the organic layer, it is the Ag^- intensity in the CuPc film that is about one order of magnitude lower than in sample A2a. For our experimental deposition conditions, the CuPc layer should have the

same α-phase structure in both samples as described in reference[34]. Nevertheless, their morphologies are different. For the low temperature substrate, the CuPc layer has a fine – grain morphology. When increasing the substrate temperature, the crystals grow longer[34,36]. This change in the morphology produces films with different densities and surface roughness[39]. As a result, the sample prepared using low substrate temperature has not only sharper interface but also less Ag diffusion, which is consistent with the SIMS depth profiles. At this point, it is however not possible to clearly distinguish between diffusion during sample preparation and sputter-induced diffusion.

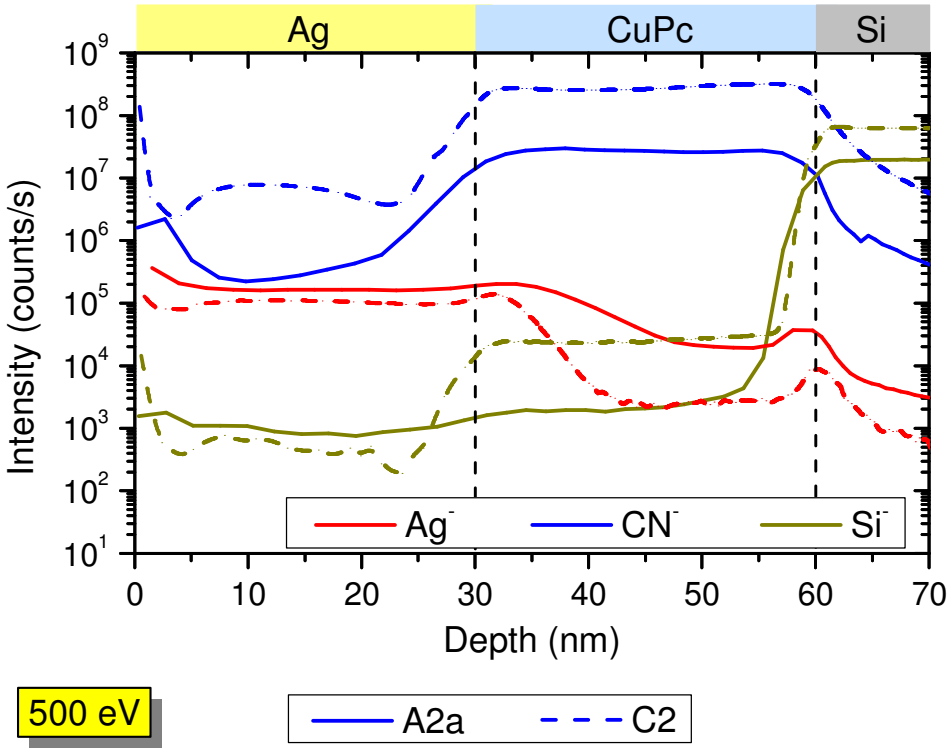

Figure VI.6: *Secondary ion intensities as a function of depth for samples A2a and C2 at 500 eV.*

For sample C2, the intensity of Ag^- decreases down to ~2.10^3 counts/s after about 13 nm from the Ag/CuPc interface. This corresponds to the intensity of mass interference at m/z=107 in the CuPc mass spectrum. Therefore, the Ag diffusion in C2 sample may stop at the depth of about 13 nm from the Ag/CuPc interface. Otherwise, the Ag diffusion of sample A2a prepared at room temperature seems to be larger than 17 nm and possibly reaches until

the CuPc/Si interface. Unfortunately the origin of the diffusion, i.e during sample preparation or sputtering-induced, cannot be clarified. The peaks in Ag^- depth profiles observed at the CuPc/Si interface in both samples are caused by a matrix effect coming from the native silicon oxide[254].

In Figure VI.7, the SIMS depth profiles of two samples prepared using similar deposition conditions than for the previous samples but with thinner layers are compared. Similar to the thick samples, the thin sample prepared using the cooled substrate has a better SIMS interface width at the interfaces than the one deposited at room temperature (cf. section V.2.5). However, the depth profiles of these two samples show that Ag diffuses largely into the organic layer. Sample C1 has the same preparation conditions than sample C2, however its Ag^- intensity decreases just a little between the Ag/CuPc and CuPc/Si interfaces. At the same time, the thickness of the CuPc film in sample C1 is 13 nm, which is equal to the diffusion depth of Ag in sample C2. The steep gradient in the Ag depth profile in sample C2 is not seen in sample C1, which is probably due to the matrix effect close to the CuPc/Si interface. Similar explanations are valid for the "deeper" Ag diffusion in sample B1 and the matrix effect, which causes a 5 nm large peak at the CuPc/Si interface.

In the Ag^- depth profile of sample B1, there are also steps at a depth of 18 nm and 25 nm depth. They are due to the change of the ion detector from the electron multiplier (EM for the range up $2x10^6$ counts/s) to the Faraday cup (FCs for the range of $1x10^6$ up to $5x10^9$ counts/s) and inverse when the secondary ion intensity is around 10^6 counts/s. The yield of the electron multiplier was adjusted to low masses (CN^- and Si^-).

In addition, in sample C1 the Ag^- depth profile has a minimum at ~1 nm before the Ag/CuPc interface. This behaviour is seen only on the thin sample prepared using a cooled substrate during the deposition process.

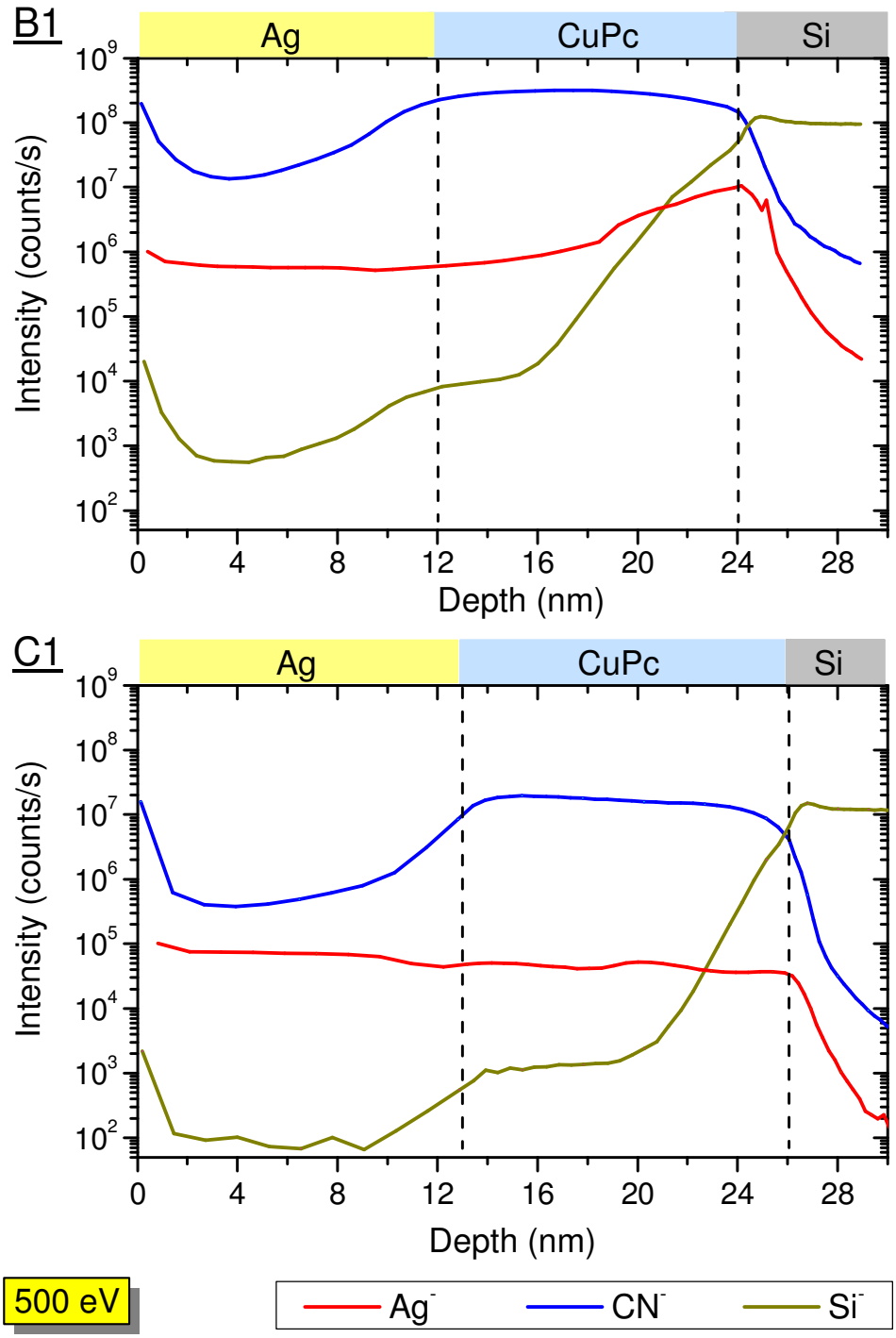

Figure VI.7: *Secondary ion intensities as a function of depth of samples B1 and C1 at 500 eV.*

VI.2.4. Sample Al on CuPc

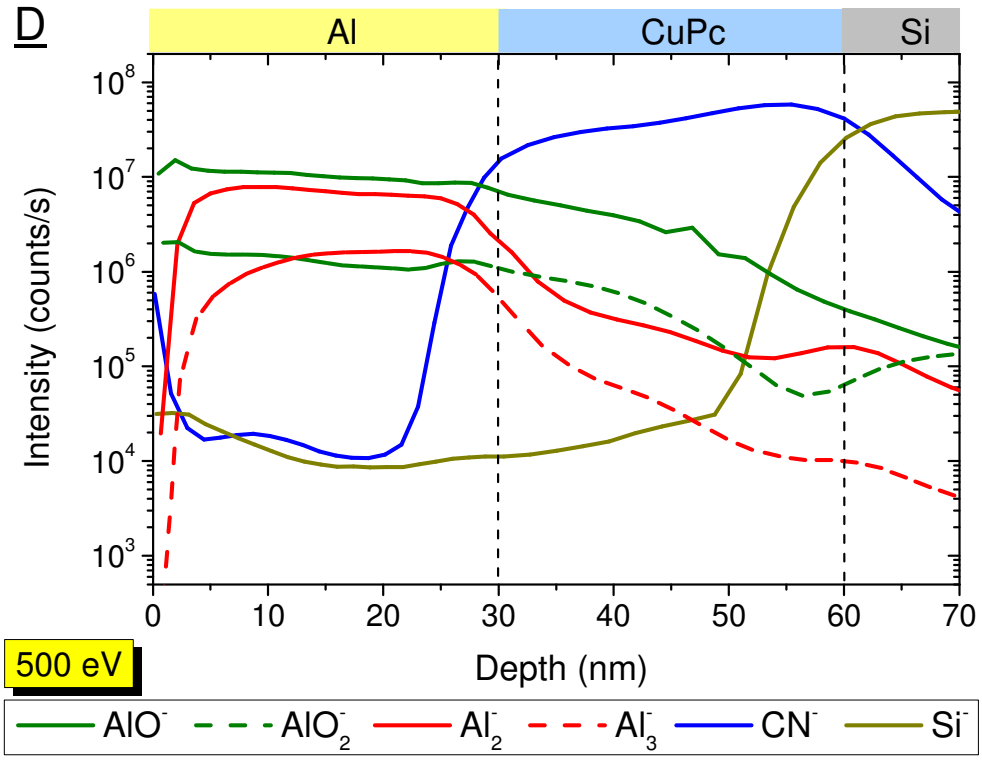

Figure VI.8: *Secondary ion intensities as a function of depth for sample D at 500 eV.*

Figure VI.8 shows the SIMS depth profiles of sample D. Similar to the calculation of the Ag/organic samples in section V.2.1, the interface widths calculated from the rising edge of CN^- and Si^- intensities show values of 6 nm and 3.1 nm at the Al/CuPc and CuPc/Si interfaces, respectively. Compared to the A samples of Ag on organic with the same layer thicknesses (cf. chapter V), the interface widths of sample D are slightly larger. In the negative mode at 500 eV, the A samples have less than 5.6 nm and 2.9 nm at the Ag/organic and organic/Si interfaces, respectively. The broadening of the metal/organic interface for Al is probably a result of the strong chemical interaction between Al and the organic layer it is deposited onto. These interactions create complex reaction/diffusion processes[44,45,253,255]. Another possible explanation of the larger interface widths is roughness formation during the SIMS analysis. This has not been verified, but there is no other

reason why the interface width at the CuPc/Si interface should increase. Si wafer and CuPc deposition conditions were the same than for other samples.

In order to understand the sputter-induced diffusion processes, the depth profiles of different Al containing cluster ions are compared in Figure VI.8. The m/z=27 (Al^-) mass is not taken into account because there is a large contribution of organic mass interferences with secondary ion intensities up to 10^6 counts/s. The mass resolution $\frac{M}{\Delta M}$ of 400 used during depth profiling is not enough to separate Al^- and the organic mass-interfering ions. The m/z of Al^- is 26.98 and with a mass resolution of 400, masses in the mass range of 26.91 amu up to 27.05 cannot be separated. Thus, it is not possible to eliminate interferences coming from organic clusters like CNH^- (m/z=27.01) or $C_2H_3^-$ (m/z=27.02). For the AlO^-, AlO_2^-, Al_2^-, Al_3^- ions, the intensity of mass interferences at m/z= 43, 54, 59, 81 is by more than 2 orders of magnitude lower than the corresponding aluminium cluster intensities. Therefore, the depth profile of these ions should show the diffusion of Al into the organic layer.

The depth profile of AlO^- and AlO_2^- ions in the Al/CuPc sample are similar to the depth profile of Ag^- in the Ag/organic samples presented previously, i.e. there are high Al intensities in almost the whole organic layer. Compared to the AlO_n^- ions, the Al_n^- cluster ions show a faster decrease of the intensity at the Al/CuPc interface. They still have high intensities until the CuPc/Si interface, even when compared to the organic mass interferences, which have intensities of about 10^3 counts/s. Yet, their depth profiles fit better to the real layer compositions and are less influenced by sputter-induced diffusion than for monoatomic secondary ions or the Al-O clusters. When SIMS crater approaches the organic layer, the metal concentration reduces and the metal atoms diffuse separately into the organic film. This decreases the formation probability of metal ion clusters both on and above the surface, thus the metal ion cluster intensity reduces faster than the monatomic ion intensity. Using metal ion clusters reduces the effect of sputter-induced diffusion on secondary ion intensities, but does not change the diffusion process itself. Moreover, the technique gets also less sensitive for deposition-induced diffusion. Similar results could be expected for Ag. However, for Ag on organic samples, the Ag_2^- and Ag_3^- depth profiles are not made due to too low secondary intensities.

VI.3. Back-side analysis

In this part, we compare the depth profiles from front-side analysis with the one from back-side analysis for the samples A1 (Ag/Alq_3), A3 (Ag/Pc) and P1 (Ag/Al/CuPc). Results are shown both for the negative (at 500 eV) and the positive mode (at 1 keV).

VI.3.1. Samples of Ag on Organic

Figure VI.9 compares the depth profiles from front-side analysis of sample A1 with the ones from back-side analysis. By combining the depth profiles from the adhesive tape and the Si substrate to the total depth profile from the front-side analysis, it is evidenced that the Ag/Alq_3/Si system separates at the Ag/Alq_3 interface. The Ag layer is sticking on the tape and the Alq_3 layer stayed on the Si substrate. The depth profiles from the peeled-off layer on the C tape show a stable intensity of Ag^- and a decrease of secondary ion intensities at m/z=26 (CN^-) and m/z=28 (Si^-) as a function of sputtering time (Figure VI.9 a). The decrease of C and N containing ion intensities show that some organic molecules or contaminations are sticking on the Ag layer after peeling off. The intensity of m/z=28 in the organic layer comes from C, N and O containing mass interferences. On the remaining substrate (Figure VI.9 b), the high intensity of Ag^- intensity at the beginning and its decrease after sputtering show the presence of Ag on or in the organic layer. Either some Ag stayed on the organic layer when peeling off or Ag diffused inside the organic layer during the deposition process. The time scales in Figure VI.9 a and b differ from the one in Figure VI.9 c which is due to a higher primary current in the front-side analysis. Moreover, the electronic gate was open in the experiment for figure VI.9 a and b and closed to 70 % in the analysis for Figure VI.9 c. Therefore, the intensities are somewhat lower in the last depth profile. Finally, peeling off the Ag layer, did not change much the depth profiles. Either the amount of Ag sticking on the organic layer is too high, or there is some Ag diffusion during sample preparation.

The depth profiles in the positive mode (Figure VI.10) show similar results as in negative mode. As for sample A1, the time scales in Figure VI.10 differ because of different primary currents. This explains also differences in secondary ion intensities for front-side and back-side analysis. However, by using the MCs^+ secondary ions, the bump in the Ag^- depth profile at the interfaces, and which is due to the matrix effect caused by air contact and native silicon oxide, is overcome[114,256,257]. This is also true for sample A3 (Figure VI.12). Furthermore, the Ag intensity in the front-side analysis in Figure VI.10 is slightly more important than in the back-side analysis, showing that some irradiation-induced diffusion exists. The MCs^+ ions are less influenced by matrix effects, so that the influence of irradiation-induced diffusion can be see more clearly in the positive mode than in the negative mode. The CsC^+ and $CsSi^+$ intensities in Figure VI.10 c are about 3 times higher than in Figure VI.10 b, while the $CsAg^+$ intensity is more than one order of magnitude higher in the front-side analysis than in the back-side.

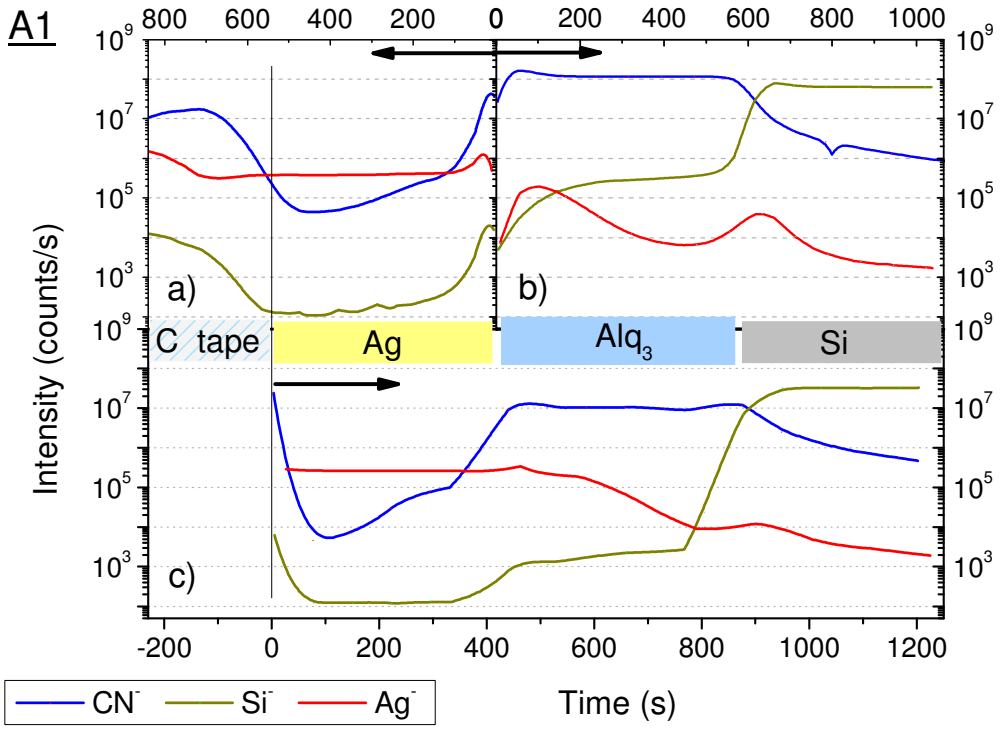

Figure VI.9: *Secondary ion intensities from the analyses a) from the back-side on the tape, b) of the peeled-off substrate and c) from the front-side of sample A1 at 500 eV.*

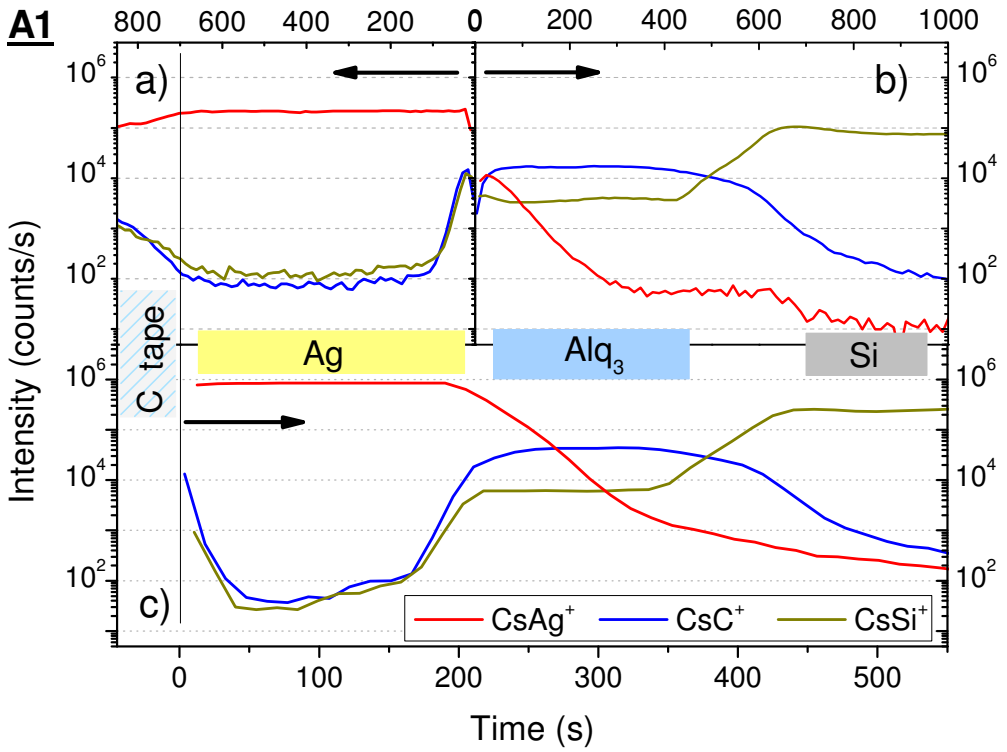

Figure VI.10: *Secondary ion intensities from the analyses a) from the back-side on the tape, b) of the peeled-off substrate and c) from the front-side of sample A1 at 1 keV.*

When peeling off sample A3, the layer separated at a similar position than for sample A1, with the Ag layer sticking on the tape and the organic layer staying on the Si substrate. However, in the negative mode the Ag^- depth profile in the substrate after peeling off in Figure VI.11 b shows almost no presence of Ag on or in the organic layer. The Ag^- intensity is about 10^4 counts/s in the organic layer after peeling off but varies in the range of 10^5 to 10^4 counts/s in the front-side analysis. 10^4 counts/s may correspond to the mass interference at m/z=107 from the organic material. Similar to sample A1, some residual Ag is seen in the positive mode on the organic layer. The $CsAg^+$ intensity is about two orders of magnitude lower in the organic layer where Ag has been peeled-off than for the front-side analysis i.e. it varies from 10^4 to 10^1 counts/s in the organic layer after peeling off and from 10^6 to 10^2 counts/s in the front-side analysis.

The CsC^+ and $CsSi^+$ intensities of sample A3 are about 2 times higher in Figure VI.12 c than in Figure VI.12 b, but the $CsAg^+$ intensity is more than two

orders of magnitude higher in Figure VI.12 c than in Figure VI.12 b. Thus the back-side depth profiling removes successfully the effect of radiation-induced diffusion. This is seen also in sample A1, but less pronounced. The variation in CsC^+ and $CsSi^+$ intensities is similar to sample A3 but is less than two orders of magnitude for the $CsAg^+$ intensity when comparing Figure VI.10 c and Figure VI.10 b. Moreover, in sample A3, the sputter-induced diffusion is identified in both negative and positive mode. Ag seems to stick less well on Pc than on Alq_3, so that it could be removed almost completely by peeling off. Intensities in the pre-equilibrium regime are increased by contaminations adsorbing on the surface after peeling off, so that final conclusions on Ag diffusion during sample preparation are difficult to draw. More conclusive results could be obtained when peeling off the metal and organic layers.

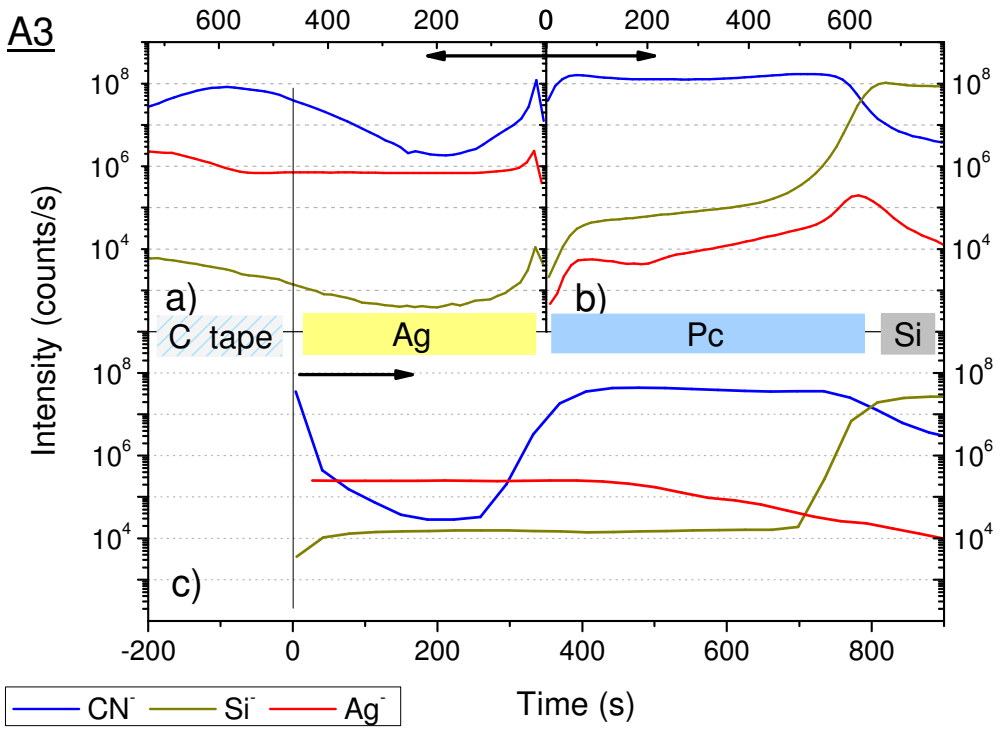

Figure VI.11: *Secondary ion intensities from the analyses a) from the back-side on the C tape, b) of the peeled-off substrate and c) from the front-side of sample A3 at 500 eV.*

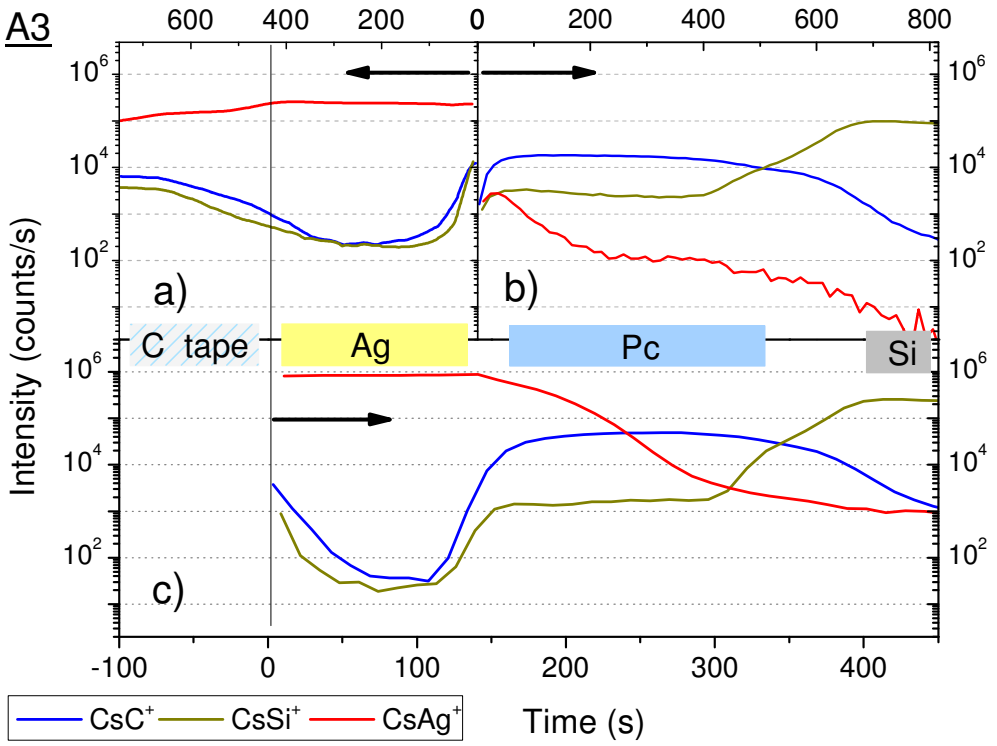

Figure VI.12: *Secondary ion intensities from the analyses a) from the back-side on the C tape, b) of the peeled-off substrate and c) of the front-side of sample A3 at 1 keV.*

VI.3.2. Sample of Ag on Al on CuPc

Figure VI.13 presents the depth profiles in the negative mode of sample P1, both for back-side and the front-side analyses. In these two graphs, the time scales are identical as the primary current is always the same. In the back-side analysis, the high intensity of CN^- secondary ions proves that the organic layer sticks on the Ag/Al layers and is also peeled off from the Si substrate.

The Ag/Al and Al/organic interfaces are badly resolved and the diffusion of organic atoms into the Al layer and of Al atoms into the Ag layer is important i.e. even the Al_3^- intensity decreases only at the Ag/adhesive tape interface. For the front-side analysis in Figure VI.13 b), a strong diffusion of Ag into the Al layer and both of Ag and Al into the organic layer is shown. High intensities of Ag^-, Al_3^- and CN^- in the organic layer in both analysis directions suggest that in addition to deposition-induced diffusion, roughness formation and sputtered-

induced diffusion during the SIMS analysis have to be taken into account. Especially the broad interface at the CuPc/Si interface demonstrates the effect of roughness formation. Although, the diffusion of the metal species is also seen for the back-side analysis (Figure VI.13 a), the metal secondary ion intensities are much lower in the organic layers in the back-side depth profile i.e. from the organic film to the Al layer, the Al_3^- intensity increases slowly from 10^2 to 10^5 counts/s in the back-side analysis while it is already above 10^5 counts/s in the organic layer in the front-side analysis. This reveals that the metal species diffuse well during or after the deposition process, but much less as indicated by the front-side analysis. Some Ag seems also to be trapped at the Al/organic interface. This information can only be obtained from the back-side depth profile.

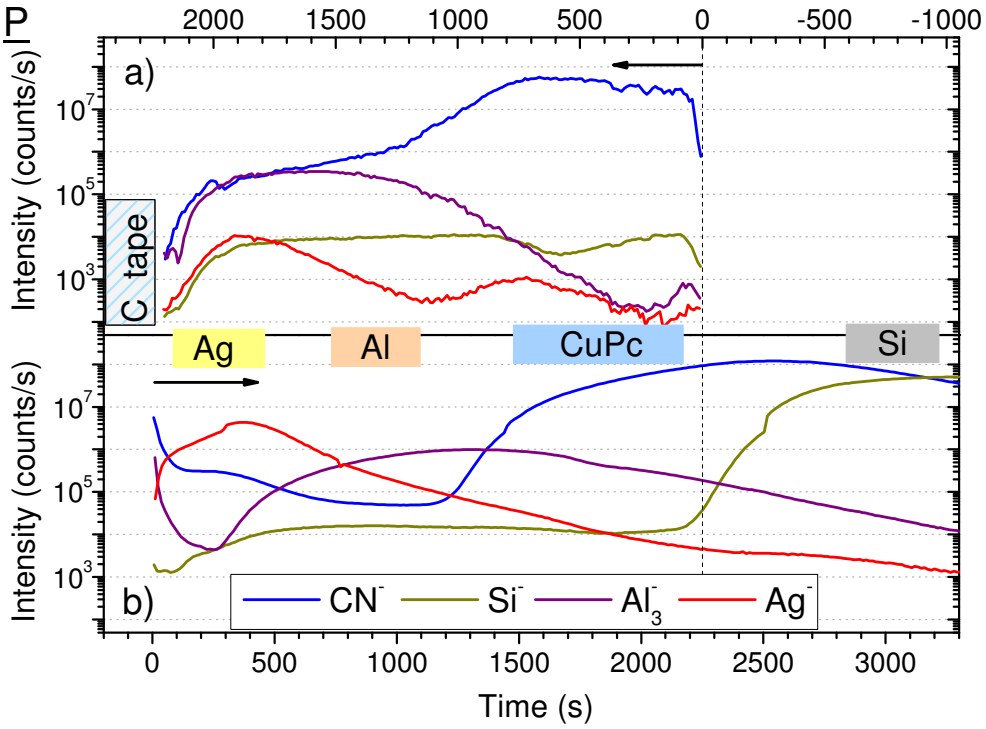

Figure VI.13: *Secondary ion intensities from the analyses a) from the back-side on the C tape and b) from the front-side of sample P1 at 500 eV.*

In summary, although the deposited layers were peeled off at organic/Si substrate, the addition of the Al layer changes the properties of the sample. Strong metal diffusion into the inner layer during and after deposition and sputter-induced diffusion during SIMS analysis in both analysis directions make

the interpretation quite complicated. The Al/organic interface is even worse than the Ag/organic interface. Nevertheless, similar to the Ag/organic samples the metal diffusion into the organic layer is proved much larger in the front-side analysis than in the back-side analysis. Furthermore, the intensity is about more than two orders of magnitude higher in the front-side analysis than in the back-side analysis. However, this Ag/Al/CuPc sample does not give any extra information on Ag diffusion during sample preparation.

VI.4. Conclusions

Metal diffusion into the organic layers is seen in SIMS depth profiles for a series of silver/organic samples. The diffusion does not depend significantly on the organic molecules tested in this study nor on the secondary ion mode. Nevertheless, the diffusion increases slightly when changing the impact energy from 1 keV to 500 eV and becomes worst at 250 eV. This metal diffusion observed in the SIMS depth profiles comes, depending on the samples, mainly from diffusion during layer deposition or mainly from sputter-induced diffusion during SIMS analysis. The diffusion reduces in the samples prepared using a cooling substrate during the deposition. However, if it is mainly due to reduced sputter-induced diffusion or due to diffusion during sample preparation could not be verified. The SIMS depth profiles show Ag diffusion depth of about 13 nm into organic film of a sample prepared at –60°C and about more than 17 nm deep into the organic film of a sample prepared at room temperature. Furthermore, the diffusion into CuPc is proven for Ag and Al. For Al/organic samples, the Al cluster ions show a better depth profile, because their formation becomes less probable in the organic layer with reduced Al concentrations. With these secondary ions, SIMS becomes less sensitive for the metal diffusion, still the origin of this diffusion cannot be clarified. Therefore, the optimal conditions for this kind of samples are 1 keV or 500 eV depending on the sample and detection of monatomic M^- or MCs^+ secondary ions.

The problem of sputter-induced diffusion can be further verified by using back-side analysis. The back-side analysis of the samples A1, A3 and P shows more

or less the presence of metal on or inside the organic layer after peeling off the Ag layer. In conclusion, the metal diffusion into the organic layers in SIMS depth profiling is due mainly to sputter-induced diffusion, however diffusion during sample preparation is also possible. The latter is difficult to study because it is not obvious to eliminate the former and it is only possible when the layers can be peeled-off properly from the substrate. When peeling off the metal layer alone, some metal atoms may remain on the organic layer as well as some organic molecules on the metal layer. This makes data interpretation complicated and SIMS-induced diffusion cannot be excluded. However, it was shown that the metal secondary ion intensities may increase by 2-3 orders of magnitude for $CsAg^+$ ions at 1 keV in positive mode and by more than 1 order of magnitude for Ag^- at 500 eV in negative mode due to sputter-induced diffusion. The sputter-induced diffusion of metal species is mainly a problem for the characterization of the metal layer and the proper identification of metal diffusion during sample preparation. However, sharp metal/organic and organic/Si interfaces of thin films can still be identified by SIMS using the rising edge of organic and Si containing cluster ions.

Conclusions and outlook

General conclusions

Recently there has been an increased interest in the development optoelectronic devices (e.g. organic light emitting diodes (OLEDs) and organic photovoltaic cells (OPV)) based on conjugated organic compounds. In these devices, the doping and the interface structure and properties influence the performance of the devices such as operational lifetime, energy conversion efficiency and charge and energy transport. In order to develop optimal deposition conditions and techniques, a characterization technique with molecular – level dimensional control for the analysis of the thin multi-layered structures is required. For this application, secondary ion mass spectrometry (SIMS) with its excellent sensitivity and its good depth resolution is a powerful technique. However, conventional dynamic SIMS with its high-energy incident ion beam fragments the organic molecules and induces important atomic mixing which harms the characterization of organic thin multi-layered samples. To overcome this problem, low-energy SIMS is introduced in this PhD thesis for the analysis of organic samples related to optoelectronic applications.

The objective of this thesis is to study the impact of low-energy ion bombardment on organic materials and the ability of SIMS to characterize organic interfaces and thin multi-layered samples. A Cs^+ primary ion beam has been chosen because of its ability to enhance the ionization probability of negative secondary ions and its potential to depth profile organic samples. To achieve these objectives, the work is organized as follows: the fragmentation of the three molecules of interest (C_{60}, CuPc and Alq_3) is studied through SIMS mass spectra, possible artefacts related to Cs-O dot formation when transferring samples between SIMS and AFM are explained and controlled, and finally typical metal/organic interfaces and structures in organic optoelectronic devices are characterized by SIMS depth profiling and AFM imaging.

At first, the mass spectra of three organic molecules (C_{60}, CuPc, Alq_3) are studied for impact energies from 5 keV down to 250 eV. They show that the molecular information is lost in steady-state conditions due to fragmentation.

However, the different molecules can be identified by different clusters, including C_n^-, C_kCs^- and C – N containing clusters. In the studied energy range, the oscillations of the C_n^- (for all three molecules used) cluster intensities do not depend on the impact energy. On the contrary, the distribution of the C_kCs^- cluster intensities varies with the impact energy. For impact energies lower than 1 keV, oscillations are observed over the whole abundance distribution, while for the other impact energies, the oscillations of the cluster intensities start only at larger cluster sizes. This is due mass interferences coming from C_nH^- clusters. Depending on the impact energy, the formation of one of the cluster types is favoured and mass inferences start at larger or smaller C_kCs^- cluster sizes. Moreover, the similarity between the distributions of the C_n^- and C_kCs^- cluster intensities and the results recorded on other C containing materials by other authors suggest that the emission and ionization mechanisms for these different kinds of materials in dynamic SIMS should be identical. From these results, clusters with high secondary ion intensities which do not depend on the impact energy are identified and selected for depth profiling in the following chapters.

Before being able to start the depth-profiling study, a work on the behaviour of implanted Cs in organic matter is presented in order to understand and avoid any artefacts in subsequent analyses combining SIMS with AFM. In the study, the SIMS imaging and AES analysis evidence the formation of Cs–O grains in SIMS craters of CuPc samples after air exposure. AFM measurements as a function of air-exposure time show the appearance, development and subsequent disappearance of Cs-O dots. A mechanism of Cs migration and oxidization was presented to explain this phenomenon. The Cs implanted diffuses to the surface, reacts with oxygen in air to form Cs_2O_2 which results in a growth of hillocks during 2 days. Later on, the diffusion stops and Cs_2O_2 transforms slowly to CsO_2 and the hillocks disappear after a few days of exposure to air. This mechanism is supported by XPS results, which compare the elemental concentrations on the craters of CuPc in vacuum, after 2 hours at air and 1 month of exposure to air. However, the Cs-O hillocks develop to a different extent for different craters. This depends on sample composition, crater depth and whether it is located in a layer or close to an interface. For example, the bi-layered sample of oxygen containing Alq_3 does not show any

well-defined Cs-O hillocks and a sample with a thin layer of CuPc shows only few Cs-O dots. The Cs-O hillocks appear only after exposure to air, and produce artefacts in analyses subsequent to SIMS depth profiling, i.e. during elemental mapping by NanoSIMS of the previously sputtered craters (local variations in secondary ion yields) and in AFM measurement (changed topography). When Cs-implanted surfaces need to be transferred to different instruments, UHV transfer is necessary in order to avoid any artefacts. For AFM, this is not possible and Cs-O dots in AFM images must be removed by a mask for the surface roughness calculation.

Next, the sputter – induced roughness in SIMS craters is calculated from AFM images. Under low-energy bombardment, the surface roughness is about 1.5 nm for different Ag/organic layers. Moreover, for all situations, at Ag/organic and organic/Si interfaces, the interface width is worse than the RMS roughness. Furthermore, the SIMS interface width depends on analysis conditions (energy impact and incident angle) as well as sample properties (interface position, layer composition, sample thickness and sample preparation). It is shown that the interface width calculated from the depth profiles in negative mode is better than the one in positive mode which is explained by the roughness development at oblique incident angles and the possible presence of mass interferences for the MCs^+ secondary ions. Among the different analysis conditions in our study, the best for depth profiling of organic materials are 500 eV or 1 keV, depending on the organic layer composition and thickness. SIMS analyses are shown to be able to characterize the properties of different interfaces when analysis conditions are chosen carefully. Samples with Ag on MPc have a better interface width at organic/Si interface than samples with Ag on Pc and Ag on Alq_3 for similar layer thicknesses and deposition conditions. The different organic structures and densities cause different sputter rates and roughness formation. Furthermore, samples with thin layer thicknesses show also a better SIMS interface width than samples with thicker ones. When comparing samples with similar layer thicknesses, samples prepared at –60°C present a better SIMS interface width than the one deposited at room temperature. These results relate to the development of organic surface roughness and mixing during

deposition. Altogether, when choosing the optimal conditions SIMS allows characterizing differences in interface width due to sample preparation.

Although the SIMS interface width at metal/organic interfaces in our study is as good as 3 nm in some cases, the metal diffusion into the organic layer can exceed more than 13 nm, and this both in the negative and the positive mode. Moreover, for a given sample the diffusion seen in SIMS depth profiles increases when changing the impact energy from 1 keV to 250 eV which is due to increased sputter-induced diffusion. This effect increases especially between 500 eV and 250 eV. Diffusion can be reduced by using a cooled substrate during the deposition process, but this could reduce diffusion during sample preparation as well as during analysis. The origin of this diffusion could however not be completely clarified in this work. Furthermore, the diffusion is observed for both Ag and Al into CuPc. The Al_n^- cluster ions are less sensitive to diffusion than the Al single containing ions. Therefore, for samples with a certain thickness i.e ~30 nm, the optimal conditions to overcome the metal diffusion in SIMS depth profiling are 500 eV or 1 keV and the detection of monatomic M^- and MCs^+ secondary ions. When combining front-side analysis with back-side analysis, the sputtering – induced diffusion during SIMS analyses becomes obvious. However, this method requires that the layers separate on the organic/Si interface, or that no metal sticks on the organic layer when they separate at the metal/organic interface. The results reveal that the sputtering – induced diffusion raises the metal-containing secondary ion intensities by 2-3 orders of magnitude at 1 keV in positive mode and by more than 1 order of magnitude at 500 eV in negative mode. To conclude, back-side depth profiling helps to characterize metal/organic interfaces and metal diffusion during the deposition process for specific samples where the peeling-off method works well.

To summarize the major findings of this PhD thesis, the mass spectra study shows a significant fragmentation of the organic matter during low-energy dynamic SIMS analyses, but characteristic secondary ions for depth profiling are found. The possibility of successful depth profiling for metal/organic layered systems is proved. When taking into account the Cs-O aggregation of the sputtered SIMS craters after exposure to air and removing any artefacts, the RMS roughness in sputtered craters is shown to be in optimal conditions

less than 1.5 nm. Under those conditions, the measured interface width and Ag diffusion are shown to become worst for the lowest impact energy. The best condition in our study for 30 nm of Ag on 30 nm of organic film is at 1 keV impact energy and 51° incident angle. However, the metal diffusion into the organic layers in SIMS depth profiles is difficult to discuss because of its two origins: the deposition-induced diffusion and the sputtering-induced diffusion. The exact contribution of each of them is difficult to determine and the latter difficult to eliminate. However, by back-side depth profiling the deposition-induced diffusion is determined to be less than 13 nm. 13 nm were found by front-side analysis, but it was not possible to convert the time scale to depth scale for the back-side analyses. Thus, low-energy SIMS is well suited to analyse organic thin layered samples and interface structures.

This work reveals the possibility to use low-energy dynamic SIMS to characterize interface roughness and metal diffusion in organic optoelectronic devices. This information is important to understand the degradation mechanisms of these devices under normal operation conditions and to contribute to the development of new devices. It was shown that interface roughness has an impact on interface heat conduction, i.e. for thin multilayers the thermal boundary resistance increases with reducing the interface mixing. In addition, a rough metal electrode scatters plasmons more effectively and enhances the emission intensity of OLEDs. These examples illustrate the importance of results obtained by SIMS.

Outlook: LE-SIMS for organic optoelectronic devices

In this work, the use of a low-energy Cs ion bombardment for the depth profiling of organic optoelectronic devices was explored. However, changing from caesium primary ions to oxygen primary ions is also of interest. Although the O_2^+ ions beam is better for the analysis of electropositive elements, its reaction with metal species or other atoms of the sample could be used to form stoichiometric (metal) oxides which minimize the roughening of the sputtered surface. this was already proven for inorganic samples[258,259], where the achievable interface resolutions could be improved.

In the Cameca Sc-Ultra instrument, the temperature of the sample holder is room temperature. Thus, the thermal diffusion of metal atoms into the organic films and the atomic mixing are not minimized. Moreover, the use of low-temperature sample holder during the depth profiling of polymers was shown by other authors to reduce the roughening and fragmentation by cluster ion bombardment[260-262]. Thus combining dynamic low-energy SIMS with a temperature-controlled sample holder during depth profiling can be a potential method to enhance the characterization of interfaces in organic multilayered samples.

Recently, the development of massive Ar_n^+ cluster ion sources shows also the ability to depth profile organic materials[263,264] with limited formation of surface roughness and no accumulation of sample damage. In future, it is important to follow and compare the improvement in depth profiling for low energy monoatomic ion beams and massive cluster ion beams organic multi-layered samples. For the moment, low-energy bombardment has the advantage of a higher depth resolution, while the molecular structure is much better conserved with massive Ar_n^+ cluster bombardment.

Appendix A
Cameca Sc-Ultra instrument and charge effect

A.1. Cs source

The schematic of the Cs source is presented in Figure A.1. The reservoir and the ionizer are heated independently by two filaments: the reservoir to 400°C and the ionizer to 1100°C. At a temperature of 400°C, the tablet of cesium chromate (Cs_2CrO_4) or cesium carbonate (Cs_2CO_3) in the reservoir generates cesium vapour. When this vapour comes in contact with the tungsten plate (ionizer) at a temperature of 1100°C, it is ionized to Cs^+. A voltage adjustable between 3 kV and 12 kV is applied to the reservoir and the ionizer while the extraction electrode in front of the ionizer is at ground voltage (0 V) for "conventional" use and at float potential when floating voltage is applied. Therefore, the Cs^+ ions are extracted from the ionizer and accelerated through the extraction electrode into the primary column[56].

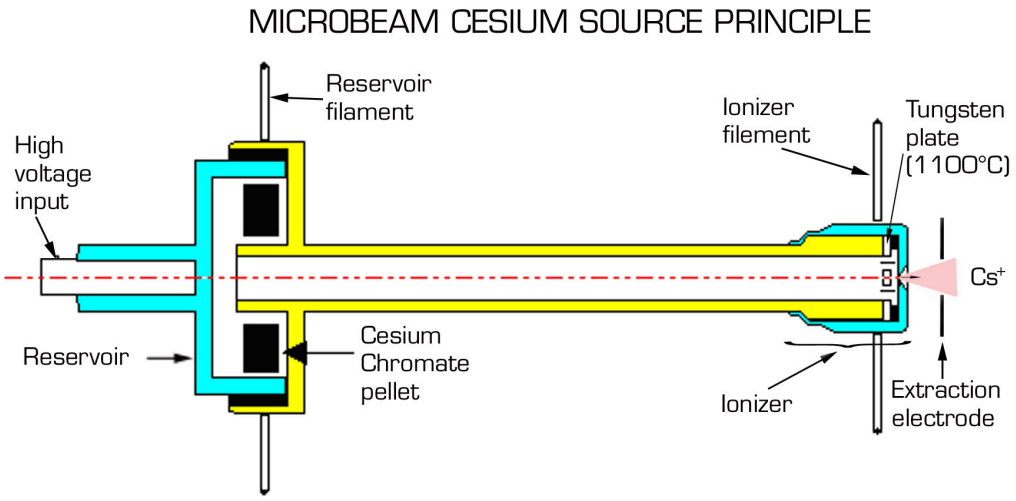

Figure A.1: *Cesium source (Cameca Sc-Ultra user manual).*

A.2. Primary column:

The primary column can be biased at any voltage (Float Volt), which allows reducing the impact energy to a few hundred eV. In a non-floating column, the impact energy is defined by the difference between the source voltage and the sample voltage. Therefore, conventional instruments do not allow working at low impact energies. Figure A.2 shows an example where the float voltage is used to obtain a low impact energy.

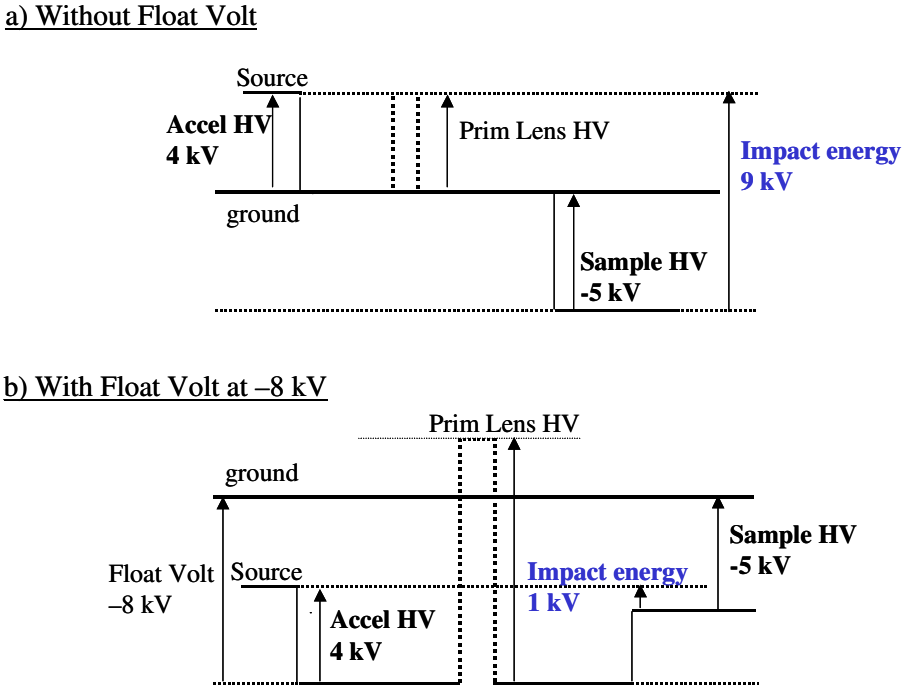

Figure A.2: *How a floating column works.*

The primary column is used to transport the ions from the source to the sample by using a system of electrostatic lenses and deflectors as well as two stencils (Figure A.3).

The perforated spherical Electrostatic Sector (switch ESA) allows either primary ions from the Cs source or primary ions from the duoplasmatron source to enter into the floating column. A pair of lenses (LPRIMO) at the two sides of the ESA is used in parallel to produce an image of the Cs source at a scale of 1:1, followed by the LPRIM1 lens. The lenses LPRIM1 and LPRIM2 project onto the first stencil a source image at a scale varying between 6:1 and 3:1.

The shaping lens LPRIM3 produces the first stencil image onto the second stencil. Thus, in combination with the two stencils, the shaping lens and the W-H deflectors allow adjusting the primary ion beam in a suitable rectangular shape. The beam blanking BBP deviates the primary ion beam into a Faraday Cup for measuring the primary current. The deflectors DPRIM5 are used to raster scan the primary ion beam over the sample. The raster size can be selected from 50x50 μm^2 to 500x500 μm^2. The last lens LPRIM5 focuses the primary ion beam on the sample surface. Its electrode closest to the source is biased to the Floating Volt while the last electrode is set to the sample voltage (from Cameca Sc-Ultra user manual).

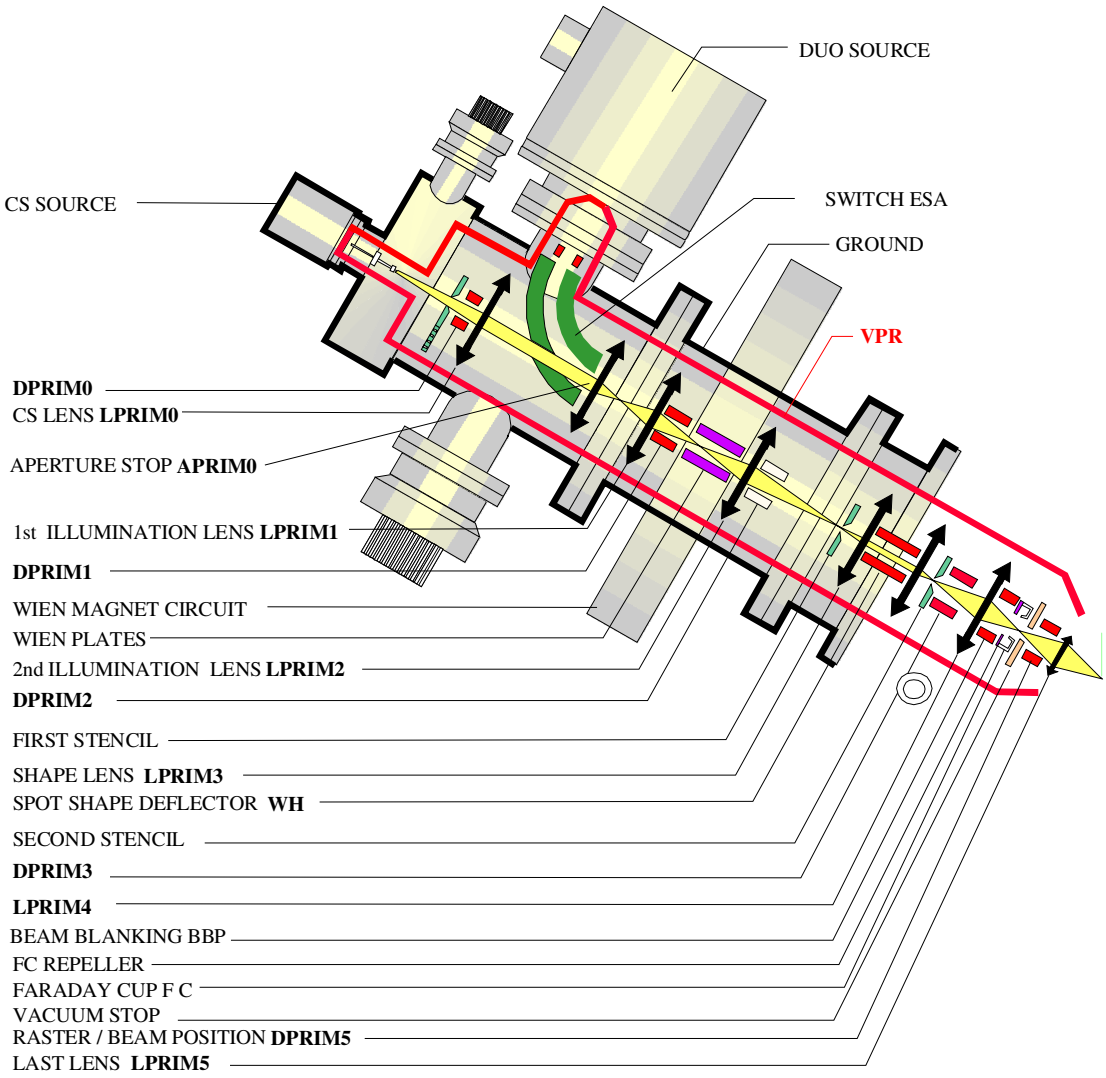

Figure A.3: *Primary column schematics (Cameca Sc-Ultra user manual).*

A.3. Mass spectrometer

Secondary ions sputtered from the sample are extracted into a double focusing magnetic sector mass spectrometer. Being filtered in energy and mass, the secondary ions are then transferred either to the Faraday cup or electron multiplier for counting or projected onto a microchannel plate for visualization.

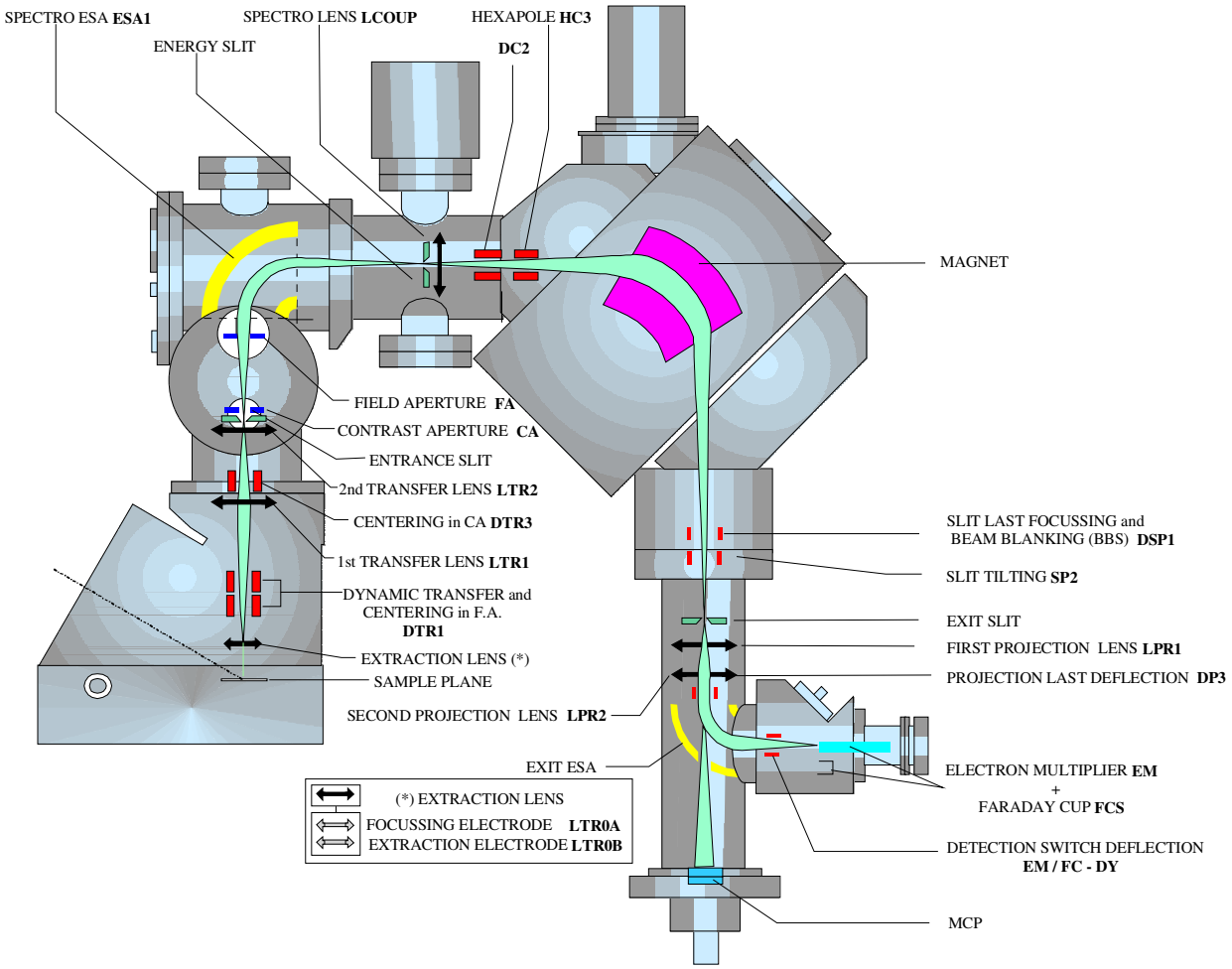

Figure A.4: *Secondary column schematics (Cameca Sc-Ultra user manual).*

The matching transfer optics system consists of an extraction lens, the two transfer lenses LTR1 and LTR2 and the deflectors DTR1 and DTR3. This system accelerates and focuses the secondary ion beam into the mass spectrometer entrance, i.e. onto the entrance slit. An optical microscope is

set behind the extraction lens, which allows observing the sample surface and helps in adjusting the surface height (Z stage) (Figure A.4).

The extraction lens (Figure A.5) is composed of 4 electrodes, among which the 1st and 4th electrodes are set at the sample HV and ground potential, respectively. Although the last electrode of the last lens in the primary column and the first electrode of the immersion lens are both biased at the sample voltage, the extraction field from the immersion lens produces a non negligible effect on the primary ion trajectory at low impact energies (variations of lateral displacement and impact angle) (from Cameca Sc-Ultra user manual). At an impact energy of 250 eV, the incident angle is 38° and 50° for an impact energy of 1 keV.

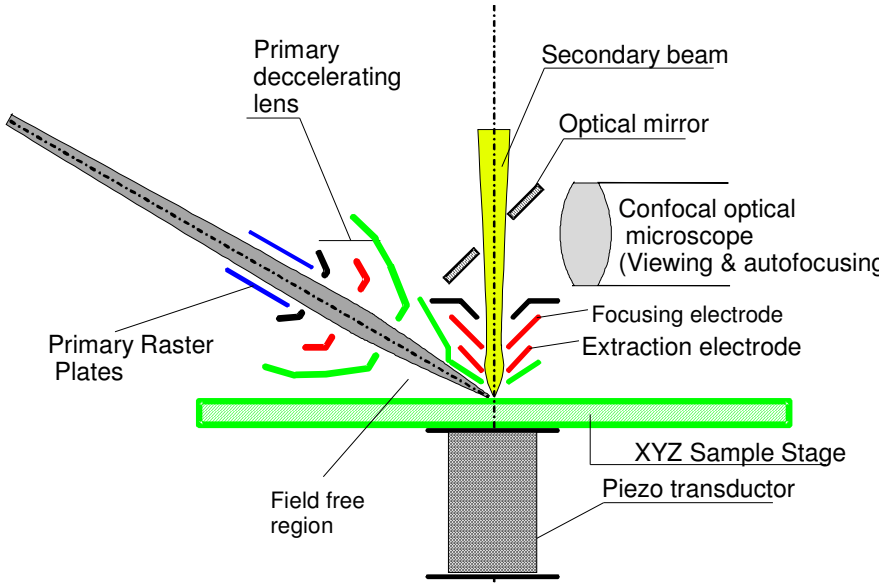

Figure A.5: *The immersion lens region. (Cameca Sc-Ultra user manual)*

The double focusing mass spectrometer consists of an electrostatic sector (ESA) for energy focusing and a magnetic sector for mass dispersion. At first, the secondary ions travel through the electrostatic sector, where they disperse in energy according to the relationship as described in [56]:

$$R = -\frac{2V}{E_0} \qquad \text{(A.1)}$$

Where R is the curvature radius of the trajectory of the particles, V is the secondary ion energy (not only acceleration voltage but whole energy $V+V_0$) and E_0 is the radial electrostatic field

An energy slit between the ESA and the magnet allows filtering the trajectories with energy in the range $V \pm \Delta V$. Moreover, the ESA forms the image of the entrance slit into the energy slit plane. An electrostatic lens (LCOUP) is placed behind the energy slit plane and projects the sample image approximately at the centre plane of the magnetic sector (Figure A.6).

Next, the primary ions that enter the magnet get dispersed in mass by the magnetic field according to the relationship:

$$R = \frac{1}{B}\sqrt{\frac{2mV}{q}} \qquad \text{(A.2)}$$

Where B is the magnetic field produced by the magnet along the ion path, m is the mass of the considered ion and q is the charge of ion.

The exit slit allows filtering only a narrow mass band. The secondary ions leaving the magnetic sector are projected through the projection optics (a pair of the lenses LPR1 and LPR2) either onto the detection systems for secondary ion counting (through a spherical ESA) or onto the microchannel plate for visualization (from Cameca Sc-Ultra user manual).

In the detection system for secondary ion counting, a deflector after the spherical ESA allows deflecting the secondary beam either to an electron multiplier (EM) or to a Faraday cup (FCs). The FCs and EM can measure count rates in the range of $5x10^5$-5.10^9 counts/s and 10^{-1} - 10^6 counts/s, respectively. Thus, this combination allows a very high dynamic range for the secondary intensities (from Cameca Sc-Ultra user manual).

On the MicroChannel Plate (MCP), either an ion sample image (image mode) or the beam cross section at the exit slit plane (slit mode) can be projected. The MPC consists of a microchannel plate, a phosphorus screen and a video camera, which allows displaying the ion images on the computer screen (from Cameca Sc-Ultra user manual).

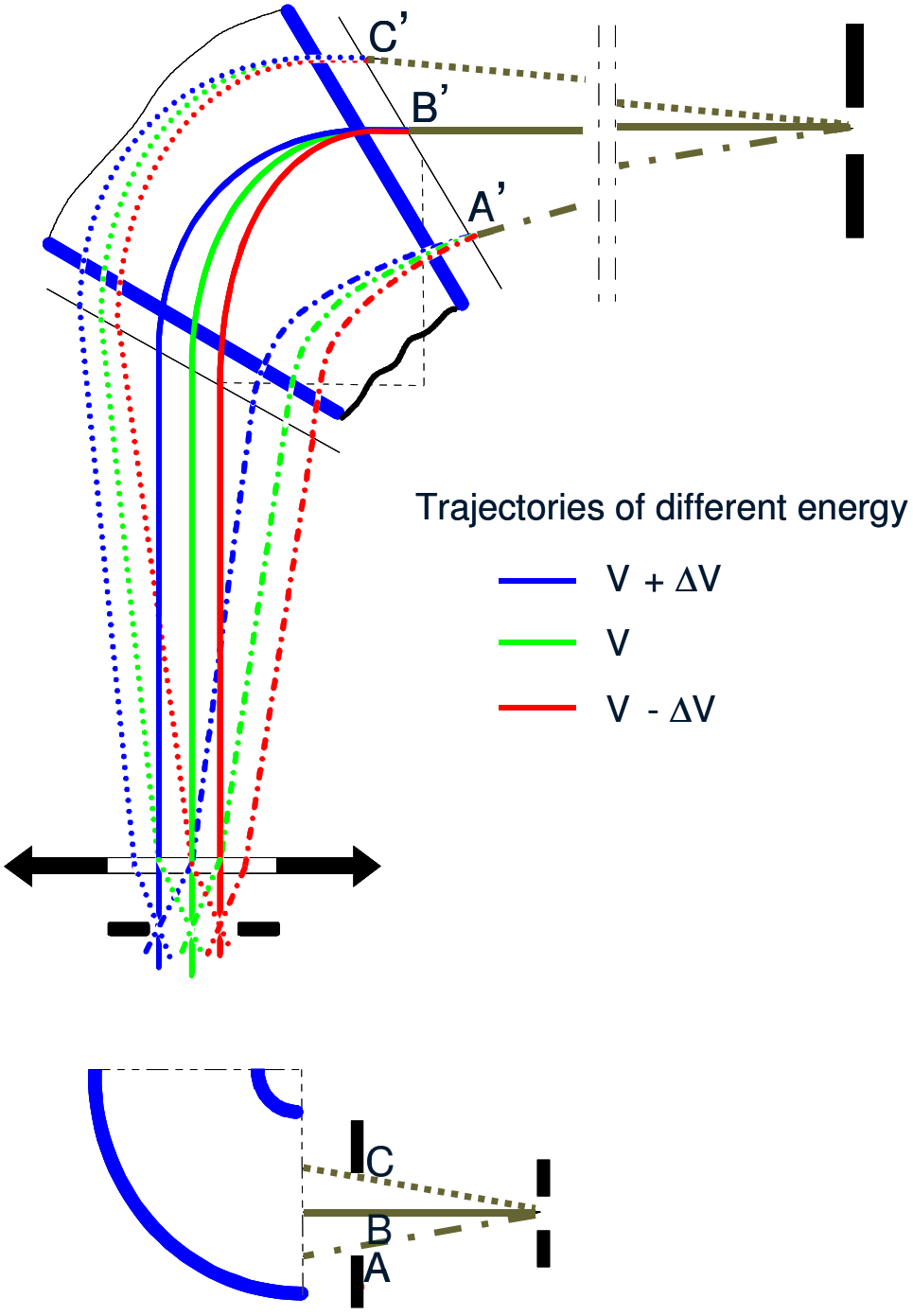

Figure A.6: *Complete schematic of the double focusing spectrometer (Cameca Sc-Ultra user manual).*

A.4. Charge effect and role of the electron gun

During SIMS analyses, an ion beam impinges the sample surface and as a result, positive and negative secondary ions as well as secondary electrons are ejected from the sample surface. As the total charge of ejected particles is not equal to the charge arriving at the surface, charge accumulation occurs over the sputtered area. For a conductive sample, the charge can transfer from / to the conductive sample holder. In this situation, the potential of the surface is kept constant. For an insulator, the electrical charge accumulates on the sputtered surface, changing the surface potential, which leads to a change of the secondary ion energy. Therefore, for important charging effects, secondary ions cannot pass the mass spectrometer and for light charging effects the secondary ion intensity becomes unstable. Most often, the sample is charging positively so that the charges can be neutralized by an electron gun.

In positive mode, the sample potential is set to a positive potential (e.g. 3 kV) Thus only positive secondary ions are extracted while negative charges including secondary electrons and negative ions are trapped on the sample surface. The amount of charges Q+ left per incoming primary ion is given by the relationship:

$$Q_+ = q_p + q_s.Y^+ \qquad (A.3)$$

q_p is the primary ion charge. When considering only singly charged primary ions, q_p is +1 and -1 for positive and negative primary ions, respectively. q_s is the sign of the charges left on surface. Y^+ is the sputter yield for positive secondary ions. This yield is always less than 1. The charging up in the positive mode for different primary ions is listed in table A.1.

Positive mode	
Primary ions	Charging up
Cs^+, O_2^+	+
O^-	-

Table A.1: *Charging up in positive mode as a function of primary ion species and charge.*

In negative mode, the sample is set to a negative potential (e.g. -3 kV). Therefore, negative secondary ions and electrons escape from the sample and leave positive charges on the sample surface. In this situation, the charge equation becomes:

$$Q_- = q_p + q_s \ (Y^- + Y^e) \qquad (A.4)$$

Y^- is the sputter yield for negative secondary ions, which is always less than 1, and Y^e is the sputter yield for secondary electrons, which is always larger than 1. From equation 4, it is deduced that for both positive and negative singly charged primary ions, a positive charge is building up over the sputtered area (Table A.2).

Negative mode	
Primary ions	Charging up
Cs^+, O_2^+	+
O^-	+

Table A.2: *Charging up in negative mode as a function of primary ion charge and species.*

In order to overcome the charge effect on insulators, a metallic coating can be used. However, this method can damage and contaminate the surface and influence the analysis. As a solution, electron flooding is used for positive charge compensation[153,265].

Reference List

1. B. Lucas, T. Trigaud, C. Videlot-Ackermann, *Polymer International* 2012; **61**: 374.

2. J. Kalinowski, V. Fattori, M. Cocchi, J. A. G. Williams, *Coordination Chemistry Reviews* 2011; **255**: 2401.

3. L. X. Xiao, Z. J. Chen, B. Qu, J. X. Luo, S. Kong, Q. H. Gong, J. J. Kido, *Adv. Mater.* 2011; **23**: 926.

4. Moliton, André, *Electronique et optoelectronique organiques,* Springer-Verlag Fance, **2011**.

5. C. Adachi, R. C. Kwong, P. Djurovich, V. Adamovich, M. A. Baldo, M. E. Thompson, S. R. Forrest, *Appl. Phys. Lett.* 2001; **79**: 2082.

6. B. W. D'Andrade, S. R. Forrest, *J. Appl. Phys.* 2003; **94**: 3101.

7. B. W. D'Andrade, S. R. Forrest, *Adv. Mater.* 2004; **16**: 1585.

8. Y. Kim, W. B. Im, *Phys. Status Solidi A* 2004; **201**: 2148.

9. M. A. Baldo, S. Lamansky, P. E. Burrows, M. E. Thompson, S. R. Forrest, *Appl. Phys. Lett.* 1999; **75**: 4.

10. R. C. Kwong, S. Sibley, T. Dubovoy, M. Baldo, S. R. Forrest, M. E. Thompson, *Chem. Mater.* 1999; **11**: 3709.

11. B. W. D'Andrade, R. J. Holmes, S. R. Forrest, *Adv. Mater.* 2004; **16**: 624.

12. M. A. Baldo, S. R. Forrest, *Phys. Rev. B: Condens. Matter* 2000; **62**: 10958.

13. C. Adachi, M. A. Baldo, M. E. Thompson, S. R. Forrest, *J. Appl. Phys.* 2001; **90**: 5048.

14. S. Nowy, B. C. Krummacher, J. Frischeisen, N. A. Reinke, W. Brutting, *J. Appl. Phys.* 2008; **104**:

15. K. Hong, J. L. Lee, *Electron. Mater. Lett.* 2011; **7**: 77.

16. L. S. Hung, C. H. Chen, *Mater. Sci. Eng. , R* 2002; **39**: 143.

17. A. McEvoy, T. Markvart, L. Castaner, *Practical hanbook of photovoltaics: Fundamentals and applications,* Elsevier, **2012**.

18. S. E. Shaheen, D. S. Ginley, G. E. Jabbour, *MRS Bull.* 2005; **30**: 10.

19. P. Peumans, A. Yakimov, S. R. Forrest, *J. Appl. Phys.* 2003; **93**: 3693.

20. N. Grossiord, J. M. Kroon, R. Andriessen, P. W. M. Blom, *Org. Electron.* 2012; **13**: 432.

21. B. P. Rand, P. Peumans, S. R. Forrest, *J. Appl. Phys.* 2004; **96**: 7519.

22. Krebs, Frederik C, *Stability and degradation of organic and polymer solar cells,* Wiley, **2-1-2012**.

23. A. M. Hassan, 2007

24. S. A. VanSlyke, C. H. Chen, C. W. Tang, *Appl. Phys. Lett.* 1996; **69**: 2160.

25. G. G. Malliaras, Y. L. Shen, D. H. Dunlap, H. Murata, Z. H. Kafafi, *Appl. Phys. Lett.* 2001; **79**: 2582.

26. H. F. Xiang, Z. X. Xu, V. Roy, C. M. Che, P. Lai, *Review of Scientific Instruments* 2007; **78**:

27. C. H. M. Maree, R. A. Weller, L. C. Feldman, K. Pakbaz, H. W. H. Lee, *J. Appl. Phys.* 1998; **84**: 4013.

28. O. Berger, W. J. Fischer, B. Adolphi, S. Tierbach, V. Melev, J. Schreiber, *Journal of Materials Science-Materials in Electronics* 2000; **11**: 331.

29. R. Prabakaran, R. Kesavamoorthy, G. L. N. Reddy, F. P. Xavier, *Physica Status Solidi B-Basic Research* 2002; **229**: 1175.

30. *WolframAlpha computational knowledge engine* 2012

31. Boyan Johnev, 2005

32. W. Y. Gao, A. Kahn, *Org. Electron.* 2002; **3**: 53.

33. D. S. Zheng, H. R. Li, Y. Y. Wang, F. J. Zhang, *Appl. Surf. Sci.* 2001; **183**: 165.

34. F. Yang, M. Shtein, S. R. Forrest, *Journal of Applied Physics* 2005; **98**:

35. M. Krzywiecki, L. Ottaviano, L. Grzadziel, P. Parisse, S. Santucci, J. Szuber, *Thin Solid Films* 2009; **517**: 1630.

36. Y. L. Lee, W. C. Tsai, J. R. Maa, *Appl. Surf. Sci.* 2001; **173**: 352.

37. I. Kroger, B. Stadtmuller, C. Stadler, J. Ziroff, M. Kochler, A. Stahl, F. Pollinger, T. L. Lee, J. Zegenhagen, F. Reinert, C. Kumpf, *New J. Phys.* 2010; **12**:

38. Z. Liu, X. Zhang, Y. Zhang, J. Jiang, *Spectrochim. Acta, Part A* 2007; **67**: 1232.

39. Y. Jin, A. Yadav, K. Sun, H. Sun, K. P. Pipe, M. Shtein, *Appl. Phys. Lett.* 2011; **98**:

40. K. Sliuziene, B. Vengalis, V. Lisauskas, R. Butkute, A. Maneikis, V. Pyragas, A. Steikuniene, M. Andrulevicius, S. Tamulevicius, *INTERNATIONAL CONFERENCE ON RADIATION INTERACTION WITH MATERIALS AND ITS USE IN TECHNOLOGIES 2008* 2008250.

41. L. He, *J. Vac. Sci. Technol. , A* 1997; **15**: 951.

42. F. Yang, M. Shtein, S. R. Forrest, *Journal of Applied Physics* 2005; **98**:

43. A. Turak, D. Grozea, X. D. Feng, Z. H. Lu, H. Aziz, A. M. Hor, *Appl. Phys. Lett.* 2002; **81**: 766.

44. S. Kwon, S. C. Kim, Y. Kim, J. G. Lee, S. Kim, K. Jeong, *Appl. Phys. Lett.* 2001; **79**: 4595.

45. T. P. Nguyen, J. Ip, P. Jolinat, P. Destruel, *Appl. Surf. Sci.* 2001; **172**: 75.

46. *Angstrom Engineering INC* 2012

47. N. Samanthule, 2010

48. J. J. Thomson, *Philosophical Magazine Series 6* 1910; **20**: 752.

49. R. F. K. Herzog, F. P. Viehböck, *Phys. Rev.* 1949; **76**: 855L.

50. R. E. Honig, *J. Appl. Phys.* 1958; **29**: 549.

51. R. C. Bradley, *J. Appl. Phys.* 1959; **30**: 1.

52. H. E. Beske, *Zeitschrift fur Angewandte Physik* 196230.

53. H. W. Werner, *Philips technical review* 1966; **27**: 344.

54. R. E. Honig, *SIMS V* 19862.

55. A. Benninghoven, *Surf. Sci.* 1975; **53**: 596.

56. A. Benninghoven, F. G. Rudenauer, H. W. Werner, *Secondary ion mass spectrometry: basic concepts, instrumental aspects, applications, and trends,* Chemical analysis, John Wiley & Sons, **1987**.

57. A. Benninghoven, *Surf. Sci.* 1994; **299-300**: 246.

58. A. Benninghoven, *Angew. Chem. Int. Ed.* 1994; **33**: 1023.

59. A. Benninghoven, W. K. Sichtermann, *Anal. Chem.* 1978; **50**: 1181.

60. J. S. Fletcher, N. P. Lockyer, J. C. Vickerman, *Mass Spectrom. Rev.* 2011; **30**: 142.

61. G. J. Leggett, M. C. Davies, D. E. Jackson, S. J. B. Tendler, *J. Phys. Chem.* 1993; **97**: 5348.

62. K. WIEN, *Nucl. Instrum. Methods Phys. Res. B* 1997; **131**: 38.

63. M. G. Dowsett, G. Rowlands, P. N. Allen, R. D. Barlow, *Surf. Interface Anal.* 1994; **21**: 310.

64. P. C. Zalm, *Mikrochim. Acta* 2000; **132**: 243.

65. A. Brown, J. C. Vickerman, *Surf. Interface Anal.* 1984; **6**: 1.

66. A. Adriaens, L. Van Vaeck, F. Adams, *Mass Spectrom. Rev.* 1999; **18**: 48.

67. A. H. M. Sondag, M. C. Raas, P. N. T. Vanvelzen, *Chem. Phys. Lett.* 1989; **155**: 503.

68. G. Stingeder, *Anal. Chem.* 1994; **297**: 231.

69. P. C. Zalm, *Rep. Prog. Phys.* 1995; **58**: 1321.

70. M. G. Dowsett, R. D. Barlow, *Anal. Chem.* 1994; **297**: 253.

71. M. G. Dowsett, R. D. Barlow, P. N. Allen, *J. Vac. Sci. Technol. , B* 1994; **12**: 186.

72. E. de Chambost, in *Advances in imaging and electron physics* (Eds: Peter W.Hawkes), Elsevier Academic Press INC, San Diego, **2011**, pp. 1-119

73. P. Fragu, J. Clerc, C. Briancon, C. Fourre, J. Jeusset, S. Halpern, *Micron* 1994; **25**: 361.

74. J. N. Audinot, S. Schneider, M. Yegles, P. Hallegot, R. Wennig, H. N. Migeon, 2003490.

75. S. Chandra, *Appl. Surf. Sci.* 2004; **231-232**: 462.

76. S. Chandra, *Appl. Surf. Sci.* 2004; **231**: 467.

77. P. Pirotte, 2007

78. M. J. Pellin, J. W. Burnett, *Pure \& Appl. Chem.* 1993; **65(11)**: 2361.

79. M. H. Shapiro, E. Trovato, T. A. Tombrello, *Nucl. Instrum. Methods Phys. Res. B* 2001; **180**: 58.

80. H. W. Werner, *Vacuum* 1974; **24**: 493.

81. Behrisch Rainer,Wittmaack Klaus, in *Sputtering by particle bombardment III* (Eds: Behrisch Rainer,Wittmaack Klaus), Springer-Verlag, **1991**, pp. 1-13

82. Behrisch Rainer,W. Eckstein, in *Sputtering by particle bombardment* (Eds: Behrisch Rainer,W. Eckstein)*,* Springer, **2007***,* pp. 1-20

83. P. C. Zalm, *Vacuum* 1996; **45(6/7)**: 753.

84. A. Delcorte, X. Vanden Eynde, P. Bertrand, D. F. Reich, *Int. J. Mass Spectrom.* 1999; **189**: 133.

85. M. Ramana, *Surf. Sci.* 2002; **500**: 523.

86. H. H. Andersen,H. L. Bay, *Sputtering by particle bombardment I,* Springer, **1981**.

87. P. Sigmund, *Sputtering by particle bombardment I,* Springer, **1981**.

88. J. Kozole, A. Wucher, N. Winograd, *Anal. Chem.* 2008; **80**: 5293.

89. L. L. Zheng, A. Wucher, N. Winograd, *Anal. Chem.* 2008; **80**: 7363.

90. A. G. Shard, F. M. Green, P. J. Brewer, M. P. Seah, I. S. Gilmore, *The Journal of Physical Chemistry B* 2008; **112**: 2596.

91. A. Wucher, *Surf. Interface Anal.* 2008; **40**: 1545.

92. Q. Wei, K.-D. Li, J. Lian, L. Wang, *J. Phys. D: Appl. Phys.* 2008; **41**: 172002.

93. W. F. van der Weg, P. K. Rol, *Nucl. Instrum. Methods* 1965; **38**: 274.

94. M. L. Yu, *Phys. Rev. B* 1984; **29(4)**: 2311.

95. G. Slodzian, *Physica Scripta* 1983; **T6**: 54.

96. P. Williams, *Applications of Surface Science* 1982; **13**: 241.

97. W. Gerhard, *Z. Phys. B: Condens. Matter* 1975; **22**: 31.

98. H. Oechsner, H. Schoof, E. Stumpe, *Surf. Sci.* 1978; **76**: 343.

99. A. Benninghoven, *Int. J. Mass Spectrom. Ion Processes* 1983; **53**: 85.

100. R. G. Cooks, K. L. Busch, *International Journal of Mass Spectrometry and Ion Physics* 1983; **53**: 111.

101. S. J. Pachuta, R. G. Cooks, *Chem. Rev.* 1987; **87**: 647.

102. A. Delcorte, B. G. Segda, P. Bertrand, *Surf. Sci.* 1997; **381**: 18.

103. H. Gnaser, *Nucl. Instrum. Methods Phys. Res. B* 1999; **149**: 38.

104. H. Gnaser, *Nucl. Instrum. Methods Phys. Res. B* 2000; **164**: 705.

105. G. Gillen, *Int. J. Mass Spectrom. Ion Processes* 1991; **105**: 215.

106. H. M. Urbassek,W. O. Hofer, *Sputtering of molecules and clusters: Basic experiments and theory,* Fundamental Processes in Sputtering of Atoms and Molecules (SPUT92)
Kongelige danske videnskabernes selskab: Matematisk-fysiske meddelelser, **1993**.

107. J. Krohn, *J. Appl. Phys.* 1962; **33**: 3523.

108. A. Mikami, T. Kazawa, Y. Kido, *Jpn. J. Appl. Phys.* 2008; **47**: 2234.

109. H. Gnaser, *Phys. Rev. B* 1996; **54(23)**: 16456.

110. P. Philipp, T. Wirtz, H. N. Migeon, H. Scherrer, *Int. J. Mass Spectrom.* 2006; **253**: 71.

111. P. Philipp, T. Wirtz, H. N. Migeon, H. Scherrer, *Int. J. Mass Spectrom.* 2007; **264**: 70.

112. P. Philipp, J. N. Audinot, T. Wirtz, H. N. Migeon, *Surf. Interface Anal.* 2010; **42**: 1499.

113. K. Wittmaack, *Nucl. Instrum. Methods Phys. Res. B* 1992; **64**: 621.

114. Y. Gao, Y. Marie, F. Saldi, H. N. Migeon, *Int. J. Mass Spectrom. Ion Processes* 1996; **144**: 11.

115. T. Wirtz, B. Duez, H. N. Migeon, H. Scherrer, *Int. J. Mass Spectrom.* 2001; **209**: 57.

116. K. Wittmaack, *Int. J. Mass Spectrom.* 2012; **313**: 68.

117. B.Berghmans and W.Vandervorst, *J. Appl. Phys.* 2009; **106**: 033509.

118. B. Berghmans, B. Van Daele, L. Geenen, T. Conard, A. Franquet, W. Vandervorst, *Appl. Surf. Sci.* 2008; **255**: 1316.

119. W. Vandervorst, T. Janssens, C. Huyghebaert, B. Berghmans, *Appl. Surf. Sci.* 2008; **255**: 1206.

120. B.Berghmans and W.Vandervorst, *J. Appl. Phys.* 2009; **106**: 033509.

121. T. Wirtz, H. N. Migeon, *Appl. Surf. Sci.* 2004; **222**: 186.

122. K. Jacobi, H. Shi, M. Gruyters, G. Ertl, *Phys. Rev. B* 1994; **49(8)**: 5733.

123. B. Woratschek, W. Sesselmann, J. Kuppers, G. Ertl, H. Haberland, *J. Chem. Phys.* 1987; **86**: 2411.

124. B. Rousseau, M. VayerBesancon, H. EstradeSzwarckopf, *Solid State Commun.* 1996; **99**: 143.

125. E. A. Podgornov, I. P. Prosvirin, V. I. Bukhtiyarov, *J. Mol. Catal. A: Chem.* 2000; **158**: 337.

126. V. I. Bukhtiyarov, I. Prosvirin, R. I. Kvon, B. S. Balzhinimaev, E. A. Podgornov, *Appl. Surf. Sci.* 1997; **115**: 135.

127. J. Hrbek, Y. W. Yang, J. A. Rodriguez, *Surf. Sci.* 1993; **296**: 164.

128. P. Dolle, S. Drissi, M. Besancon, J. Jupille, *Surf. Sci.* 1992; **269**: 687.

129. M. Besancon, H. Araghikozaz, R. Landers, J. Jupille, *Surf. Sci.* 1990; **236**: 23.

130. H. Araghikozaz, G. Brojerdi, M. Besancon, P. Dolle, J. Jupille, *Surf. Sci.* 1991; **251**: 1091.

131. D. I. Lee, Y. Sun, Z. Liu, S. Sun, S. Peterson, P. Pianetta, *J. Appl. Phys.* 2007; **102**:

132. B. Rousseau, H. EstradeSzwarckopf, *Solid State Commun.* 1993; **88**: 1.

133. W. O. Hofer, in *Sputtering by Particle Bombardment III* (Eds: R. Behrisch,K. Wittmaack)*,* Springer-Verlag, Berlin Heidelberg, **1991***,* pp. 15-90

134. H. M. Urbassek, W. O. Hofer, *Fundamental Processes in Sputtering of Atoms and Molecules (Sput92)* 199397.

135. M. L. Yu, in *Sputtering by Particle Bombardment III* (Eds: R. Behrisch,K. Wittmaack)*,* Springer-Verlag, Berlin Heidelberg, **1991***,* pp. 91-160

136. H. Gnaser, H. Oechsner, *Nucl. Instrum. Methods Phys. Res. B* 1993; **82**: 518.

137. H. Gnaser, *Phys. Rev. B* 2001; **63**: 45415.

138. A. K. Gupta, P. Ayyub, *Eur. Phys. J. D* 2001; **17**: 221.

139. M. L. Yu, in *Sputtering by particle bombardment III* (Eds: Behrisch Rainer,Wittmaack Klaus)*,* Springer-Verlag, **1991***,* pp. 91-160

140. R. Heinrich, C. Staudt, M. Wahl, A. Wucher, *SIMS XII* 1999111.

141. H. Yamamoto, F. Esaka, H. Asaoka, *SIMS XII* 1999295.

142. H. Gnaser, *Appl. Surf. Sci.* 2003; **203-204**: 78.

143. H. Gnaser, *Nucl. Instrum. Methods Phys. Res. B* 2000; **164**: 705.

144. R. Golser, H. Gnaser, W. Kutschera, A. Priller, P. Steier, C. Vockenhuber, *Nucl. Instrum. Methods Phys. Res. B* 2004; **223-224**: 221.

145. A. D. Bekkerman, N. K. Dzhemilev, S. E. Maksimov, V. V. Solomko, S. V. Verkhoturov, I. V. Veryovkin, *Vacuum* 1996; **47**: 1073.

146. R. J. Tarento, C. Dolin, P. Joyes, *Nucl. Instrum. Methods Phys. Res. B* 1993; **78**: 310.

147. S. Yang, K. J. Taylor, M. J. Craycraft, J. Conceicao, C. L. Pettiette, O. Cheshnovsky, R. E. Smalley, *Chem. Phys. Lett.* 1988; **144**: 431.

148. W. Weltner, R. J. Vanzee, *Chem. Rev.* 1989; **89**: 1713.

149. W. L. Brown, R. R. Freeman, K. Raghavachari, M. Schluter, *Science* 1987; **235**: 860.

150. J. Y. Qi, L. Dang, M. D. Chen, W. Wu, Q. E. Zhang, C. T. Au, *J. Phys. Chem. A* 2008; **112**: 12456.

151. C. G. Zhan, S. Iwata, *J. Chem. Phys.* 1996; **104**: 9058.

152. T. Ishitani, R. Shimizu, *Appl. Phys.* 1975; **6**: 241.

153. Wittmaack Klaus, in *Sputtering by particle bombardment III* (Eds: Behrisch Rainer,Wittmaack Klaus)*,* Springer-Verlag, **1991***,* pp. 161-256

154. W. Klaus, *Vacuum* 2001; **34**: 119.

155. H. H. Andersen, *Appl. Phys.* 1979; **18**: 131.

156. H. M. Urbassek, in *Sputtering by particle bombardment: Experiments and Computer Calculations from Threshold to MeV Energies* (Eds: R. Behrisch,W. Eckstein)*,* Springer, **2007***,* pp. 189-230

157. D. Evans, *Advances in Cryogenic Engineering (Materials)* 2010; **1219**: 103.

158. N. E. B. Cowern, G. F. A. Vandewalle, P. C. Zalm, D. J. Oostra, *Phys. Rev. Lett.* 1992; **69**: 116.

159. A. Charlesby, *Radiat. Phys. Chem.* 1981; **18**: 59.

160. M. Hada, S. Ibuki, Y. Hontani, Y. Yamamoto, K. Ichiki, S. Ninomiya, T. Seki, T. Aoki, J. Matsuo, *J. Appl. Phys.* 2011; **110**:

161. S. Ninomiya, K. Ichiki, H. Yamada, Y. Nakata, T. SEKI, T. Aoki, J. MATSUO, *Surf. Interface Anal.* 2011; **43**: 221.

162. A. Delcorte, B. J. Garrison, *Nucl. Instrum. Methods Phys. Res. B* 2007; **255**: 223.

163. Z. Postawa, B. Czerwinski, N. Winograd, B. J. Garrison, *J. Phys. Chem. B* 2005; **109**: 11973.

164. L. Houssiau, N. Mine, *Surf. Interface Anal.* 2010; **42**: 1402.

165. N. Wehbe, L. Houssiau, *Anal. Chem.* 2010; **82**: 10052.

166. N. Wehbe, L. Houssiau, *Surf. Interface Anal.* 2011; **43**: 190.

167. T. Aoki, S. Chiba, J. Matsuo, I. Yamada, J. P. Biersack, *Nucl. Instrum. Methods Phys. Res. B* 2001; **180**: 312.

168. W. O. Hofer, U. Littmark, *Phys. Lett. A* 1979; **71**: 457.

169. U. Littmark, W. O. Hofer, *Nuclear Instruments & Methods* 1980; **170**: 177.

170. U. Littmark, W. O. Hofer, *Nuclear Instruments & Methods* 1980; **168**: 329.

171. R. R. Hart, H. L. Dunlap, O. J. Marsh, *J. Appl. Phys.* 1975; **46**: 1947.

172. R. R. Hart, H. L. Dunlap, O. J. Marsh, *J. Appl. Phys.* 1975; **46**: 1947.

173. G. Dearnaley, *Appl. Phys. Lett.* 1976; **28**: 244.

174. A. Delcorte, X. Vanden Eynde, P. Bertrand, D. F. Reich, *Int. J. Mass Spectrom.* 1999; **189**: 133.

175. M. A. Makeev, R. Cuerno, A. L. BARABASI, *Nucl. Instrum. Methods Phys. Res. B* 2002; **197**: 185.

176. R. M. Bradley, J. M. E. Harper, *J. Vac. Sci. Technol. A* 1988; **6(4)**: 2390.

177. A. Zalar, *Thin Solid Films* 1985; **124**: 223.

178. C. W. T. Bullelieuwma, *Surf. Interface Anal.* 1986; **9**: 74.

179. M. Py, J. Barnes, M. Charbonneau, R. Tiron, J. Buckley, *Surf. Interface Anal.* 2011; **43**: 179.

180. C. M. Mahoney, A. J. Fahey, G. Gillen, *Anal. Chem.* 2007; **79**: 828.

181. C. M. Mahoney, A. J. Fahey, G. Gillen, C. Xu, J. D. Batteas, *Anal. Chem.* 2007; **79**: 837.

182. C. M. Mahoney, *Mass Spectrom. Rev.* 2010; **29**: 247.

183. K. Ichiki, S. Ninomiya, Y. Nakata, H. Yamada, T. Seki, T. Aoki, J. Matsuo, *Surf. Interface Anal.* 2011; **43**: 120.

184. N. Toyoda, I. Yamada, *Nucl. Instrum. Methods Phys. Res. B* 2012; **273**: 11.

185. A. G. Shard, F. M. Green, I. S. Gilmore, *Appl. Surf. Sci.* 2008; **255**: 962.

186. A. G. Shard, P. J. Brewer, F. M. Green, I. S. Gilmore, *Surf. Interface Anal.* 2007; **39**: 294.

187. A. Delcorte, B. Garrison, K. Hamraoui, *Anal. Chem.* 2009; **81**: 6676.

188. A. G. Sostarecz, S. Sun, C. Szakal, A. Wucher, N. Winograd, *Appl. Surf. Sci.* 2004; **231-232**:

189. C. Szakal, S. Sun, A. Wucher, N. Winograd, *Appl. Surf. Sci.* 2004; **231-232**: 183.

190. C. Guillermier, S. la Negra, R. Rickman, V. Pinnick, E. Schweikert, *Appl. Surf. Sci.* 2006; **252**: 6529.

191. S. Verkhoturov, V, R. Rickman, C. Guillemier, G. Hager, J. Locklear, E. Schweikert, *Appl. Surf. Sci.* 2006; **252**: 6490.

192. M. S. Wagner, K. Lenghaus, G. Gillen, M. J. Tarlov, *Appl. Surf. Sci.* 2006; **253**: 2603.

193. S. Ninomiya, K. Ichiki, H. Yamada, Y. Nakata, T. SEKI, T. Aoki, J. MATSUO, *Surf. Interface Anal.* 2011; **43**: 95.

194. K. Ichiki, S. Ninomiya, Y. Nakata, Y. Honda, T. Seki, T. Aoki, J. Matsuo, *Appl. Surf. Sci.* 2008; **255**: 1148.

195. J. Lee, S. Ninomiya, J. Matsuo, I. Gilmore, M. Seah, A. Shard, *Anal. Chem.* 2010; **82**: 98.

196. W. Klaus, *Vacuum* 2001; **34**: 119.

197. Y. KATAOKA, M. SHIGENO, Y. TADA, K. YAMAZAKI, M. KASE, *FUJITSU Sci. Tech. J.* 2002; **38(1)**: 69.

198. Y. Kataoka, K. Yamazaki, M. Shigeno, Y. Tada, K. Wittmaack, *Appl. Surf. Sci.* 2003; **203-204**: 43.

199. N. Fukumoto, Y. Mizukami, S. Yoshikawa, H. Morita, *Appl. Surf. Sci.* 2008; **255**: 1391.

200. R. Liu, A. T. S. Wee, D. H. Shen, H. Takenaka, *Appl. Surf. Sci.* 2004; **231-232**: 653.

201. C. M. NG, A. T. S. Wee, C. H. A. HUAN, A.SEE, *J. Vac. Sci. Technol. , B* 2001; **19(3)**: 829.

202. H. Cramer, T. Grehl, F. KOLLMER, R. Moellers, E. Niehuis, D. Rading, *Appl. Surf. Sci.* 2008; **255**: 966.

203. V. I. Shulga, *Nucl. Instrum. Methods Phys. Res. B* 2001; **179**: 485.

204. P. Sigmund, *Phys. Rev.* 1969; **184(2)**: 383.

205. Z. L. Zhang, *Nucl. Instrum. Methods Phys. Res. B* 1999; **149**: 272.

206. V. I. Shulga, *Nucl. Instrum. Methods Phys. Res. B* 2002; **187**: 178.

207. E. de Chambost, B. Boyer, B. Rasser, M. Schuhmacher, *in: A. Benninghoven, et al. (Eds.), Secondary Ion Mass Spectrometry SIMS XII, Elsevier, Amsterdam* 1999533.

208. J. L. Guerquin-Kern, T. D. Wu, C. Quintana, A. Croisy, *Biochim. Biophys. Acta* 2005; **1724**: 228.

209. J. L. Guerquin-Kern, F. Hillion, J. C. Madelmont, P. Labarre, J. Papon, A. Croisy, *Biomed. Eng. Online* 2004; **3**:

210. E. Zinner, S. Amari, R. Guinness, C. Jennings, A. F. Mertz, A. N. Nguyen, R. Gallino, P. Hoppe, M. Lugaro, L. R. Nittler, R. S. Lewis, *Geochim. Cosmochim. Acta* 2007; **71**: 4786.

211. B. Bendler, R. Barrahma, P. Philipp, T. Wirtz, *Surf. Interface Anal.* 2011; **43**: 514.

212. P. Hinterdorfer, Y. F. Dufrene, *Nat. Methods* 2006; **3**: 347.

213. A. Engel, D. J. Muller, *Nature Structural Biology* 2000; **7**: 715.

214. R. Garcia, R. Perez, *Surf. Sci. Rep.* 2002; **47**: 197.

215. *http://scientec. fr/contenu. php?cat=agilent&sub=5100* 2011

216. *http://gwyddion. net/* 2011

217. I. S. Tilinin, A. Jablonski, W. S. M. Werner, *Prog. Surf. Sci.* 1996; **52**: 193.

218. K. M. Siegbahn, 1981

219. D. Briggs,J. T. Grant, in *Surface Analysis by Auger and X-Ray Photoelectron Spectroscopy* (Eds: D. Briggs,J. T. Grant), IM Publications, Chichester, UK, **2003**, pp.

220. G. Moretti, *J. Electron. Spectrosc. Relat. Phenom.* 1998; **95**: 95.

221. J. Cazaux, 2007; **P2620**:

222. L. Houssiau, B. Douhard, N. Mine, *Appl. Surf. Sci.* 2008; **255**: 970.

223. L. Houssiau, N. Mine, *Surf. Interface Anal.* 2010; **42**: 1402.

224. K. Wittmaack, *SIMS VIII* 199291.

225. H. Gnaser, H. Oechsner, *Fresenius J. Anal. Chem.* 1991; **341**: 54.

226. Y. Gao, *J. Appl. Phys.* 1988; **64(7)**: 3760.

227. T. Wirtz, H. N. Migeon, *Surf. Sci.* 2004; **557**: 57.

228. M. Barozzi, L. Vanzetti, E. Iacob, M. Bersani, M. Anderle, G. Pucker, C. Kompocholis, M. Ghulinyan, P. Bellutti, in L. Johansson, J. Andersen, M. Gothelid, U. Helmersson, L. Montelius, M. Rubel, J. Setina, L. Wernersson), **2008**, pp.

229. *http://gwyddion. net/* 2011

230. B.Berghmans and W.Vandervorst, *J. Appl. Phys.* 2009; **106**: 033509.

231. L. S. Liao, X. H. Sun, L. F. Cheng, N. B. Wong, C. S. Lee, S. T. Lee, *Chem. Phys. Lett.* 2001; **333**: 212.

232. A. Ishitani, T. Nonaka, *Surf. Interface Anal.* 1994; **21**: 356.

233. W. J. Song, Z. P. Li, S. K. So, Y. Qiu, Y. F. Zhu, L. L. Cao, *Surf. Interface Anal.* 2001; **32**: 102.

234. W. Y. Chen, Y. C. Ling, B. J. Chen, H. H. Shih, C. H. Cheng, *Appl. Surf. Sci.* 2006; **252**: 6594.

235. K. Q. Ngo, P. Philipp, Y. Jin, S. E. Morris, M. Shtein, J. Kieffer, T. Wirtz, *Surf. Interface Anal.* 2011; **43**: 194.

236. J. P. Biersack, L. G. Haggmark, *Nucl. Instrum. Methods* 1980; **174**: 257.

237. J. P. Biersack, W. Eckstein, *Appl. Phys. A* 1984; **34**: 73.

238. W. Eckstein, W. Möller, *Nucl. Instrum. Methods Phys. Res. B* 1985; **7/8**: 727.

239. M. G. Dowsett, *SIMS X* 1995355.

240. J. B. Clegg, N. S. Smith, M. G. Dowsett, M. J. J. Theunissen, W. B. de Boer, *J. Vac. Sci. Technol. A* 1996; **14(4)**: 2645.

241. K. Wittmaack, *J. Appl. Phys.* 1982; **53(7)**: 4817.

242. J. Krohn, *J. Appl. Phys.* 1962; **33**: 3523.

243. P. A. W. van der Heide, M. S. Lim, S. S. Perry, J. Bennett, *Nucl. Instrum. Methods Phys. Res. B* 2003; **201**: II.

244. P. A. W. van der Heide, J. Bennett, *Appl. Surf. Sci.* 2003; **203**: 156.

245. W. Klaus, *Vacuum* 2001; **34**: 119.

246. P. A. W. van der Heide, M. S. Lim, S. S. Perry, J. Bennett, *Nucl. Instrum. Methods Phys. Res. B* 2003; **201**: 413.

247. *Chemicool periodic table* 2011

248. C. Mansilla, P. Philipp, T. Wirtz, *Nucl. Instrum. Methods Phys. Res. , Sect. B* 2011; **269**: 905.

249. E. H. Cirlin, J. J. Vajo, T. C. Hasenberg, R. J. Hauenstein, *J. Vac. Sci. Technol. A* 1990; **8(6)**: 4101.

250. K. Fostiropoulos, M. Rusu, *Sol. Energy Mater. Sol. Cells* 2011; **95**: 1489.

251. W. J. Song, S. K. So, J. Moulder, Y. Qiu, Y. F. Zhu, L. L. Cao, *Surf. Interface Anal.* 2001; **32**: 70.

252. O. Molodtsova, V, V. Aristov, V. Zhilin, Y. Ossipyan, D. Vyalikh, V, B. Doyle, S. Nannarone, M. Knupfer, *Appl. Surf. Sci.* 2007; **254**: 99.

253. N. Isomura, T. Mitsuoka, T. Ohwaki, Y. Taga, *Jpn. J. Appl. Phys. , Part 2* 2000; **39**: L312.

254. P. Williams, C. A. Evans, *Surface Science* 1978; **78**: 324.

255. C. Shen, A. Kahn, J. Schwartz, *J. Appl. Phys.* 2001; **89**: 449.

256. Y. Gao, *J. Appl. Phys.* 1988; **64(7)**: 3760.

257. W. Bock, H. Gnaser, H. Oechsner, *Anal. Chem.* 1994; **297**: 277.

258. K. Tsunoyama, T. Suzuki, Y. Ohashi, *Jpn. J. Appl. Phys.* 1976; **15**: 349.

259. C. M. NG, A. T. S. Wee, C. H. A. HUAN, A.SEE, *J. Vac. Sci. Technol. B* 2001; **19(3)**: 829.

260. C. M. Mahoney, A. J. Fahey, G. Gillen, *Anal. Chem.* 2007; **79**: 828.

261. C. M. Mahoney, A. J. Fahey, G. Gillen, C. Xu, J. D. Batteas, *Anal. Chem.* 2007; **79**: 837.

262. C. M. Mahoney, *Mass Spectrom. Rev.* 2010; **29**: 247.

263. J. L. S. Lee, S. Ninomiya, J. Matsuo, I. S. Gilmore, M. P. Seah, A. G. Shard, *Anal. Chem.* 2009; **82**: 98.

264. S. Ninomiya, K. Ichiki, H. Yamada, Y. Nakata, T. SEKI, T. Aoki, J. MATSUO, *Rapid Commun. Mass Spectrom.* 2009; **23**: 3264.

265. W. K., J. Maul, F. Schulz, in *Electron and Ion Beam Science and Technology* (Eds: R. Bakish), the Electrochemical Society,Inc., New York, 1974, **2011**, pp. 164-

List of Figures

List of Tables